Synthesis, Magnetism and Organisation of Molecular Coordination Compounds for Molecular Spintronics

Von der Fakultät Chemie der Universität Stuttgart
zur Erlangung der Würde eines
Doktors der Naturwissenschaften (Dr. rer. nat.)
genehmigte Abhandlung

Vorgelegt von

Junfeng Wang

aus Henan, P.R. China

Hauptberichter:	**Prof. Dr. Martin Dressel**
Mitberichter:	**Dr. Lapo Bogani**
2. Mitberichter:	**Prof. Dr. Joris van Slageren**

Tag der mündlichen Prüfung: 12. Februar 2016

1. Physikalisches Institut der Universtät Stuttgart
2016

Erklärung über die Eigenstndigkeit der Dissertation

Ich versichere, dass ich die vorliegende Arbeit mit dem Titel
Synthesis, Magnetism and Organisation of Molecular Coordination Compounds for Molecular Spintronics
selbständig verfasst und keine anderen als die angegebenen Quellen und Hilfsmittel benutzt habe; aus fremden Quellen entnommene Passagen und Gedanken sind als solche kenntlich gemacht.

Declaration of Authorship

I hereby certify that the dissertation entitled
Synthesis, Magnetism and Organisation of Molecular Coordination Compounds for Molecular Spintronics
is entirely my own work except where otherwise indicated. Passages and ideas from other sources have been clearly indicated.

Name/Name: _____

Unterschrift/Signed: _____

Datum/Date: _____

To my dear parents,

Zusammenfassung

In diesem Beitrag geht es um die rationale Synthese von Lanthanoid-basierten Einzelmolekülmagneten (Single-Molecule Magnet, SMMs) und deren Aufbringung auf unterschiedlichen Oberflächen. Die Ergebnisse der Dissertation werden in zwei Teilen dargestellt.

Im ersten Teil dieser Arbeit wird die mehrstufige Synthese von ein- und mehrkernigen Dy(III)-basierten SMMs anhand eines modularen LEGO-ähnlichen Verfahrens präsentiert. Im Weiteren wird die Auswirkung des Austauschs von Lösungsmittelmolekülen auf die dynamischen magnetischen Eigenschaften von zweikernigen Dy(III) Komplexen untersucht.

Durch modulare LEGO-ähnliche Verfahren können die grundlegenden Bausteine schrittweise zusammengebracht werden, um einen Einzelmolekülmagnet mit gewünschten magnetischen Eigenschaften zu erzeugen. Eine Reihe von mononuklearen und polynuklearen Dy(III)-basierten Einzelmolekülmagneten wurde synthetisiert, wobei wir die Dy(III) Ionen als magnetische Bausteine, Hexafluoroacetylacetone-Liganden als massige Schutzhüllen und zwei- oder dreizähnige Liganden als Linker verwendeten haben. Die erhaltenen Komplexe waren hierbei $Dy(hfac)_3bpy$ (bpy = 2,2′-bipyridine), **1**; $Dy(hfac)_3tBu\text{-}bpy$ (tBu-bpy = 4,4′-di-tert-butyl-2,2′-bipyridine), **2**; $[Dy(hfac)_3(EtOAc)]_2bpm$ (EtOAc = ethyl acetate, bpm = 2,2′-bipyrimidine), **3** and $[Dy(hfac)_3]_3HAT$ (HAT = 1,4,5,8,9,12-hexaazatriphenylene), **4**. Von diesen zeigte nur Komplex **3** eindeutiges SMM Verhalten, welches durch frequenzabhängige AC Suszeptibilitätsmessungen im Nullfeld nachgewiesen werden konnte. Quantentunneln der Magnetisierung wurde für alle Komplexe durch ein optimiertes externes Magnetfeld von 4 kOe unterdrückt, wodurch Frequenzabhängißgkeiten der AC Suszeptibilitätsmessungen in allen Fällen beobachtet werden konnten, was das SMM Verhalten bestätigte. Die größte effektive Energiebarriere, zur Spinumkehr wurde für **4** mit dem Wert von 84 K beobachtet. Die statischen magnetischen Eigenschaften zeigen die Rolle der Verbindungsgruppen für das Einführen intramolekularer Wechselwirkungen, die abgestimmt werden können. Dynamische Suszeptibilitätsmessungen an den Komplexen **1** bis **4** zeigten außergewöhnliche Unterschiede der dynamischen Eigenschaften, was deren gezielte Manipulation durch einen rationalen Syntheseansatz ermöglicht, wie z.B. die Unterdrückung von Tunnelprozessen oder das Erhalten großer Werte für die Barriere.

Die Flexibilität der supramolekularen Chemie und des magnetischen LEGO-Systems erlaubt die Bereitstellung einer zusätzlichen Koordinationsstelle am Dy(III)-Ion, welche durch Lösungsmittelmoleküle besetzt werden kann. Dies erlaubt eine gezielte Manipulation der Eigenschaften. Eine Reihe von neutralen zweikernigen Komplexen (Dy(III)-Ionen enthaltend) mit der allgemeinen Formel $[Dy(hfac)_3R]_2bpm$ (R = Null (**5**), Wasser

(H_2O, **6**), Ethylacetate (EtOAc, **3**) und Propionsäuremethylester (MP, **7**)), wurde synthetisiert. Mydosh′s Gesetz und die frequenzabhängige imaginäre χ'' Komponente der AC-Suszeptibilität beweisen, dass alle Komplexe Einzelmolekülverhalten zeigen. Eine effektive elektrostatische Modellanalyse zeigte, dass die leichte Magnetisierungsachse in der Fläche liegt, welche von gegenüberliegenden $hfac^-$-Liganden gebildet wird. Dies liegt daran dass die potentielle Energie in der Ebene geringer ist als im bpm-Liganden, im Lösungsmittelmolekl und dem letzten $hfac^-$-Liganden aufgrund der beiden β-Diketonat-Liganden mit vier großen negativ geladenen Sauerstoffatomen. Darüber hinaus ist die Richtung der magnetischen Momente annähernd senkrecht zu dem Vektor, der die beiden Dysprosium(III)-Ionen verbindet, welches die antiferromagnetische Kopplung erklärt.

Im zweiten Teil wurden die Dy(III)-basierten Einzelmolekülmagnete mittels SQUID Magnetometrie untersucht, um zu identifizieren ob sie ihre molekularen magnetischen Eigenschaften auch nach Aufbringung auf unterschiedlichen Oberflächen beibehalten. Die Dysprosium(III) Dimer (**3**) wurde auf SiO_2- und auf Graphen-Oberflächen untersucht. Die unbeschadete Aufbringung der magnetischen Moleküle wurde mit Hilfe von molekularer Aufdampfung erreicht, was ebenso das AFM-Imaging der Moleküle ermöglichte. Durch Vergleich der Ergebnisse von statischen und dynamischen magnetometrischen Messungen mit Messungen an Pulverproben wurde gezeigt, dass die Vollständigkeit der magnetischen Moleküle nicht beeinflusst wird.

Zur Erforschung der Morphologie des Dy(III) Dimers (**3**) auf Graphen-Oberflächen wurde eine ähnliche experimentelle Strategie eingesetzt. Die Abbildung der molekularen Nanomagneten auf Graphen zeigt die Existenz individuell adressierbarer Moleküle und Aggregate, vermutlich da es nur schwache Wechselwirkungen zwischen Graphen und den Molekülen gibt.

Im Gegensatz zur molekularen Evaporation ermöglicht die Selbstorganisation, dass die magnetischen Moleküle auf der Seitenwand von Single-Wall Carbon Nanotubes (SWCNTs) zur Erzeugung eines hybriden Einzelmolekülmagneten-SWCNTs-Systems anwachsen können. Die Lösbarkeit des Dy(III) Dimers (**3**) in $CHCI_3$ und DMF ermöglicht die Erzeugung zweier hybrider Systeme, nämlich **Hyb.1** und **Hyb.2**. Rasterelektronenmikroskopie (REM) und hochauflösende Transmissionselektronenmikroskopie (HRTEM) an **Hyb.1** und **Hyb.2** zeigten, dass die nanoskaligen Partikel auf der Oberfläche von der SWCNTs aufwachsen. Die Röntgenphotoelektronenspektroskopie (XPS) und die energiedispersive Röntgenspektroskopie (EDS) bestätigten die Anwesenheit von Dy(III) in beiden Systemen. Die magnetische Resonanz bei tiefen Temperaturen zeigt ein änliches Verhalten für Pulverproben dieser Hybridsysteme. Dies bietet zusätzliche Möglichkeiten für die Aufbringung dieser Hybridsysteme.

Abstract

Magnets have fascinated humans for millennia, playing a prominent role in the development of society, science and technology. When approaching the nanoscale, magnets show unconventional properties. As far as the development of molecular nanomagnets (also called Single-Molecule Magnets, SMMs), the interest in lanthanides based SMMs has been boosted since 2003.

In view of rational design of SMMs with controllable magnetic exchange interaction, molecular LEGO-like approach allows assembling the magnetic blocks, the shielding blocks and the linker blocks to produce SMMs. Mononuclear and polynuclear dysprosium(III)-based SMMs were prepared from hexafluoroacetylacetonate (hfac) and different linkers using this method, namely $Dy(hfac)_3bpy$ (bpy = 2,2′-bipyridine), **1**; $Dy(hfac)_3tBu$-bpy (tBu-bpy = 4,4′-di-tert-butyl-2,2′-bipyridine), **2**; $[Dy(hfac)_3(EtOAc)]_2bpm$ (EtOAc = ethyl acetate, bpm = 2,2′-bipyrimidine), **3** and $[Dy(hfac)_3]_3HAT$ (HAT = 1,4,5,8,9,12-hexaazatriphenylene), **4**. Only compound **3** exhibits distinct SMM behaviour under zero direct current (DC) field. Quantum tunnelling of the magnetisation (QTM) for all compounds was suppressed by an external field of 4 kOe, and frequency-dependent out-of-phase alternating current (AC) susceptibilities for all were observed, confirming SMMs behaviour. The biggest effective energy barrier to reverse the spin is obtained for **4** with the value of 84 K.

In the case of fine-tuning of magnetic properties of SMMs, we studied a series of dinuclear dysprosium(III)-based SMMs by substituting coordinated solvent molecule, sharing the general formula $[Dy(hfac)_3(R)]_2bpm$, in which R = nothing (**5**), water (H_2O, **6**), ethyl acetate (EtOAc, **3**), and methyl propionate (MP, **7**). Systematic comparison and analysis indicate that coordinated solvent molecule can influence the local geometry of dysprosium(III) ions. Nevertheless, the magnetic properties of these dimer systems were little influenced by these substitutions and the effective anisotropy barriers for all compounds were slightly increased.

Thanks to hexafluoroacetylacetonate group with enhanced volatility, the dinuclear dysprosium(III)-based SMM (complex **3**) can be deposited on various surfaces by means of molecular evaporation methodology in high vacuum. Surface technique results provide clear evidence of structural and electronic integrity of the molecules grafted on surfaces. Controllable morphology and thickness of molecules films when deposited on surfaces were achieved and characterised by AFM. Magnetic property measurements prove that the properties of deposited molecules remain unvaried. More specific, AC susceptibility measurements show that the multi-layer system maintains the same magnetic dynamics as that found in bulk samples. The successful deposition of intact SMMs on surfaces

represents the first step towards the fabrication of spintronic and optoelectronic devices based on thin films of lanthanide based SMMs.

At last, the successful experience of thermally depositing intact complex **3** on surfaces allows grafting SMMs onto graphene. The solubility of complex **3** in organic solvents makes it possible to decorate single-walled carbon nanotubes (SWCNTs) with magnetic molecules. In the case of exfoliated graphene, AFM imaging of surface-decorated graphene reveals that organisation of individual magnetic molecules can be fine designed by controlling the evaporation process. In another case of SWCNTs, combining characterisation of high resolution tunnelling electron microscopy (HRTEM), energy-dispersive X-ray spectroscopy (EDS), X-ray photoelectron spectroscopy (XPS), and Raman techniques on the hybrids SMMs–SWCNTs clearly shows **3** were grafted onto SWCNTs. Magnetic properties measurements show the paramagnetic response of the hybrid materials compared to the diamagnetic response of pure SWCNTs. All these achievements are helpful for introducing magnetic molecules into carbon nanostructure-based devices in the viewpoint of spintronic devices.

Contents

Motivation

Nowadays, the interest in nanomaterials science has dynamically increased due to the promising properties that make these nanoscale systems (in the range between one and several hundreds of nanometers) interesting for technological developments and also for fundamental researches.

Single-Molecule Magnets (SMMs), the name of which was proposed by A. Caneschi, D. Gatteschi and R. Sessoli, in 1991[1], have attracted enormous attention as nanoscale materials. Importantly, slow magnetic relaxation and distinct macroscopic quantum behaviour were observed in discrete molecules[2, 3]. These features are promising in view of possible future applications in ultra-high density memories[4, 5], quantum information processing[6, 7], and molecular spintronics[8, 9].

SMMs are of quite large importance as one key component in molecular nano-magnetism. In order to understand the mechanism, to rationally design molecular structures, and to fine-control magnetic behaviour, massive amounts of magnetic complexes have been synthesised[10–15]. Lanthanide based complexes recently attracted much attention [16, 17], since this systems may hold the key to obtain SMMs with high blocking temperatures, because of large magnetic anisotropy and magnetic moments lanthanide ions possess large magnetic anisotropy[18]. To date, considerable efforts have been dedicated to the understanding of magnetic mechanisms in SMMs which are based on bombinating 3d transition and 4f lanthanide ions[11, 19–21]. The complexity, however, of the electronic states and the non-collinearity of the single-ion easy-axes of magnetism in lanthanide(III) ions[14, 22] make it not easy to explain the magnetic relaxation dynamics in pure 4f SMMs[23, 24] and the rationalisation of the superparamagnetic behaviour of lanthanide-based molecular systems. The main reason lies in the difficultly of correlating the molecular structure with the magnetic properties of lanthanide based SMMs[25]. Therefore, a rational synthesis strategy of lanthanide based SMMs with enhanced and controllable physical properties is obligatory.

In order to render SMMs attractive as potential materials in development of quantum information devices, which utilise the spin degree of freedom of the molecules to manipulate or store information[9], significant advancements in nanostructuring and deposition of single SMM allow probing its intrinsic magnetic properties[26]. Studies on grafted SMMs onto substrates, such as nanojunctions[27–30], films[31–34], and porous materials[35], have been undertaken. Adopting appropriate SMMs and a proper grafting approach are the key points when implementing them into various nano-devices without changing their structures and corresponding magnetic properties. On the other hand, the devices should retain cleanness without being polluted or even destroyed by unknown

impurities during grafting procedure of SMMs. Therefore, finding the proper molecular systems and deposition methods is the key to achieving success towards this goal, which is the main subject of this thesis.

Despite the success of several interesting attempts to obtain isolated SMMs on surfaces [36–39], it is still a challenge to access the magnetic properties of a single magnetic molecule within a device or on a substrate surface. An alternative approach to address this issue is based on the use of single-molecule transistor geometry[40] to measure the electronic transport through individual SMMs placed between two electrodes. Along this line, notable physical phenomena such as Coulomb blockade have been observed in an individual well-known Mn_{12}OAc SMM functionalised with thiol groups[27]. Although these results are encouraging, the date seems to indicate that Mn_{12}OAc molecules intend to change when covalent bonding to surfaces. Thus maintaining the intrinsic properties and structural intactness of the investigated SMMs is a key precondition for performing the electronic transport measurement.

Dissertation Outline

This dissertation is a multidisciplinary project that consists of synthetic chemistry (through bulk magnetic and structural characterisation), surface engineering (the grafting and magnetism of SMMs on surfaces from sub-monolayer to multilayer), and finally electron transport characterisation at low temperatures through SMMs(see the outlook part).

The dissertation is therefore organised as follows:

Chapter 1 briefly gives a history tour and reviews fundamental features of SMMs, i.e. magnetic anisotropy, magnetisation dynamics, and the spin state information of free lanthanide ions. Moreover, it explains the basic working mechanism of superconducting quantum interference device (SQUID) and fundamental theory on dynamic process of slow relaxation of magnetism of SMMs. The experimental analysis techniques employed in this dissertation are also briefly introduced.

Chapter 2 introduces mononuclear and polynuclear dysprosium(III)-based SMMs were synthesised via a molecular LEGO approach. Static and dynamic magnetic properties of these complexes were measured by using a commercial SQUID magnetometry and are compared in detail.

In **Chapter 3** the effect of solvent molecule substitutions on dynamic magnetism of a series of dinuclear dysprosium(III)-based SMMs is investigated. Magnetic properties of these complexes are systematically investigated and compared.

Chapter 4 introduces a molecular evaporation approach, which allows depositing the dinuclear dysprosium(III)-based SMMs synthesised in **Chapter 2** on various surfaces, and the corresponding structures and magnetic properties of film systems from quasi-monolayer to thick layers are eventually characterised via a combination of introduced surface techniques in **Chapter 1**.

In **Chapter 5**, preparation, structure, and magnetic characterisation of the SMMs-nanocarbon hybrid materials obtained by implementing dinuclear dysprosium(III)-based SMMs into carbon nanostructures (graphene and single-walled carbon nanotubes (SWCNTs), particularly) are introduced. This work has served to establish the first step towards the fabrication of carbon nanostructures based spintronics devices involving SMMs;

Chapter 6 gives the summary of this thesis and an outlook for the future work.

1 Introduction

This chapter is divided into three parts. In the first part the history of SMMs and their fundamental features including magnetic anisotropy and magnetic relaxation dynamics (i.e. thermally activated magnetic relaxation and quantum tunnelling of the magnetisation, QTM) is briefly introduced. Since lanthanide ions play a special role in molecular magnetism, the spin state information of free lanthanide ions is presented with the goal to produce the background to investigations of the magnetic behaviour of the lanthanide-based SMMs reported in this dissertation. In the second part, several experimental characterisation techniques employed in this thesis are introduced. In the last part, the basic theory of cryogenic electronic transport through individual SMMs is reviewed.

Part I Single-Molecule Magnets

1.1 A brief history tour of SMMs

In the year 1980, a transition metal coordination compound with dodecametallic manganesesacetate cage of the formula $[Mn_{12}O_{12}(CH_3COO)_{16}(H_2O)_4]\cdot 2CH_3COOH\cdot 4H_2O$ ($Mn_{12}OAc$, Ac = CH_3COO) was structurally characterised by Prof. Tadeusz Lis, from the reaction of $Mn(CH_3COO)_2$ and $KMnO_4$ in acetic acid[41]. Its molecular structure is shown in Figure 1.1, revealing that it mainly consists of twelve Mn atoms, which are organised by an outer ring of eight Mn(III) ions and in an inner ring of four Mn(IV) ions, forming a magnetic $Mn_{12}O_{12}$ core, surrounded by sixteen acetate groups, which shield the magnetic core from neighbouring molecules. In 1991, Gatteschi et al. established magnetic properties of $Mn_{12}OAc$ via high-field electron paramagnetic resonance (EPR)[42] and a superconducting quantum interference device (SQUID) magnetometer measurements, indicating a spin ground state value $S = 10$ and zero-field splitting (ZFS) parameter D of –0.5 cm^{-1}[1]. More excitingly, it was discovered that distinct frequency-dependent imaginary components (χ'') of alternating current (AC) susceptibility are present in zero applied magnetic field[1], Figure 1.1b, indicative of slow relaxation of the magnetisation. Actually, similar behaviour is also observed in superparamagnets[43]. This relaxation follows an Arrhenius law and the process can be described well using an Argand diagram (or a Cole-Cole plot).

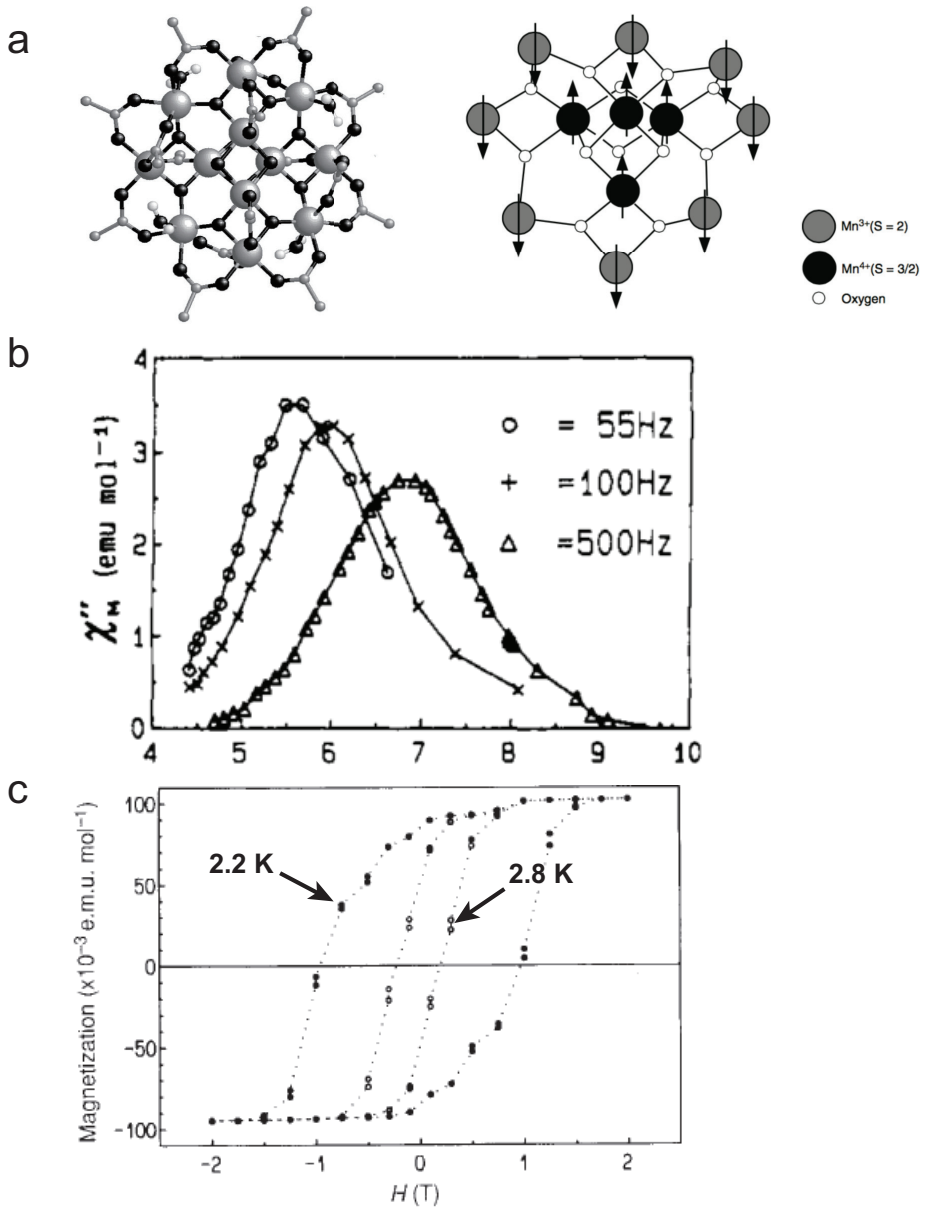

Figure 1.1: a. Molecular structure of $Mn_{12}OAc$ and chemical structure of its core. Small grey spheres are carbon atoms and black spheres are oxygen atoms. Solvent molecules are omitted for clarify. The left image is reprinted with permission from Ref. [44] and the right image is cited from Ref. [45]. b. Imaginary component (χ_M'') of AC susceptibility for $Mn_{12}OAc$ at frequencies: 55 Hz, 100 Hz and 500 Hz. Reprinted with permission from Ref. [1]. c. Its magnetic hysteresis loop characterised on a SQUID magnetometer at 2.2 K and 2.8 K (see arrows), respectively. Reprinted with permission from Ref. [46].

Two years later (in 1993), magnetic hysteresis loops (Magnetisation vs. applied field) of this molecule were observed at 2.2 K and 2.8 K for the first time[46], Figure 1.1c. The presence of magnetic bistability evidenced by hysteresis loops shows the possibility of magnetic data storage at the discrete molecule.

At milliKelvin (mK) temperatures, distinct step-like in magnetisation hysteresis loops of single crystal $Mn_{12}OAc$ samples were experimentally observed at very low temperatures for the first time[47], as shown in Figure 1.2. However, until 1996 the origin of the step-like

loops was clear, attributed to macroscopic QTM[2, 3, 48]. It seems the spins "tunnel" through it from one side to another, rather than climb over the energy barrier, which accordingly lowers the anisotropy barrier. The steps are signatures for thermally assisted, field-tuned, resonant QTM[2, 48].

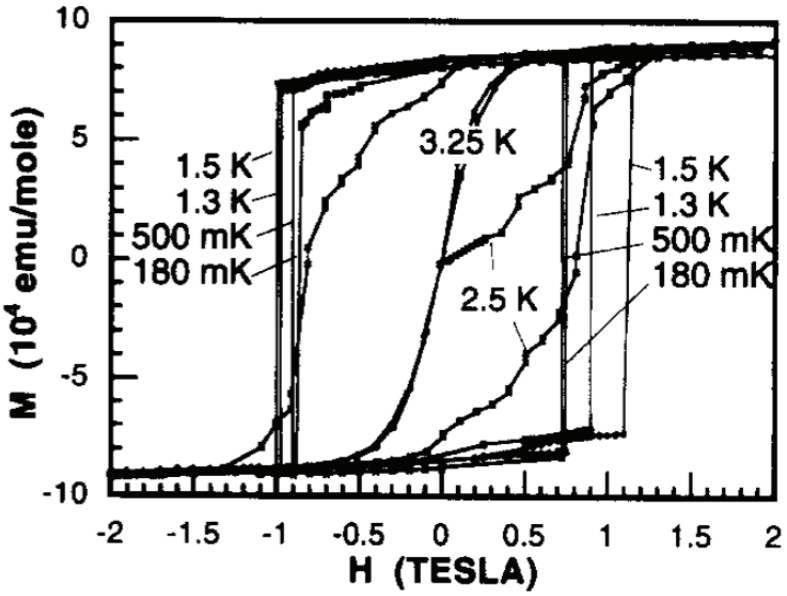

Figure 1.2: Magnetic hysteresis loops of single crystal $Mn_{12}OAc$ samples characterised in a SQUID magnetometer at various temperatures with the field sweeping at a rate of about 1 T per hour, revealing step-like transitions. Reprinted with permission from Ref. [47], Copyright 1995 Elsevier Science B.V.

In addition, the term ‘‘Single-Molecule Magnets" was proposed in 1996, defined as ‘‘all molecules that can retain their magnetisation once magnetised under an external magnetic field upon removal of the external stimuli"[49, 50].

In general, the size of nanoscale magnetic particles obtained by fragmentation of bulk ferro- or ferrimagnets such as magnetite (Fe_3O_4), are in the range from several to hundreds of nanometer (nm). This top-down approach, however, gives a distribution of particle sizes, that complicates the study of the size dependence of the properties[51]. For example, a uniform response to an external stimulus such as an applied magnetic field is precluded. The appearance of SMMs represents a breakthrough in that SMMs have more advantage over fragmented magnetic particles such that a mono-disperse domain size is ensured. Because SMMs are normally synthesised by means of solution methods and the obtained samples are in a defined size. Moreover, the SMMs are soluble and stable in common organic solvents. For example, $Mn_{12}OAc$ is dissolved and perfectly stable in acetonitrile and toluene, confirmed by proton nuclear magnetic resonance (^{1}H-NMR) spectra[52]. This provides advantages in potential applications.

The exciting discovery of $Mn_{12}OAc$ initiated developing molecular nano-materials. Since 1993, a considerable number of molecular complexes have been functionalized as SMMs. Molecular nanomagnets based on 3d, 3d/4f, and 4f ions have been widely reported[19, 20,

53–55]. Selected typical SMMs are shown in Figure 1.3.

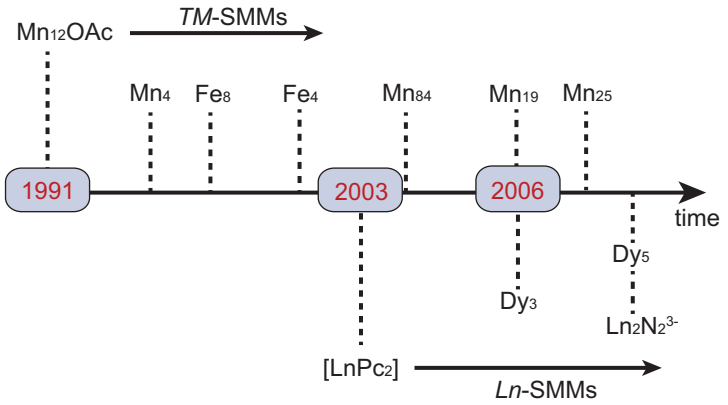

Figure 1.3: Selected reported typical SMMs with time. The examples consisting of $Mn_{12}OAc$[1] and its derivatives sharing $[Mn_{12}O_{12}(O_2CR)_{16}(H_2O)_4]$ [R = Et or Ph][52], Mn_4 with formula of $[Mn(IV)Mn(III)_3O_3X]$ (X = Cl or Br)[56], $Fe_8[(tacn)_6Fe_8O_2(OH)_{12}]^{8+}$[57], Fe_4 with formula of $[Fe_4(\mu_3\text{-}O)_2]^{8+}$[58], Mn_{84} with the formula of $[Mn_{84}O_{72}(O_2CMe)_{78}(OMe)_{24}(MeOH)_{12}(H_2O)_{42}OH_6]\cdot xH_2O\cdot CHCl_3$ [59], Mn_{19} with the formula of $[Mn(III)_{12}Mn(II)_7(\mu_4\text{-}O)_8(\mu_3,\eta^1\text{-}N_3)_8(HL)_{12}\text{-}(MeCN)_6]Cl_2\cdot 10MeOH\cdot MeCN$[60]; Mn_{25} with the formula of $[Mn_{25}O_{18}(OH)_2(N_3)_{12}(pdm)_6(pdmH)_6]Cl_2$ (pdmH = pyridine-2,6-dimethanol)[61]; $[LnPc_2]$ $[Pc_2Ln]^-TBA^+$ (Ln = Tb(III), Dy(III), Ho(III); $TBA^+ = N(C_4H_9)^+$)[62], Dy_3 $[Dy_3(\mu_3\text{-}OH)_2L_3Cl_2(H_2O)_4][Dy_3(\mu_3\text{-}OH)_2L_3Cl(H_2O)_5]Cl_5\cdot 19H_2O$ (HL = *o* - vaniliin)[63], Dy_5 $[Dy_5O(OiPr)_{13}]$[64] and $Ln_2N_2{}^{3-}$ $[\{[(Me_3Si)_2N]_2Ln(THF)\}_2(\mu\text{-}\eta^2\text{:}\eta^2\text{-}N_2)]^-$ (Ln = Gd(III), Dy(III))[65]are listed at different times. Reprinted with permission from Ref. [66], Copyright 2013 Elsevier B.V.

Particularly, since 2003, when Ishikawa et al. demonstrated slow relaxation of the magnetisation can occur in mononuclear lanthanide species[62], interests have been shifted to lanthanide based SMMs, due to their magnetic anisotropy of individual ions which arises from the unquenched orbital angular momentum. In order to well understand the magnetism of the complexes which contain lanthanide ions, the magnetism of free lanthanide ion will be briefly introduced in section 1.2.3.

1.2 Fundamental features of SMMs

1.2.1 Magnetic anisotropy

Magnetic anisotropy is a situation when the ferro-/antiferro-magnetic axis of a compound lies along fixed direction (called the easy axis). There are three kinds of anisotropies [67]: magnetocrystalline anisotropy, magnetoelastic anisotropy and shape anisotropy. According to their physical origin, the former two cases are due to spin-orbit coupling, and the last one is of dipolar origin.

In the case of SMMs, magnetocrystalline anisotropy is dominant and will be in focus here. It directly results from spin-orbital coupling in addition to the low-symmetry ligand environments about the metal ions[68]. While, dipolar effects in most SMMs are negligible due to its small magnitude.

The effective Spin Hamiltonian (SH) approach is a quantitative way on treating this anisotropy behaviour. Only the spin variables was considered in this method, while the orbital parts are included in parameters of this approach[68]. A system having $2S+1$ spin levels is used to interpret this approach. This multiplet can be split by ligand field of the appropriate Hamiltonian (ligand field Hamiltonian) and by an external magnetic field (Zeeman Hamiltonian), and the total SH can be expressed as:

$$\widehat{\mathbf{H}} = \widehat{\mathbf{S}} \cdot \mathbf{D} \cdot \widehat{\mathbf{S}} + \beta \widehat{\mathbf{S}} \cdot \mathbf{g} \cdot \vec{B} \tag{1.1}$$

where $\mathbf{D}$ is a real and symmetric and zero-field splitting tensor having three orthogonal eigenvectors, and $\widehat{\mathbf{S}}$ is a spin operator. which is connected with the magnetic field by the $\mathbf{g}$ tensor. The Zeeman perturbation (the second part of Eq. 1.1) will not be discussed here for sake of simplicity. As mentioned above, $\mathbf{D}$ has three orthogonal eigenvectors, and if the coordinate frame xyz is taken along the principal axes of $\mathbf{D}$. Then Eq. 1.1 can be written as:

$$\widehat{\mathbf{H}} = D_{xx}\widehat{S}_x^2 + D_{yy}\widehat{S}_y^2 + D_{zz}\widehat{S}_z^2 \tag{1.2}$$

where $\widehat{S}_x$, $\widehat{S}_y$, and $\widehat{S}_z$ are spin operators. The physical properties will be not changed if a constant is subtracted from a Hamiltonian. Hence, Eq. 1.2 can be written as:

$$\widehat{\mathbf{H}} = D[\widehat{S}_z^2 - \frac{1}{3}S(S+1)] + E(\widehat{S}_x^2 - \widehat{S}_y^2) \tag{1.3}$$

where the coordinate frame xyz is taken along the principal axes of the tensor $\mathbf{D}$. Its diagonal elements are related to the zero-field splitting parameters D and E, which describe the axial and rhombic components of anisotropy[69], according to the relations: where

$$D = D_{zz} - \frac{1}{2}D_{xx} - \frac{1}{2}D_{yy}$$
$$E = \frac{1}{2}(D_{xx} - D_{yy}).$$

In an axial symmetry, $D_{xx} = D_{yy}$, and thus $E = 0$, indicating the absence of transversal magneto-anisotropy in the system, one can obtain from the Eq. 1.3: $\widehat{\mathbf{H}} = D\widehat{S}_z^2$. Since $\widehat{S}$ is the eigenfunction of $\widehat{\mathbf{H}} = D\widehat{S}_z^2$, the energy of each state can be obtained by

$$E = DS_z^2. \tag{1.4}$$

The function of a negative D in Eq. 1.3 is that the system can be easily magnetised when a external magnetic field is applied along the principal axis, i.e. z-axis[68]. The energy levels can be plotted based on Eq. 1.4 as shown in Figure 1.4. A system has a ground doublet with an easy axis magnetic anisotropy, $D < 0$. And the ground doublet is characterised by $m_s = \pm S$. Two potential wells are separated by an effective anisotropy barrier, ΔE.

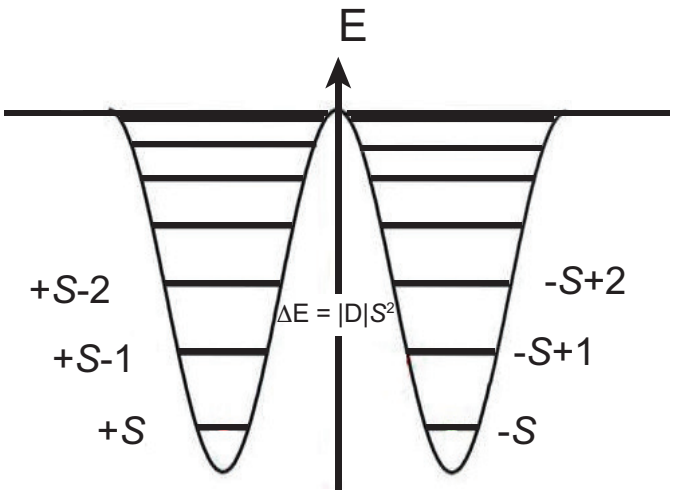

Figure 1.4: Energy levels for the $2S+1$ microlevels with negative D value in zero magnetic field.

The D value for a spin system can be experimentally obtained by means of EPR spectra, or by Inelastic Neutron Scattering (INS)[70–73]. Also magnetometry, i.e. torque[74] and SQUID magnetometer, especially when performed on single crystal samples, can provide D value.

1.2.2 The dynamics of the magnetisation

As described above, slow magnetic relaxation was firstly observed in $Mn_{12}OAc$, by means of AC susceptibility measurements at low temperatures[1]. At a sufficiently low temperature the relaxation becomes too slow, and an opening of the hysteresis loop can be observable[68]. The double well shown in Figure 1.4, can be used to interpret this dramatic slowing down of the fluctuations.

In the equilibrium state, the spin may be located either in the left or in the right potential well with the same probability. For instance, it is in the left well in Figure 1.5a. The relaxation of the magnetisation becomes slow when the spin system is cooled to low temperature, and the spin is not able to overcome the energy barrier to go into the other (the right well). On the other hand, it is much easier to achieve that at higher temperatures, since the spin system can receive energy from phonons, which help it climb the energy level step by step to overcome the potential barrier and then go down on the other side with releasing the phonons. This process is called thermally activated relaxation of the magnetisation[75].

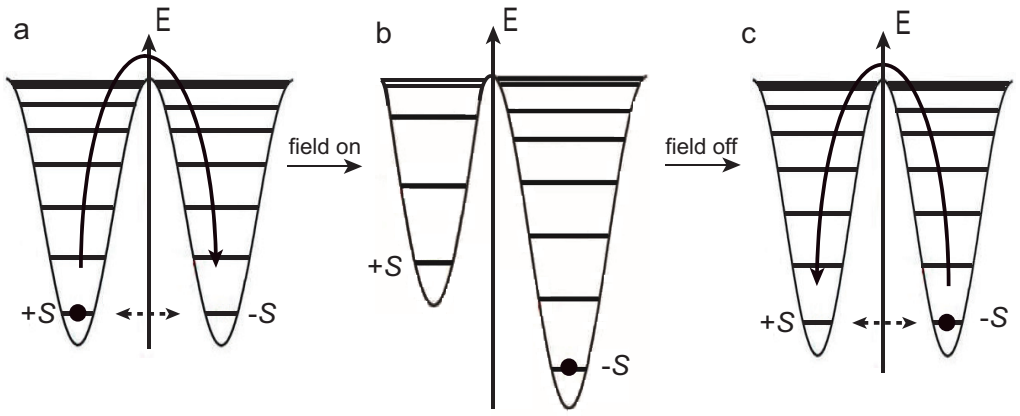

Figure 1.5: Schematic diagrams of slow relaxation of SMMs in a double well. a. one SMM stay at either in the left or in the right potential well, overcoming the barrier separating the two wells, and then go down into the right well; b. applying a magnetic field populates the right (or left) well; c. the system reestablishes a equilibrium state after removing the external fields. QTM of one SMM in a double well occurs, as shown by dished lines.

An external magnetic field enables stabilising and populating one of the two potential wells preferentially. Figure 1.5b, making one state the true ground state.

When the magnetic field is removed, an equilibrium state for the two wells (Figure 1.5c), is only reestablished by transferring part of the population[68] from one side to the other (from right to left in this case). These transitions are promoted by deformations of the coordination environment (i.e. rotations and geometrical strains) around the metal ion[68]. While, these deformations can only induce transitions between states between m_s by ± 1 and ± 2[68].

For an SMM, combination of the less populated highest energy states at low temperature and the quadratic energy spacing by Eq. 1.3 yields the relaxation time which is exponential temperature dependent[68]. This is a typical thermally activated relaxation of the magnetisation which obeys the Néel-Arrhenius law in the limit $k_B\mathrm{T} \ll U_{\mathrm{eff}}$ and a weak magnetic field[76]:

$$\tau = \tau_0 exp(U_{\mathrm{eff}}/k_{\mathrm{B}}\mathrm{T}) \tag{1.5}$$

in which τ is the relaxation time, U_{eff} is the effective energy barrier, k_{B} is Bohr magneton, and τ_0 is a pre-exponential factor which reveals the characteristic time of the thermally activated relaxation process, with the following equation,

$$\tau_0 = \frac{2\pi}{3}\frac{\hbar^2\rho c^5}{V}[\frac{S^2}{U_{\mathrm{eff}}}]^3 \tag{1.6}$$

where ρ is the density of the sample, V is the volume and c is the speed of sound in materials. τ_0 is proportional to $(S^2/U_{\mathrm{eff}})^3$. Combined with Eq. 1.4, therefore $\tau_0 \propto |\mathrm{D}|^{-3}$. This means that the relaxation time τ_0 is longer with increasing the spin S value when a anisotropy energy barrier is given. Therefore, one would expect that synthesis of clusters with large S values and magnetic anisotropy enables achieving a long magnetic relaxation time of the systems.

As a matter of the fact, besides the thermally activated relaxation process, spin reversal in SMMs can also take place via QTM[2, 48, 77] when two states possess the same energy lying on each sides of the potential wells. the probability of observing a through-barrier transition is different from zero, as shown in Figure 1.5c.

1.2.3 Magnetism of free Lanthanide ions

The internal nature of the 4f orbitals and spin-orbital coupling dominate the well-known magnetic properties of lanthanide ions[18]. To understand the magnetism of lanthanide containing complexes, the electronic structures of the 4f electrons in the free lanthanide ions must be described.

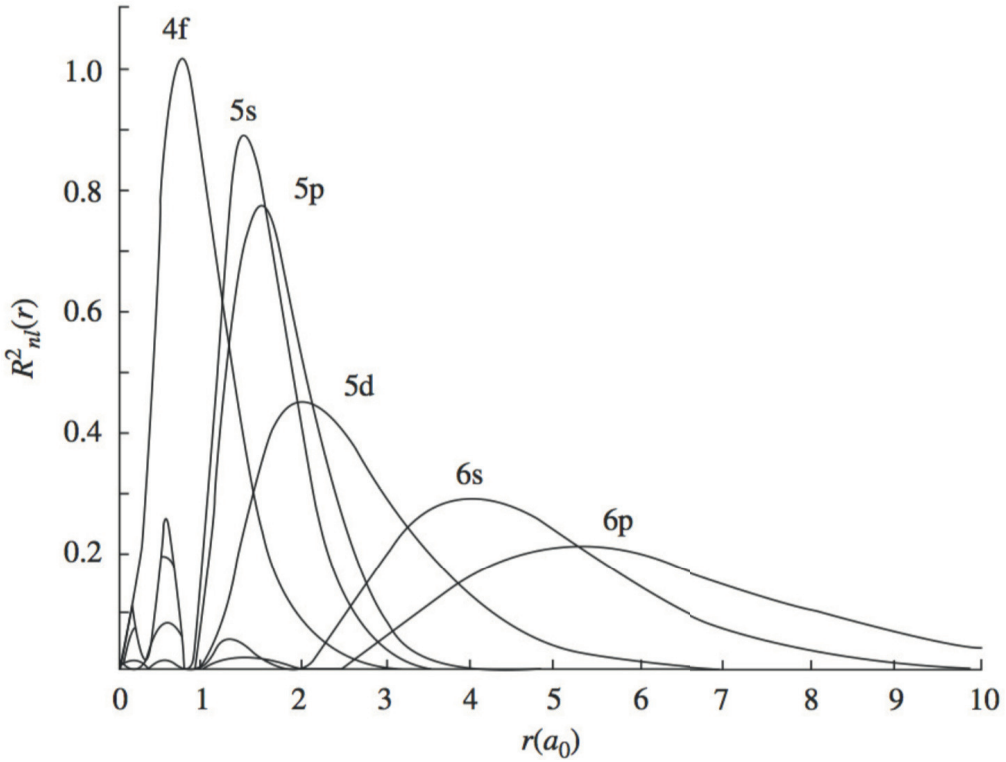

Figure 1.6: The radial distribution functions of 4f, 5s, 5p, and other orbitals for cerium. Reprinted from Ref. [78], Copyright 2010, John Wiley Sons (Asia) Pte Ltd.

Figure 1.6 shows the radial distribution of 4f wave functions for cerium. And it clearly indicates the 5s and 5p states well shield the 4f electrons. The Russel-Saunders coupling scheme is used to describe the electronic configuration of lanthanide ions[79] (i.e. dysprosium(III)), as shown in Figure 1.7.

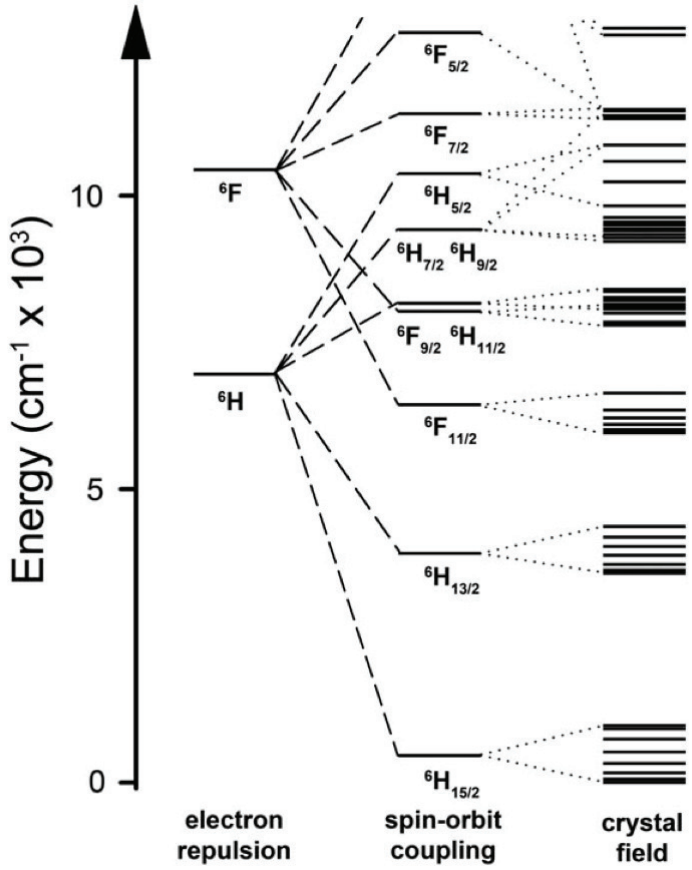

Figure 1.7: Perturbations on electronic configuration of the dysprosium(III) ion at temperatures: electron-electron repulsions, spin-orbit coupling, and the crystal field. Cited from Ref.[80], Copyright 2011, The Royal Society of Chemistry.

The trivalent lanthanide ions are characterised by $4f^n$ configurations, which give rise to ${}^{2S+1}L$ term[18]. The term can be further split by spin-orbit coupling to afford J multiplet,

$$E({}^{2S+1}L_J) = \lambda/2[J(J+1) - L(L+1) - S(S+1)] \tag{1.7}$$

in which J is limited by $|L - S| \leq J \leq L+S$, and $\lambda = \pm\, \zeta/2S$. ζ is a constant for spin-orbit coupling in the range of 600 and 3000 cm^{-1} for the lanthanide ions[18, 78]. The + sign is for $n < 7$ and – sign is for $n > 7$. In the case of f^7 ion (gadolinium(III) ion), $L = 0$ and $S = 7/2$, indicates its orbital momentum is quenched[18].

For a given lanthanide ion, three Hund′s rules can be used to determine its ground state multiplet[79]:

(1). following the Pauli exclusion principle and take maximum S;

(2). also takes its L of maximum value following a given S;

(3). When the atoms with less than half filled shells, $J = |L - S|$ lies lowest in erengy; when the atoms with more than half full filled shells $J = |L + S|$ lies lowest.

The g_J factor (also called Landé factor) of the Zeeman Hamiltonian of a given J mul-

tiplet is expressed as[18]

$$g_J = 3/2 + \frac{S(S+1) - \mathrm{L}(\mathrm{L}+1)}{2J(J+1)} \tag{1.8}$$

So far, the magnetic properties of a given system consisting of lanthanide atoms can be described based on the description above. For instance, the ground state of dysprosium(III) ion is $^6\mathrm{H}_{15/2}$, having $(2 \times 15/2 + 1) = 16$ degenerate levels. Moreover, applying a DC magnetic field H can remove these levels. The relative energy for each level can be obtained by

$$E_H = \mu_0 \mu \cdot H = -g_J m_J \mu_0 \mu_B H \tag{1.9}$$

where, μ is the atomic moment, g_J is the landé factor, m_J is the magnetic quantum number and $\mu_0 = 4\pi \times 10^{-7}$. Two adjacent levels for a given free ion are equally separated by $\Delta\mathrm{E} = \mathrm{g}_J \mu_0 \mu_B H$. Moreover, the magnetic susceptibility of lanthanide containing complexes follows the Curie law in the limit of high temperature and low magnetic field:

$$\begin{aligned} \chi &= \frac{M}{H} \\ &= \frac{N_A \mu_0 g^2 J(J+1) \mu_B^2}{3 k_B \mathrm{T}} \\ &= \frac{C}{\mathrm{T}} \end{aligned} \tag{1.10}$$

in which the C is Curie constant.

Part II Experimental Techniques

In this part, several main experimental techniques adopted for the dissertation are briefly introduced. One is for magnetic characterisation, namely Superconducting Quantum Interference Device (SQUID) magnetometer, and the another three methods for sensitive structural, electrical, and surface analysis including Matrix-Assisted Laser Desorption/Ionisation Time of Flight (MALDI-TOF) mass spectrometry, X-ray Photoelectron Spectroscopy (XPS) and Atomic Force Microscopy (AFM).

1.3 SQUID magnetometer

SQUID magnetometer is an effective and sensitive approach to measure magnetic properties of substances. A SQUID magnetometer can detect extremely weak signals by using a Josephson junction[81]. The minimum flux variation SQUID can measure is in the order of 10^{-20} Wb[82]. The Josephson junction is a junction between two superconductors, which are lightly separated by a insulating material so thin that electrons can travel from one superconductor to the other one even without an applied voltage.

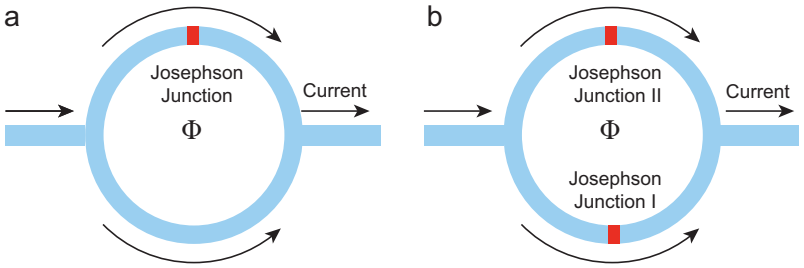

Figure 1.8: a. Schematic diagram of an radio frequency SQUID loop. It has one Josephson junction, with the insulating barrier marked by red colour; b. Schematic image of a direct current SQUID loop. It has two Josephson junctions, with the insulating barrier marked by red colour.

In 1962, Josephson proposed the electrical current density between two superconductors, which is determined by the phase difference $\Delta\phi$ of the wave functions of the two superconductors[81]. The time derivative of $\Delta\phi$ is related with the voltage between the two superconductors. In a superconducting ring interrupted by single (known as RF-SQUID[83], RF = radio frequency) or double (called as DC-SQUID[84], DC = direct current) junctions, the generated magnetic flux Φ can further affect the phase difference $\Delta\phi$. Therefore, magnetic flux can be converted into an electrical voltage in such a structure. This is how a SQUID magnetometry basically works.

1.3.1 Quantum Design MPMS XL system

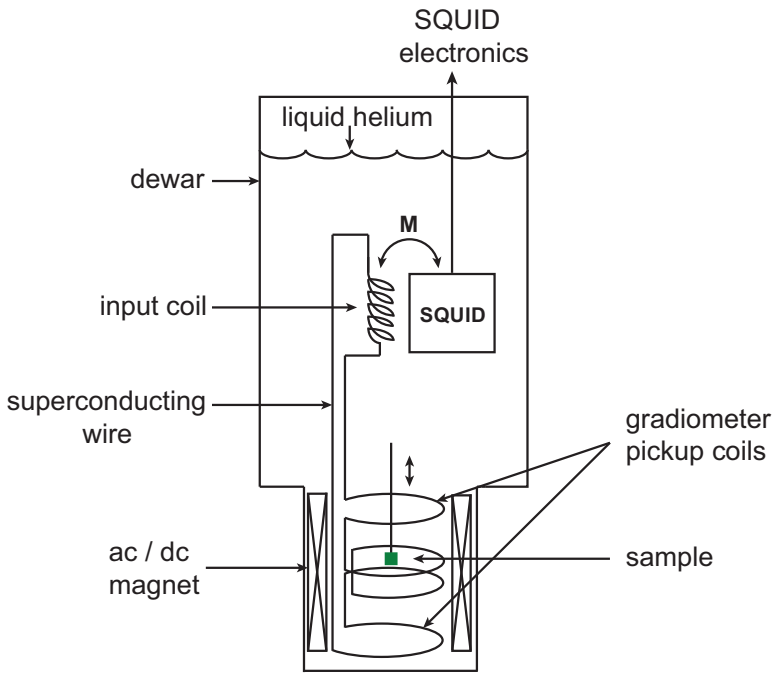

Figure 1.9: Schematic diagram of a typical SQUID magnetometer. A change in magnetic flux in the pickup coils when the sample is moved up and down, changes the magnetic field in the input coils. Then the generated magnetic flux is transferred via the input coils from the sample to a DC or AC SQUID device. Input coil and SQUID act as a magnetic flux-to-voltage converter. Then the SQUID electronics reads out this voltage.

The SQUID system used in this dissertation is a Quantum Design MPMS-XL 7 system. In addition to the classic DC and AC susceptibilities measurements, a more sensitive Reciprocating Sample Option (RSO) is installed, improving the sensitivity to 10^{-8} emu. The system is equipped with a superconducting magnet and a precise temperature control system, allowing measurements in the temperature range of 1.8 and 300 K and in fields from -7 T to 7 T.

A typical SQUID instrument is shown in Figure 1.9. The input coil and SQUID are located in the liquid helium, to maintain them in the superconducting state. Gradiometer pickup coils and the dc/ac magnet are placed at the bottom part of the system. The SQUID electronics stay in the air at room temperature.

DC measurements

In a DC measurement, the magnetic moment of the sample is measured by reading the output of the detector as the sample is moved up and down through the pickup coils. Because these movements produce an alternating magnetic flux in pick-up coils, generating the magnetic signal of the sample. Voltage readings depending on the sample positions in the pick-up coils contain the original test data. At each position, the system collects the SQUID output voltage for several times, so that multiple scans are averaged together to improve the signals resolution.

The RSO measures the magnetic properties of the substances in different way. Instead of moving the sample through the pickup coils in the common DC measurement, and stopping the motor for each data reading, the sample is moved rapidly and sinusoidally through the coils[85]. Lock-in techniques that use digital signal processor reduce the contribution of low-frequency noise to the measurement. RSO measurements can reach a sensitivity of 5×10^{-8} emu. Most of static magnetic susceptibility measurements in this thesis were done using this option.

AC measurements

A small AC oscillating magnetic field (normally 1-5 Oe) superimposed on a DC magnetic field is applied to the substances in AC magnetic measurements, causing a time-dependent magnetic moment in the substance. And the magnetic field of this moment induces a current in the pick-up coils, enabling AC magnetic measurements without any motion of the sample. The AC magnetic susceptibility is defined as $\chi = \mathrm{d}M/\mathrm{d}H$ which has both real and imaginary components, χ' and χ'' as follows:

$$\chi = \chi' - i\chi'' \tag{1.11}$$

At a low AC frequency, similar to a DC measurement, χ' is the slope of the $M(H)$ plot. χ'' shows dissipative processes inside the substance. One the other hand, at a high AC frequencies the magnetic moment of the sample does not follow the $M(H)$ curve due to the magnetic dynamic effects on the samples. The AC susceptibility is also called

dynamic susceptibility. The detailed description about this dynamic process is given in the following part.

1.4 Relaxation Dynamics

1.4.1 Dynamic equations

Researches on relaxation of magnetisation are based on the issue that the new equilibrium is established by applying a static magnetic field. This process requires a time τ. If an alternating magnetic field at high frequency is applied, the magnetisation of the samples cannot follow the changes of the magnetic field, thus lags behind in phase.

It is convenient to describe this phenomena with a applied static magnetic field H_0 parallel to the drive field with the amplitude h. Hence the applied magnetic field is expressed as,

$$H(t) = H_0 + h\cos\omega t; \tag{1.12}$$

in which $\omega = 2\pi\nu$ and ν are the angular frequency and the oscillating frequency of AC current flowing in the pickup coils. The magnetisation can be expressed by

$$\begin{aligned} M(t) &= M_0 + m\cos(\omega t - \theta) \\ &= M_0 + m\cos\omega t\cos\theta + m\sin\omega t\sin\theta \end{aligned} \tag{1.13}$$

where M_0 is the equilibrium value of the magnetisation in the field H_0. And θ is the phase angle by which the magnetisation lags behind the field.

Now we introduce χ_0, χ' and χ'' into previous M(t) equation, and a new form of M(t) is shown as below:

$$M(t) = \chi_0 H + \chi' h\cos\omega t + \chi'' h\sin\omega t \tag{1.14}$$

With the aid of Euler′s equation in the form $e^{i\omega t} = \cos\omega$t$+i\sin\omega t$, we can gather

$$H(t) = H_0 + he^{i\omega t} \tag{1.15}$$

and

$$M(t) = M_0 + \chi he^{i\omega t} \tag{1.16}$$

in which

$$\begin{aligned} \chi(\omega) &= \chi'(\omega) - i\chi''(\omega) \\ &= |\chi|e^{-i\theta} \end{aligned} \tag{1.17}$$

According to the equation 1.17, both χ' and χ'' are the function of field frequency ν and the magnitude of the DC static magnetic field H. χ' is named by high frequency susceptibility and the variation of χ' as function of frequency is the paramagnetic dispersion. χ'' is called out-of-phase signal, which is relative to the energy absorbed by the sample from

the field at high frequency[86]. In general, the decline in the in-phase components $\chi'(\omega)$ will be concomitant with the appearance of the out-of-phase component $\chi''(\omega)$ peaks, revealing slow magnetic relaxation behaviour[79].

In 1938, Casimir and du Pré proposed the following equation for the measured AC susceptibility:

$$\chi(\omega) = \chi_S + \frac{\chi_T - \chi_S}{1 + i\omega\tau} \tag{1.18}$$

To solve the equation above, one can obtain the real and imaginary components of the susceptibility:

$$\chi' = \chi_S + \frac{\chi_T - \chi_S}{1 + \omega^2\tau^2} \tag{1.19}$$

$$\chi'' = (\chi_T - \chi_S)\frac{\omega t}{1 + \omega^2\tau^2} \tag{1.20}$$

Based on the two equations above, it is clearly found that the frequency dependent χ' part is often accompanied by a χ'' part. The mathematically analogous relations between them have been determined for dielectrics by Debye. According to Eq. 1.19 and 1.20, the frequency dependence of $\chi'(\omega)$ and $\chi''(\omega)$ is shown in Figure 1.10. $\chi''(\omega)$ has a maximum, while it goes to zero following ω decreases to zero and increase to infinity. In contrary, χ' has the limiting values χ_T and χ_S.

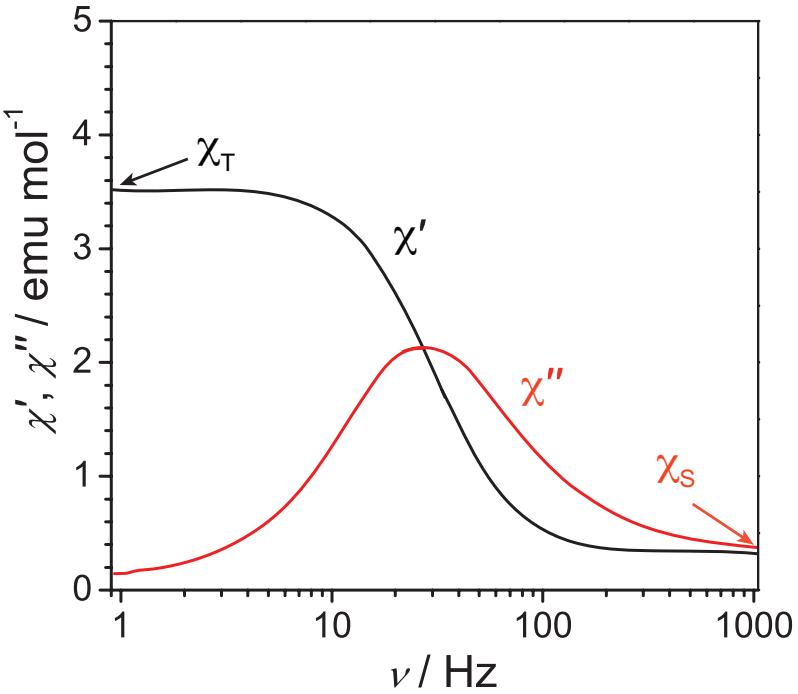

Figure 1.10: Real and imaginary components of dynamic susceptibility as a function of frequency dependence in a semi-log scale. χ_T and χ_S are the isothermal and adiabatic limit of the susceptibility, respectively.

Therefore, inspecting the temperature-dependent variation of χ' and χ'' at some investigated frequencies, is a reliable way to identifying an SMM. As depicted in Figure

1.10, with decreasing the frequency, the χ'' plot gradually increases to a maximum peak and then drops at lower frequencies, which suggests that reversal of the spin has been blocked[79].

1.4.2 Argand plots

The plot of χ'' versus χ' is called the Cole-Cole plot used for dielectrics, and known as the Argand plot in magnetism. This plot yields a semi-circle, as shown in Figure 1.11. The frequency at the top of the semicircle follows the relation $\omega^{-1} = \tau$, from which the relaxation time can be extracted.

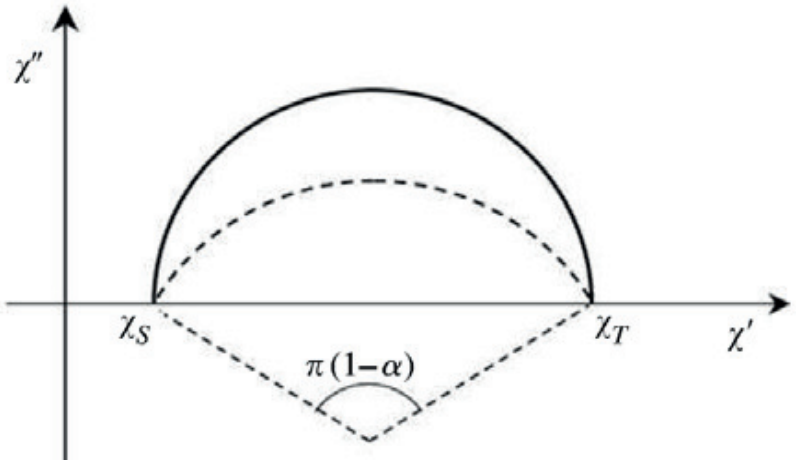

Figure 1.11: Argand plot of χ'' versus χ' at a given temperature for each frequency. Reprinted from Ref. [75], Copyright 2006, Oxford University Press.

If the imaginary χ'' does not reach the maximum in the Argand plot, it means there is the distribution of the relaxation times of magnetic relaxation process. Hence, $\chi(\omega)$ in the Eq. 1.18 is modified into the Cole-Cole equation in this case, that is:

$$\chi(\omega) = \chi_S + \frac{\chi_T - \chi_S}{1 + (i\omega\tau)^{1-\alpha}} \tag{1.21}$$

where index α changes in the range of 0 and 1. If α is zero, only one relaxation process is present in the investigated system with a single relaxation time. If α equals 1, the relaxation process is absent. So the larger α value, the wider the distribution of relaxation times. Splitting Eq. 1.21 into real and imaginary, we obtain:

$$\chi'(\omega) = \chi_S + (\chi_T - \chi_S)\frac{1 + (\omega\tau)^{1-\alpha}\sin(\pi\alpha/2)}{1 + 2(\omega\tau)^{1-\alpha}\sin(\pi\alpha/2) + (\omega\tau)^{2-2\alpha}} \tag{1.22}$$

$$\chi''(\omega) = (\chi_T - \chi_S)\frac{(\omega\tau)^{1-\alpha}\cos(\pi\alpha/2)}{1 + 2(\omega\tau)^{1-\alpha}\sin(\pi\alpha/2) + (\omega\tau)^{2-2\alpha}} \tag{1.23}$$

In experimental measurements of magnetic samples the AC susceptibility is often obtained by scanning the temperatures regarding χ' and χ'' for several selected frequencies.

The relaxation time τ and distribution index α can be obtained from fitting experimental Argand plots with Eq. 1.22 and 1.23.

When more than one relaxation process is present in the investigated system, one can also treat the data with the modified Debye model. To consider the different relaxation mechanisms interpreting the two observed χ'' signals, two different Cole-Cole equations can be expressed[87] as:

$$\chi_{total}(\omega) = \chi_S + (\chi_T - \chi_S)[\frac{\beta}{1 + (i\omega\tau_1)^{1-\alpha_1}} + \frac{1-\beta}{1 + (i\omega\tau_2)^{1-\alpha_2}}] \tag{1.24}$$

where β is the contribution factor for one relaxation process and (1-β) for the other one. This equation (1.24) can be used to fit the frequency-dependent AC susceptibilities to get the α value for each relaxation process. The real and imaginary components can be obtained by solving Eq. 1.24, shown as below:

$$\begin{aligned}\chi'(\omega) = \chi_S + (\chi_T - \chi_S)\frac{\beta(1 + (\omega\tau_1)^{1-\alpha_1}\sin(\pi\alpha_1/2))}{1 + 2(\omega\tau_1)^{1-\alpha_1}\sin(\pi\alpha_1/2) + (\omega\tau_1)^{2-2\alpha_1}} \\ + (\chi_T - \chi_S)\frac{(1-\beta)(1 + (\omega\tau_2)^{1-\alpha_2}\sin(\pi\alpha_2/2))}{1 + 2(\omega\tau_2)^{1-\alpha_2}\sin(\pi\alpha_2/2) + (\omega\tau_2)^{2-2\alpha_2}}\end{aligned} \tag{1.25}$$

$$\begin{aligned}\chi''(\omega) = (\chi_T - \chi_S)\frac{\beta(\omega\tau_1)^{1-\alpha_1}\cos(\pi\alpha_1/2)}{1 + 2(\omega\tau_1)^{1-\alpha_1}\sin(\pi\alpha_1/2) + (\omega\tau_1)^{2-2\alpha_1}} \\ + (\chi_T - \chi_S)\frac{(1-\beta)(\omega\tau_2)^{1-\alpha_2}\cos(\pi\alpha_2/2)}{1 + 2(\omega\tau_2)^{1-\alpha_2}\sin(\pi\alpha_2/2) + (\omega\tau_2)^{2-2\alpha_2}}\end{aligned} \tag{1.26}$$

1.5 Surface Analysis Techniques

To characterise the molecule-functionalised surfaces, the qualitative and quantitative chemical information as well as surface morphology are needed and can be achieved by a combination of several analysis techniques. The goal is to obtain indications of the presence of molecules on surfaces both from a topographic and a chemical point of view. Here, several powerful techniques were used in the following sections. Matrix-Assisted Laser Desorption/Ionisation Time-of-Flight (MALDI-TOF) mass spectrometry and X-ray Photoelectron Spectroscopy (XPS) are surface sensitive chemical characterisation techniques. Atomic Force Microscopy (AFM) is used to image the sample's topography.

1.5.1 MALDI-TOF mass spectrometry

MALDI is the abbreviation for Matrix-Assisted Laser Desorption/Ionisation, and it provides a quick and easy approach of molecular mass analysis using a small quantity of sample[88]. In general, the sample is uniformly mixed with appropriate matrix which can absorb the ultraviolet light (e.g. nitrogen laser light), by which a small amount of the matrix is vaporised together with the sample. TOF refers to the Time-of-Flight mass analyser which measures time it takes for the charged molecules to travel a fixed distance.

Furthermore, the ions (combination of the matrix and the analyses) of various sizes can be separated and detected depending on their different arrival time via the TOF analyser.

In a typical MALDI analysis, the sample is dissolved in the matrix and the mixture is crystallised on a sample carrier. Laser radiation vaporises and ionises this sample-matrix mixture by a short laser pulse. The matrix has two key functions. One is to absorb the energy of laser light and indirectly causing the sample to vaporise. The other one is that the matrix serves as a proton acceptor and donor, acting to ionise the sample in both positive and negative ionisation modes, respectively[89].

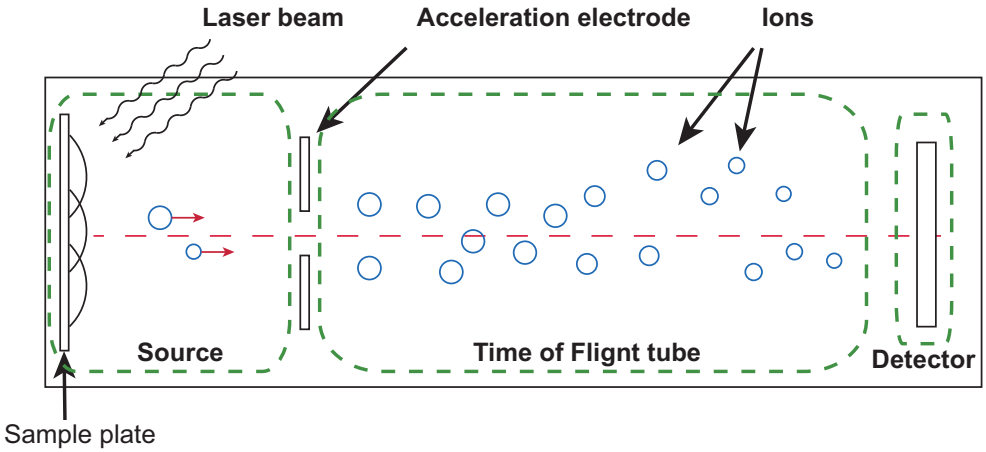

Figure 1.12: Schematic diagram of a typical MALDI-TOF mass spectrometry. It mainly contains three parts: a source, TOF tube and a detector. The mixture of sample and matrix ionised by the laser beam (marked by ions) can be positive or negative.

A schematic diagram of a typical MALDI-TOF mass spectrometry is depicted in Figure 1.12. The TOF mass analysis is based on accelerating the charged molecules towards the detector, where all ions receive the same amount of energy.

A TOF mass analyse works follow the principle that the charged molecules are accelerated in an electric field to enter a field-free TOF tube. The ions travel towards the detector at a velocity that is relative to their mass-to-charge ratio (m/z) value. Small Ions will have higher velocities than those bigger ones. This means light ions will get to the detector first.

The molecular mass, m, of the ions can be calculated according to the time it takes to travel through the fixed length L of the field-free TOF tube, after they have an energy E by being accelerated in an electric field. The relationship between E and flight time, t, is shown as below (where v is velocity of the ions):

$$E = mv^2/2 = mL^2/2zt^2$$

$$t = L(m/2zE)^{1/2} \tag{1.27}$$

Therefore, the flight time t is proportional to the molecular mass of the charged molecules in the square root form.

In our viewpoint, MALDI-TOF mass spectrometry can be considered as one of the

most powerful techniques to investigate ultrathin films of molecules on various surfaces. Particularly, this is a soft ionisation technique which holds the great advantage to identify the intact magnetic molecules on surfaces as the fingerprint information. So far, this has been widely applied to SMMs as well as patterned films proving the chemical fingerprint of the expected molecules on surfaces as well as permitting a real chemical mapping of patterned surfaces made by monolayers of molecules[90–95].

1.5.2 X-ray Photoelectron Spectroscopy

X-ray Photoelectron Spectroscopy[96], also called ESCA (electron spectroscopy for chemical analysis), is a powerful qualitative and quantitative analysis technique for surface investigation of solid samples. It provides electronic information about the elements present in a sample and on their chemical bonds, allowing the identification of the different chemical species present.

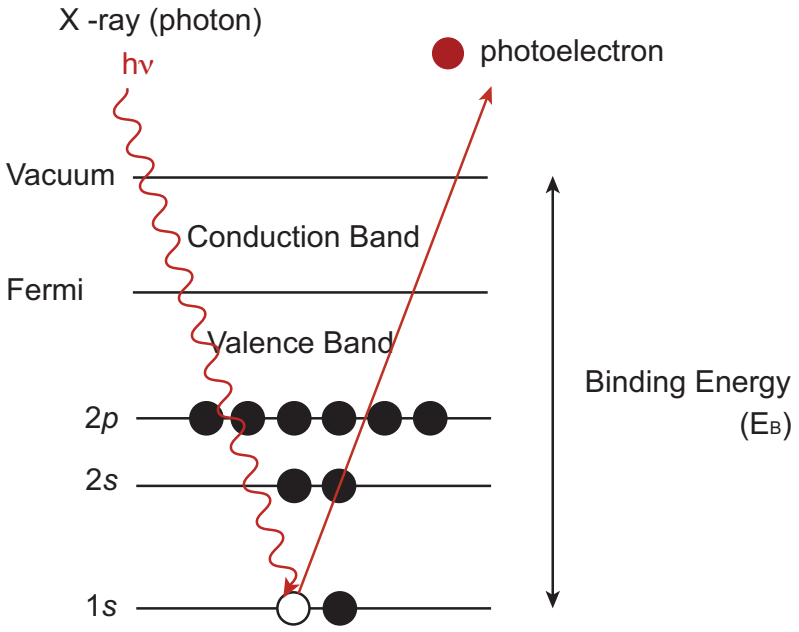

Figure 1.13: Representation of the photoemission process occurring in XPS measurements.

Briefly, XPS operates on the photoelectric effect, emission of electrons from a material when exposed to electromagnetic radiation with a frequency higher than a threshold value. Electrons obtained in this process are called photoelectrons (Figure 1.13). During the photoemission process a photon from an X-ray source transfers its energy to a core electron in the sample atom, causing its emission. The sample atom, initially with n-electrons can now rearrange its electron configuration. To get rid of the excess energy either X-ray is emitted or an electron from a higher level (Auger electron) is ejected. All emitted electrons have characteristic kinetic energies (E_K [eV]), that are relative to the atomic and molecular environment. A binding energy (E_B [eV]) is a potential barrier for an electron caused by Coulomb attraction by a positively charged nucleus. E_B depends on the distance from the nucleus (electronic level) and on the chemical bond formed between

the excited atom and its neighbours. Following the energy conservation principle, we can get a straightforward relation between the E_K and E_B in the following formula:

$$h\nu = E_B + E_K + \Phi \tag{1.28}$$

in which ν is the frequency of the radiation, for instance, $h\nu = 1486.7$ eV for Al Kα; E_B is abbreviation of binding energy of the electron defined respect to the vacuum level; E_K is the kinetic energy of the extracted photon and Φ is work function of the investigated substance.

The experimental setup consists of three major components: a vacuum chamber, an X-ray source and an electron energy analyser. The basic mechanism behind is illustrated in Figure 1.14.

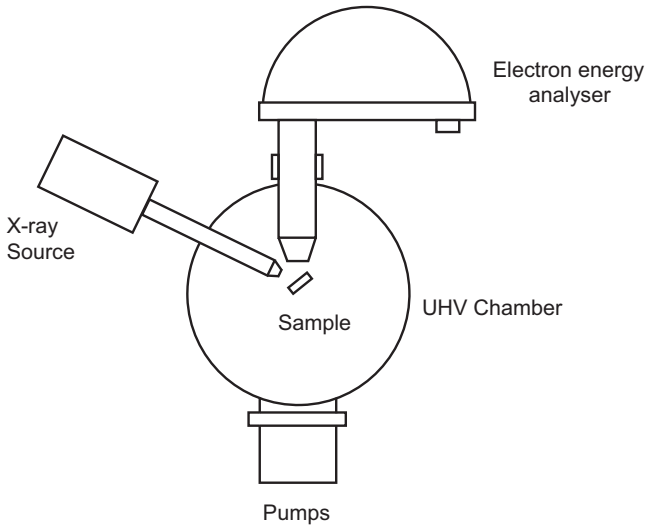

Figure 1.14: Scheme of a typical XPS apparatus. Reprinted from Ref. [92].

In the instrumental apparatus (Figure 1.14) X-rays are produced by accelerating electrons, obtained by the thermionic emission from a filament towards a metallic anode. The obtained radiation is composed by a continuum background (Bremsstrahlung) and monochromatic intense components, characteristic of the material constituting the anode (typically Mg or Al). Photoelectrons ejected from the sample irradiated by this radiation are collected and dispersed by an electrostatic analyser, which is formed by two concentric hemispheres. By varying the potential difference between the two hemispheres, the energy of electrons that can go over the trajectory toward the detector is changed. In this way electrons with different E_K are selected, each E_K corresponds to a E_B (in function of the experimental setup) and plotting the intensity of the detected signal respect to the E_B it is possible to obtain an XPS spectra. The whole process has to be performed in a ultra-high-vacuum (UHV) to preserve the surface, so that the emitted photoelectrons can travel to the detector without being scattered by gas molecules. Due to the limited inelastic mean free path of the electrons[97] in the sample (usually less than 10 nm for Al Kα X-rays) the method is highly surface sensitive and therefore suitable for the experiments

presented in this work.

The XPS spectroscopy can be used to determine the type, the concentration and the chemical state of the surface atoms. Thus, XPS has been utilised as a powerful diagnostic tool to analyse the chemical composition of ultra-thin films.

1.5.3 Atomic Force Microscopy

Scanning probing microscopy (SPM) systems have been developed and used for surface characterisation. Various types of SPM techniques mainly contain Scanning Tunnelling Microscopy (STM), and Atomic Force Microscopy (AFM), which can be used to verify the electronic and mechanical characteristics of surfaces[31]. Here, we emphasise AFM technique, as it is widely used to measure the surface structure of the substances in contrast to extreme experimental conditions such as an ultrahigh vacuum in STM for atomic resolution.

The AFM was developed by Binning, Quate, and Gerber in 1986[98] to to image surface topology and allows to study new physical phenomena at microscopic dimensions. Since then, AFM has developed into a powerful tool for direct measurements in atomic resolution, that have been used in a broad applications range such as electronics, semiconductors, materials, biology, polymers, and biomaterials. Furthermore, this technique offers additional capabilities and advantages[99] compared to other microscopic methods, like scanning electron microscopy (SEM) and tunnelling electron microscopy (TEM), in researches on metallic surfaces and micro-structures by simply accessing the nanometer scale.

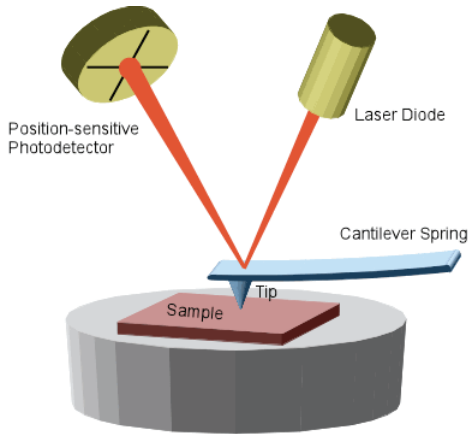

Figure 1.15: Schematic diagram of a typical atomic force microscopy (AFM). Cited from Ref. [100].

As depicted in Figure 1.15, a typical AFM system contains a micro-machined cantilever probe, a microscopic tip mounted to a cantilever spring and a position sensitive photodetector for receiving a laser beam reflected from the back of the cantilever to provide cantilever deflection feedback[99]. The underlying principle of AFM operation is the detection of the cantilever bending as a feedback or response to external forces while scanning the tip over the sample surface. Generally, interactions between the tip and the

sample surface can be distinctly identified by using a force-displacement mode. This is realised by adjusting the position between the tip and the surface.

When the distance between the tip and the surface is quite large, weak attractive forces are generated between them. When they are gradually closer, the attractive forces between them increase till the electron clouds of the tip and sample atoms begin to repel each other electrostatically[99]. As the interatomic distance continue decreasing, this repulsive force between the tip and the surface progressively makes the attractive forces weak. When the distance between the atoms of the tip and the surface reaches a couple of Angströms (Å), the interaction force becomes zero and fully repulsive when the atoms of the tip and the surface are in contact.

Based on the three interactions regimes between the tip and the surface, typically, the micro-cantilever systems are operated in three modes: contact mode, non-contact mode, and tapping mode. In the contact mode, the deflection of cantilever is kept constant while the tip remains in contact with the sample. The non-contact mode requires that the tip is oscillated at or near the natural resonance frequency of the cantilever and the amplitude of the oscillation is kept constant. At last, the tapping mode takes advantage of the two above. Compared with the former two modes, tapping mode can provide high resolution, together with minimum sample damage. Therefore, the tapping mode employed to investigate the topography and extracted other relaxant information of samples (i.e. surface roughness, film thickness).

Part III Cryogenics Electron Transport

1.6 Cryogenics Electron Transport

In the point of view of molecular spintronics[9] the aforementioned unique properties of SMMs are interesting, because they allow inserting a magnetic system with quantum properties into spintronic devices. The most difficult and important step is to integrate the magnetic molecules into the nano-devices. In most cases, these researches on integration have been undertaken by immersion of the devices in a target solution[5, 34, 101–103] or by sublimation[94, 104, 105], either before or after devices fabrication.

To measure electronic transport through individual SMMs, two different approaches, namely an *indirect* approach and a *direct* approach have been reported. In the former one, the electrons do not flow through SMMs. Instead, they flow through a proximity transport channel. In this aspect, it was achieved by using Graphene[101] and carbon nanotubes (CNTs)[106]. In contrast, in the *direct* approach employed in this work (see Outlook part), the current flows through SMMs which is directed placed between the source and drain electrodes[27, 29] (Figure 1.16).

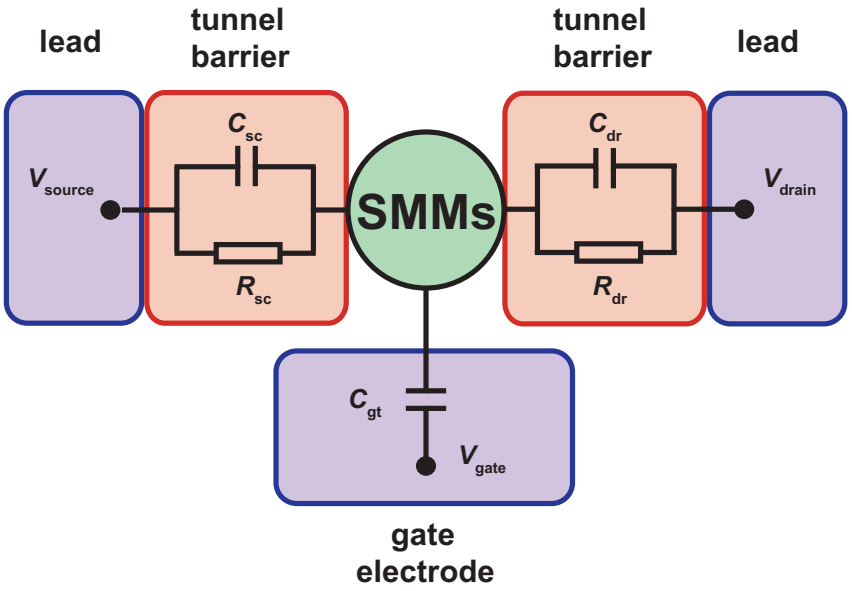

Figure 1.16: A schematic diagram of a typical single molecule transistor device. One SMM is directly placed between source and drain electrodes. A capacitance $C_{\mathrm{sc/dr}}$ and a tunnel resistance $R_{\mathrm{sc/dr}}$ are present between SMMs and electrodes. A capacitance C_{gt} is between the gate electrode and the SMM. The redox state of SMMs can be changed by applying V_{gate}. Reprinted with permission from Ref. [107], Copyright 2012, Science China Press and Springer-Verlag Berlin Heidelberg.

The magnetic molecule in a three-terminal device serves as a bridge to contact source and drain electrodes. The electrochemical potential of the two electrodes and the states of magnetic molecule can be tuned by applying a bias voltage $\mathrm{V_{bias}}$ and a gate voltage $\mathrm{V_{gate}}$, respectively. The electrochemical potentials of the source and drain electrodes can be defined as μ_{sc} and μ_{dr}. A typical schematic diagram of three-terminal device consisting of a magnetic nanomolecule and two electrodes is shown in Figure 1.17. In the case of a weak coupling between magnetic molecule and electrodes, sufficiently low temperature and a small bias voltage, molecular state is not aligned within the small bias window (Figure 1.17a). Thus, the number of the electrons on the molecule N is fixed and no current can be measured. It is possible to reduce the molecule by adding one electron to the molecule with the aid of the electrostatic field generated by the gate voltage, aiming to lower the potential of the molecule. When the condition for resonant transport is met ($\mu_{\mathrm{sc}} > \mu(\mathrm{N}+1) + \beta \mathrm{eV_{gate}} > \mu_{\mathrm{dr}}$), and the $\mu(\mathrm{N}+1)$ state is within the bias window, then one electron can hop from the source onto the molecule and off into the drain, in a two-step process[107] (centre panel of Figure 1.17a). By sweeping $\mathrm{V_{gate}}$, the molecule can be filled subsequently with electrons. This conductance measurement thus shows Coulomb blockade oscillations in the current through the molecule Figure 1.17b.

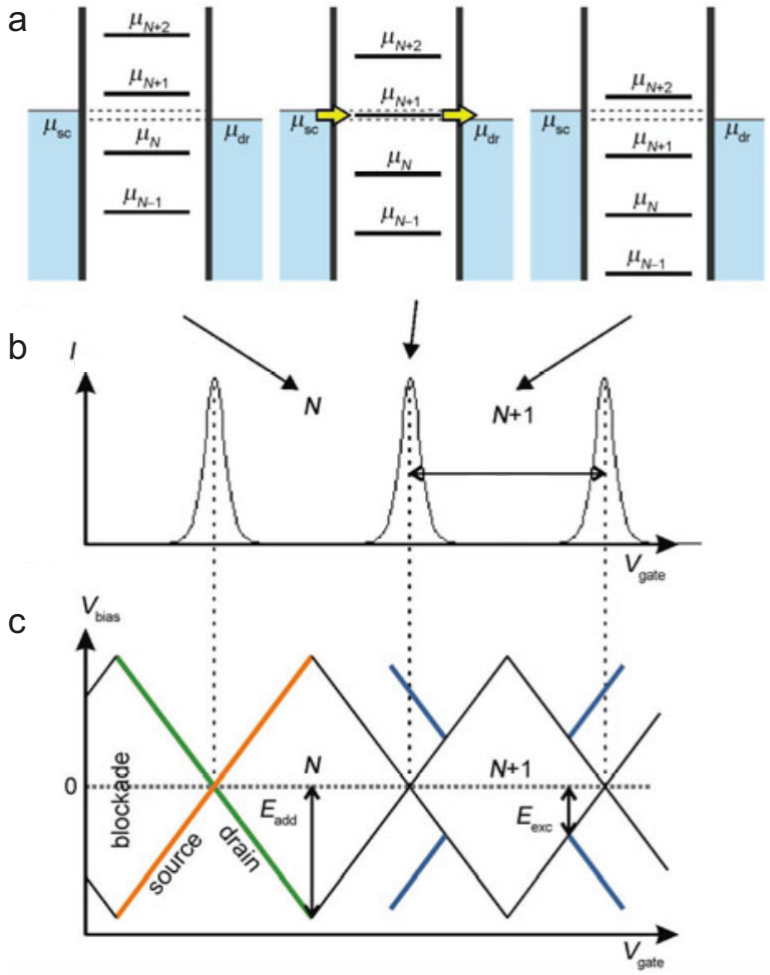

Figure 1.17: a. Schematic diagram of aligning the quantised microstates of the potential of one SMM in three different ways. The gate voltage increases from the left to right. b. Current coulomb oscillations through the SMM. c. Differential conductance $\mathrm{d}I/\mathrm{d}V_{\mathrm{bias}}$ plot showing Coulomb diamonds and excited state resonance. Reprinted with permission from Ref. [107], Copyright 2012, Science China Press and Springer-Verlag Berlin Heidelberg.

Once reaching the subsequent electron transport, the differential conductance map can be made with V_{bias} as a function of V_{gate}, generating a stability diagram of the molecule. A typical representation is shown in Figure 1.17c. The diagram contains diamond-shaped regions, also called as Coulomb diamonds. The crossing point at zero bias is named Coulomb peak or degeneracy point. Also, analogously to other spectroscopies, one can observe the excitation state of one molecule from the stability diagram and the essential information of the molecule can be extracted. For instance, the energy (E_{add}) needed to add one electron onto SMMs can be extracted from the height of the Coulomb diamonds (Figure 1.17c). Additionally, the excitations, electronic, vibrational and spin energy levels of the molecule can also be observed.

2 SMM Engineering: Molecular LEGO Approach

In this chapter, compounds **1**, **2** and **4** were synthesised by Dipl. Chem. Alexa Paretzki from Inorganic Chemistry Institute at the University of Stuttgart. The single crystal X-ray diffraction measurements were performed by Dr. Wolfgang Frey from Organic Chemistry Institute of the University of Stuttgart. Molecular structures of compound **2** were resolved by Dr. Wolfgang Frey from Organic Chemistry Institute and Dipl. Chem. Alexa Paretzki from Inorganic Chemistry Institute at the University of Stuttgart. Molecular structures of compound **3** were resolved by Shang -Da Jiang from 1st Physics Institute at the University of Stuttgart and Dr. Wolfgang Frey from Organic Chemistry Institute at the University of Stuttgart. The element analysis measurements were carried out by Ms. Barbara Förtsch from Inorganic Chemistry department of the University of Stuttgart. The MALDI-TOF mass spectra of compound **4** were measured by M. Sc. Christian Cervetti from the 1st Physics Institute of the University of Stuttgart with the help of Dr. Stephan Rauschenbach from the Max Planck Institute (MPI) at Stuttgart. The magnetic measurements on **1**, **2** and **4** were performed by Dipl. Chem. Alexa Paretzki and Dr. Lapo Bogani on a commercial SQUID magnetometry at the 1st Physics Institute at the University of Stuttgart. The low temperature magnetic hysteresis loop measurements on all complexes were performed by Dr. Wolfgang Kröner and Prof. Dr. Paul Müller at Department of Physics at Universät Erlangen-Nürnberg, Germany.

2.1 Introduction

The discovery of the first SMM $Mn_{12}OAc$ deeply inspires developing the field of molecular nanomagnetism, where amounts of transition metal and lanthanide ions containing complexes have been demonstrated to function as SMMs[19, 21, 59]. The rational design of magnetic systems has proved extremely challenging: more than forty years of work were needed to create a library of possibilities, showing how ligands affect the magnetic anisotropy of transition metal ions[108, 109] and mediate the exchange interactions between them[110].

A thorough understanding on the rational synthesis procedure towards SMMs of specific structures and on their corresponding magnetic properties is the key to the potential applications of SMMs[26]. Generally, there are two synthetic approaches to create SMMs. One is the so-called serendipitous (trial and error) method[111] that works via a reaction of metal ions with capping ligands[26]. The vast majority of SMMs were obtained in this

way. The other one is the molecular building-blocking approach that rationally assembly predesigned blocks which are able to react and associate directly[111].

In this chapter, we will introduce and further develop a approach to the synthesis of SMMs, where the magnetic building-blocks can be assembled in a veritable molecular magnetic-LEGO approach, to yield the desired magnetic properties. This behaviour-on-demand is made possible by demonstrating a minimum, complete set of building blocks that can mediate any interaction topology among a variable number of magnetic centres. Here we used dysprosium(III) ion since the ion is most used among lanthanide based complexes family. Using rare-earth centres and multi-pyridine ligands (bridging ligands), we demonstrate stepwise synthesis of SMMs of increasing nuclearity. The resulting flexibility opens ample perspectives in the rational design of both molecular magnetic materials and their hybrids.

2.2 Experimental Section

2.2.1 Magnetic LEGO approach

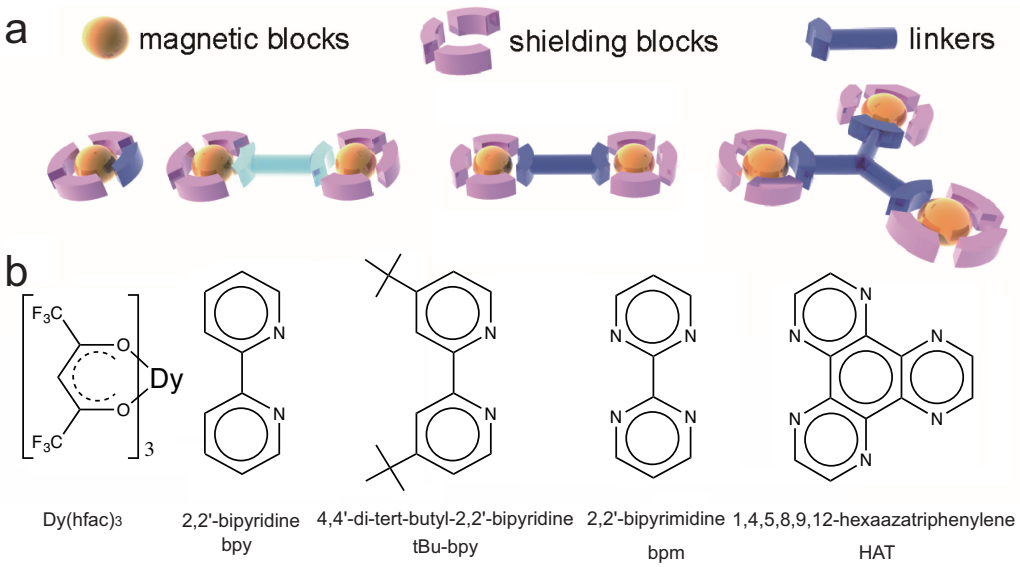

Figure 2.1: Concept and building blocks of the magnetic molecular LEGO: a. Schematic representation of the building blocks and their planned stepwise assembly. The magnetic building blocks are represented in orange, shielding elements as pink and the linking groups are blue, with light-blue blocks transmitting weaker interactions. These scheme images were made by Dr. Lapo Bogani. b. Scheme of building blocks used in this chapter, showing the $[Dy(hfac)_3]$ magnetic unit and the linking elements used: 2,2′-bipyridine (bpy), 4,4′-di-tert-butyl-2,2′-bipyridine (tBu-bpy), 2,2′-bipyrimidine (bpm) and 1,4,5,8,9,12-hexaazatriphenylene (HAT).

A basic, complete set of magnetic building blocks that can be rationally assembled, similar to magnetic LEGO bricks, is provided to create a huge variety of magnetic behaviours. To create a magnetic-LEGO, three main building blocks are required: one magnetic, one shielding, and one acting as a linker. The concept of the magnetic molecular LEGO is

shown in Figure 2.1. To produce a SMM, the magnetic block must be strongly anisotropic and reliably maintain its properties on changing the coordination sphere slightly. In this aspect, lanthanide ions are of great choices due to their large magnetic anisotropy[112]. A magnetic-LEGO system should allow substitution in specific positions, without altering the interaction pathway. The shielding blocks must be bulky, with limited mobility around the magnetic centres, so as to keep the coordination environment intact and limit the interaction between magnetic molecules. The linking blocks should not only provide the right connection between the metal ions but also transmit an appreciable, effective exchange interaction. The linkers should also allow a stepwise addition of the magnetic blocks following the pre-designed pattern.

We made use of dysprosium(III) ion and hfac ligands as bulky shielding blocks to prepare a magnetic block. The resulting dysprosium(III) trishexafluoroacetylacetonates with the formula of $Dy(hfac)_3{\cdot}2H_2O$ is a neutral building block with two or three remaining positions where an additional bidentate or tridentate ligand can coordinate. Bipyridine ligands can transmit sizeable interactions via the conjugated rings and also allow weak interaction pathways via supramolecular π-stacking interactions[113]. The existence of extensive libraries of such ligands, i.e. 2,2′-bipyridine (bpy), 4,4′-di-tert-butyl-2,2′-bipyridine (tBu-bpy), 2,2′-bipyrimidine (bpm) and 1,4,5,8,9,12-hexaazatriphenylene (HAT), with varied geometries and multiple binding sites, makes them an appealing choice as linker building blocks, Figure 2.1b.

2.2.2 Synthesis Paths

Synthesis of $Dy(hfac)_3{\cdot}2H_2O$

All reactants were used as purchased from Sigma-Aldrich without further purification. The starting reacting hydrate $Dy(hfac)_3{\cdot}2H_2O$ (hfac = hexafluoroacetylacetonate, shown in the centre of Figure 2.2) was prepared using the previously described procedure[114, 115]: 8.0 mmol (3.02 mg) of $DyCl_3{\cdot}6H_2O$ were dissolved in 10.0 ml of deionised water. A solution of $NH_4(hfac)$ was prepared by dissolving 24.0 mmol (4.99 g) of Hhfac in 100 ml of ethyl ether (Et_2O) and drop-wise adding slowly 1.78 ml aqueous ammoniac solution $NH_3{\cdot}H_2O$ ($\sim$ 0.98 g, d = 0.892 g/cm^3). The $DyCl_3{\cdot}6H_2O$ solution was added slowly into $NH_4(hfac)$ solution with fast stirring. Via multi-filtration process, the organic solvent was evaporated by reduced pressure. The resulting yellowish solid precipitate was extracted with 100 ml of boiling hexane. After cooling to room temperature naturally, the system was kept in a refrigerator and in few days the yellowish crystals were formed.

Synthesis of complexes 1-4

The magnetic-LEGO bricks $Dy(hfac)_3$ provide full interchangeability via four linking bricks including bpy, tBu-bpy, bpm and HAT following the same synthesis procedures as illustrated in Figure 2.2, according to the literature method[116].

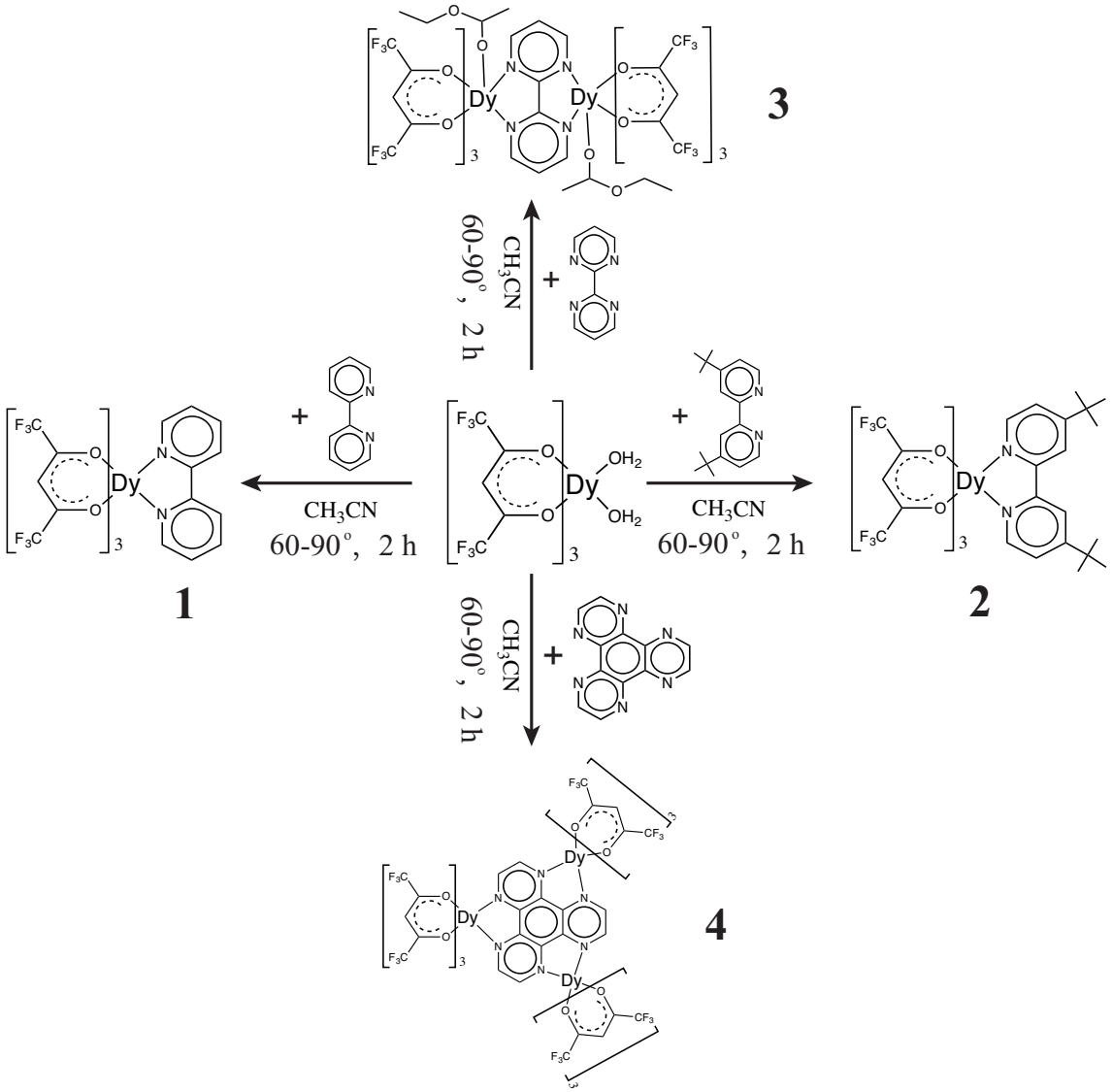

Figure 2.2: Scheme of synthesis procedures for four compounds: $Dy(hfac)_3bpy$, **1**; $Dy(hfac)_3tBu\text{-}bpy$, **2**; $[Dy(hfac)_3(ethyl\ acetate)]_2bpm$, **3** and $[Dy(hfac)_3]_3HAT$, **4**.

$Dy(hfac)_3bpy$, **1**

A 5 ml solution of acetonitrile and 2,2′-bipyridine (bpy, 1.0 mmol, 156.2 mg) was added drop-wise into a hot solution of $Dy(hfac)_3{\cdot}2H_2O$ (1.0 mmol, 819.7 mg) in 20 ml acetonitrile under stirring. After refluxing for 2 hours, the reaction was cooled naturally down to room temperature. The final solution was left still for a few days to give single crystals of compound **1**. Elemental analysis: calc. (%) for $C_{25}H_{11}DyF_{18}N_2O_6$: C, 31.95; H, 1.18; N, 2.98. Found: C, 31.65; H, 1.22; N, 2.93.

$Dy(hfac)_3(tBu\text{-}bpy)$, **2**

By using the bulky tButyl groups of 4,4′-di-tert-butyl-2,2′-bipyridine (tBu-bpy), **2** can be obtained as following: add drop-wise of a 5 ml solution of acetonitrile and tBu-bpy (1.0 mmol, 268.4 mg) into a hot solution of $Dy(hfac)_3{\cdot}2H_2O$ (1.0 mmol, 819.7 mg) in 20 ml acetonitrile under stirring. After refluxing for 2 hours, the reaction was cooled naturally

down to room temperature. The final solution was left still for a few days to give single crystals of compound **2**. Elemental analysis: calc. (%) for $C_{33}H_{27}DyF_{18}N_2O_6$: C, 38.29; H, 2.83; N, 2.57. Found: C, 38.27; H, 2.79; N, 2.63.

$[Dy(hfac)_3(ethyl\ acetate)]_2bpm$, **3**

To increase the magnetic interaction strength we can bind a second $[Dy(hfac)_3]$ center with a linker of 2,2′-bipyrimidine (bom), obtaining the binuclear **3** system by adding drop-wise of a 5 ml solution of acetonitrile and bpm (0.5 mmol, 79.1 mg) into a hot solution of 20 ml acetonitrile and $Dy(hfac)_3{\cdot}2H_2O$ (1.0 mmol, 819.7 mg) under stirring. After refluxing for 2 hours, the reaction was cooled naturally to room temperature. Volatile organic solvents were removed under reduced pressure and the dried yellowish precipitates were crystallised from ethyl acetate/heptane to give single crystals of compound **3** in a few days. Elemental analysis: calc. (%) for $C_{46}H_{28}Dy_2F_{36}N_4O_{16}$: C, 29.05; H, 1.48; N, 2.95. Found: C, 29.16; H, 1.42; N, 2.87.

$[Dy(hfac)_3]_3HAT$, **4**

The nuclearity of magnetic blocks can be extended at will by increasing the number of bidentate chelating sites, for which many examples exist[117]. The triangular complex **4**, is a particularly elegant system, which naturally expands our series. A 5 ml solution of acetonitrile and 1,4,5,8,9,12-hexaazatriphenylene (HAT, 0.5 mmol, 117.1 mg) was added drop-wise into a hot solution of 20 ml acetonitrile and $Dy(hfac)_3{\cdot}2H_2O$ (1.0 mmol, 1229.6 mg) under stirring. After refluxing for 2 hours, the reaction was cooled naturally to room temperature. The final solution was left still for a few days to give compound **4**. Elemental analysis: calc. (%) for $C_{57}H_{15}Dy_3F_{54}N_6O_{18}$: C: 26.41; H: 0.58; N: 3.25. Found: C: 26.35; H: 0.50; N: 3.18.

Elemental analyses for C, H and N were carried out with a Perkin–Elmer Analyzer 240. Matrix-assisted laser desorption/ionisation (MALDI-TOF) mass spectra were recorded with a Bruker Daltonics system. X-ray diffraction data were collected using a Bruker Kappa APEX II duo single crystal X-ray diffractometer at 110(2) K (Mo Kα radiation, λ = 0.71073 Å). Their crystal structures were solved and refined by full-matrix leastsquares techniques on F_2 by using the SHELX-97 program[118]. The absorption corrections were done numerically or by the multi-scan technique. All data were corrected for Lorentz and polarisation effects, and the non-hydrogen atoms were refined anisotropically. Hydrogen atoms were included in the refinement process as per the riding model.

DC and AC magnetic susceptibility measurements were performed on solid microcrystalline powders with a commercial Quantum Design MPMS-XL 7 system and were corrected for the diamagnetism of the sample as calculated with Pascal′s constants and the diamagnetic contribution of the sample holder, as independently determined. All samples were immobilised in Apiezon grease to prevent field orientation of the microcrystalline powders in the applied magnetic field. Magnetisation hysteresis measurements were performed using a homemade Hall probe system combined with a ^{3}He refrigerator.

2.3 Results and Discussion

2.3.1 Structural Characterization

Compound **1** was first synthesised and reported in Ref. [119]. Here we cite the CIF file of its molecular structure from the Cambridge Crystallographic Data Centre (CCDC) database with the CCDC number of 783498 in order to compare its molecular structure with those for another three compounds.

Single crystal X-ray diffraction measurements were performed on complexes **2** and **3**, except **4** due to a faster crystallisation of this complexes, which leads to big, low-quality crystals unsuited for X-ray diffraction measurement. Crystallographic parameters for **1**, **2** and **3** reported here are listed in Table 2.1. Key features, including Dy–O and Dy–N bond distances, are summarised for easy comparison in Table 2.2.

Table 2.1: Crystallographic data and refinement parameters for **1**, **2**, and **3**

Complex	**1**[a]	**2**	**3**
M_w	939.86	1052.05	1901.72
temperature (K)	110(2)	110(2)	110(2)
λ(Å)	0.71073	0.71073	0.71073
colour	colourless	colourless	colourless
crystal habit	blocks	blocks	blocks
crystal system	monoclinic	monoclinic	monoclinic
space group	$P2_1/n$	$P2_1/n$	C2/c
a, b, c (Å)	21.346(4)	13.0321(6)	31.942(3)
	18.782(4)	22.9772(1)	11.9959(9)
	16.033(3)	14.5637(3)	16.5663(1)
β (°)	106.14(3)	109.663(3)	91.123(3)
V (Å^3)	6176(2)	4103(1)	6347(9)
Z	8	4	4
D (g cm^{-3})	2.022	1.703	1.990
μ (mm^{-1})	2.572	1.945	2.508
reflns. collected	55351	80809	35977
indep. reflns.	14656	12172	9701
R[b]	0.0581	0.0516	0.0257
wR[c]	0.1478	0.1096	0.0535

[a] cited from Ref. [119].
[b] $R = \Sigma||F_o|-|F_c||/\Sigma|F_o|$
[c] $R_w = [\Sigma w(F_o^2-F_c^2)^2/\Sigma w(F_o^2)^2]^{1/2}$

Table 2.2: Crystallographic details, including selected bond distances (Å) and dihedral angles (°) for **1**[a], **2** and **3**

	2	**3**	
Dy-O1	2.337(9)	2.348(1)	2.364(2)
Dy-O2	2.335(9)	2.335(1)	2.337(2)
Dy-O3	2.320(2)	2.341(1)	2.403(2)
Dy-O4	2.358(3)	2.337(7)	2.341(2)
Dy-O5	2.327(7)	2.349(4)	2.386(2)
Dy-O6	2.344(1)	2.333(2)	
Dy-O7			2.363(2)
Dy-O8			2.375(2)
Dy-N1	2.504(1)	2.494(4)	2.589(2)
Dy-N2	2.518(2)	2.490(4)	2.599(2)
Dihedral angles (°) for **1**			
θ_1:	O1 [O2 N1] N2[b]	5.69°	
θ_2:	O3 [O4 O5] O6	2.06°	
Dihedral angles (°) for **2**			
θ_1:	O1 [O2 N2] N1	4.09°	
θ_2:	O3 [O4 O6] O5	2.12°	
Dihedral angles (°) for **3**			
θ_1	O2 [O1 N1] N2	13.89	
θ_2	O4 [O3 O5] O6	0.99	

[a] cited from Ref. [119].
[b] A [B C] D is dihedral angle between ABC plane and BCD plane;

Molecular Structure of Dy(hfac)$_3$bpy, 1

Molecular structure of **1** is shown in Figure 2.3a. This Dy(hfac)$_3$bpy species crystallises in the space group P21/C[119]. Two bpy ligands of the adjacent complexes lie with the aromatic planes perfectly parallel at 3.741 Å as calculated between the centroids of the adjacent bpy ligands, indicating intermolecular π-stacking interaction is introduced in **1**. Looking at the positions of oxygen atoms and nitrogen atoms about the Dy(III) ion, the coordination geometry can be described as a distorted square anti-prism, Figure 2.3b. Dy-O(hfac) distances support this distortion, ranging from 2.320(2) to 2.358(3) Å (av. 2.337(3) Å), which are in good agreement to those of other previously reported lanthanides complexes containing Dy(hfac)$_3$ unit[119–122]. The O-Dy-O angles vary from 72.3(4) to 145.4(7)°. The two inter-planar are defined as O1-O2-N1-N2 plane and O3-O4-O5-O6 plane and the distance between the centroids of two planes is 2.554 Å. Moreover, The planarity of the square is characterised by the dihedral angle θ. The θ value between

the two planes is 2.74°, indicative of plane-parallel approximation in the distorted square anti-prism. The shortest intermolecular Dy...Dy distance is 8.073 Å.

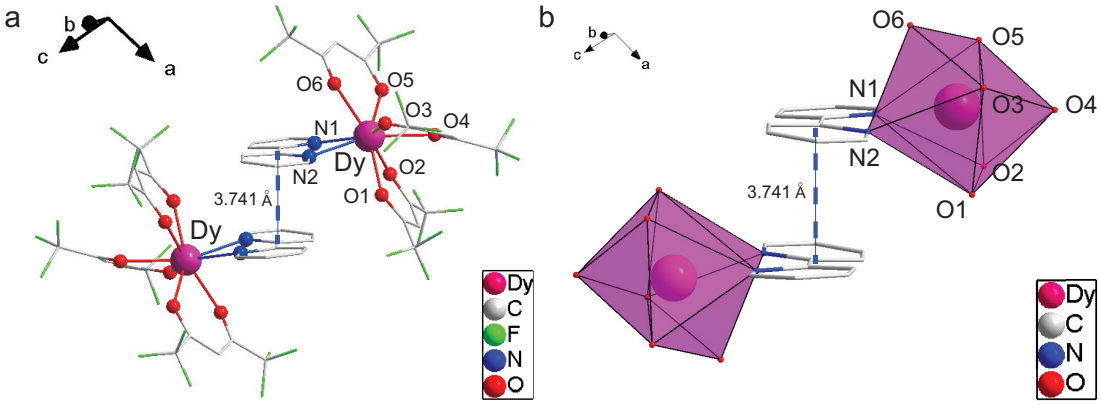

Figure 2.3: a. Molecular structure of **1**. The distance between the centroids of two bpy planes is 3.741 Å. b. Coordination environment of Dy(III) atom. The dihedral angle θ and distance between the centroids of O3-O4-O5-O6 plane and O1-O2-N1-N2 plane are 2.74° and 2.554 Å, indicative of plane-parallel approximation in the distorted square anti-prism. The molecule was synthesised and reported in Ref. [119]. We cite the CIF file of its molecular structure from the Cambridge Crystallographic Data Centre (CCDC) database with the CCDC number 783498.

Table 2.3: Selected bond Angles (°) for **1**[a]

O1-Dy-O2	72.6(9)	O1-Dy-O3	76.1(7)
O1-Dy-O4	78.8(4)	O1-Dy-O5	149.5(8)
O1-Dy-O6	137.7(1)	O1-Dy-N1	107.4(9)
O1-Dy-N2	74.7(3)	O2-Dy-O3	138.0(1)
O2-Dy-O4	74.1(6)	O2-Dy-O5	80.9(0)
O2-Dy-O6	145.4(7)	O2-Dy-N1	74.4(7)
O2-Dy-N2	115.2(9)	O3-Dy-O4	72.7(3)
O3-Dy-O5	117.1(1)	O3-Dy-O6	76.1(7)
O3-Dy-N1	149.9(4)	O3-Dy-N2	81.9(3)
O4-Dy-O5	79.6(5)	O4-Dy-O6	120.3(5)
O4-Dy-N1	144.2(4)	O4-Dy-N2	146.9(8)
O5-Dy-O6	72.3(4)	O5-Dy-N1	78.8(6)
O5-Dy-N2	131.8(4)	N1-Dy-N2	64.5(1)

[a] cited from Ref. [119].

Molecular Structure of Dy(hfac)$_3$tBu-bpy, 2

Molecular structure of **2** is shown in Figure 2.4a and selected bond lengths and angles are summarised in Table 2.2. This species crystallises in the monoclinic P1 2_1/n group with Z = 4. Each dysprosium centre was octa-coordinated by six oxygens of three hfac

ligands and two nitrogen atoms of the chelating tBu-bpy which both provide good magnetic shielding on the Dy(III) ion. The Dy–O(hfac) distances in the range of 2.349(4) and 2.333(2) Å in **1**, and the Dy–N distances are 2.494(4) and 2.490(4) Å. The average Dy–O(hfac) distance of 2.345(7) Å is shorter than the average Dy–N distance of 2.492(4) Å. The O-Dy-O angles are in the range of 72.3(7) and 150.2(9)°. The coordination geometry of Dy(III) ion is shown in (Figure 2.4b). O1-O2-N2-N1 and O3-O4-O6-O5 are the two square basic planes of the anti-prism. The dihedral angle θ between the two planes is 3.77°, indicating closely parallel planes. The distance between the centroids in two planes is 2.558 Å, which is much shorter than that of the edge length of square O1-O2-N2-N1 (av. 2.848 Å) and O3-O4-O6-O5 (av. 2.817 Å). Thus, the coordination arrangement is best described as a slightly compressed square anti-prism. The shortest intermolecular Dy...Dy distance is 8.069(2) Å.

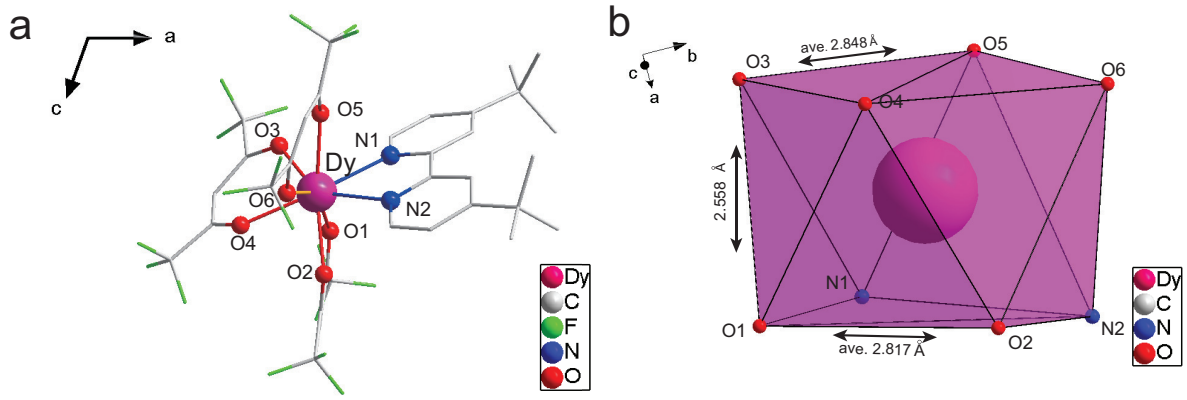

Figure 2.4: a. Molecular structure of **2**. b. Coordination environment about Dy(III) ion. The dihedral angle θ and distance between the centroids of O1-O2-N2-N1 plane and O3-O4-O6-O5 plane are 3,77° and 2.558 Å, indicative of plane-parallel approximation in the distorted square anti-prism. This crystal structure of **2** were resolved by Dipl. Chem. Alexa Paretzki from Inorganic Chemistry Institute at the University of Stuttgart and Dr. Wolfgang Frey from the Organic Chemistry department of the University of Stuttgart.

Table 2.4: Selected Bond Angles (°) for **2**

O1-Dy-O2	72.7(2)	O1-Dy-O3	73.0(5)
O1-Dy-O4	80.2(8)	O1-Dy-O5	136.8(1)
O1-Dy-O6	150.2(9)	O1-Dy-N1	73.3(9)
O1-Dy-N2	108.2(0)	O2-Dy-O3	135.4(1)
O2-Dy-O4	74.1(6)	O2-Dy-O5	73.8(8)
O2-Dy-O6	81.0(7)	O2-Dy-N1	133.7(8)
O2-Dy-N2	74.5(2)	O3-Dy-O4	72.9(2)
O3-Dy-O5	75.5(4)	O3-Dy-O6	120.2(1)
O3-Dy-N1	82.2(5)	O3-Dy-N2	144.1(8)
O4-Dy-O5	117.4(4)	O4-Dy-O6	79.1(9)
O4-Dy-N1	148.0(8)	O4-Dy-N2	142.8(5)
O5-Dy-O6	72.3(7)	O5-Dy-N1	73.6(6)
O5-Dy-N2	81.6(5)	N1-Dy-N2	64.8(5)

Molecular structure of $[Dy(hfac)_3(ethyl\ acetate)]_2bpm$, 3

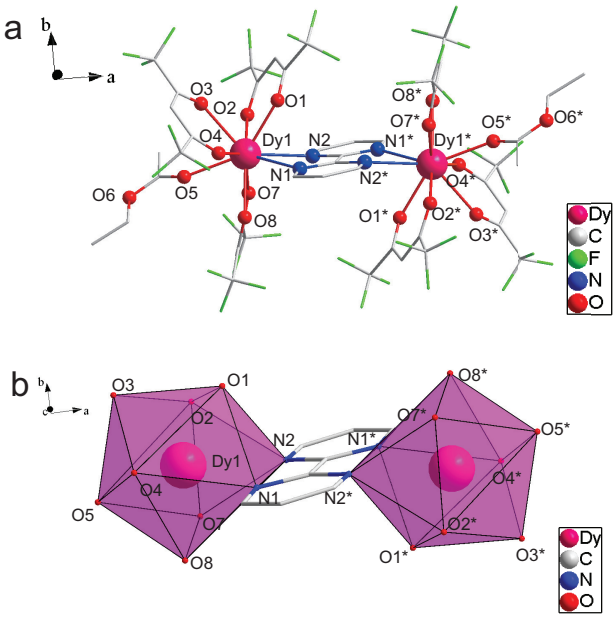

Figure 2.5: a. Molecular structure of **3**. Hydrogen atom are omitted for clarify. b. The coordination geometries about dysprosium atom in **3**. The dihedral angles between O7–O8–N1 plane and O8–N1–N2 plane is 11.01° and that between O5–O4–O2 plane and O4–O2–O1 plane of 3.06°, indicating planarity of the corresponding squares. The two square planes defined as O1–O2–O4–O5 and N1–N2–O7–O8, and O3 from one hfac ligand sits on the capping position. Symmetry-equivalent positions are denoted by a star ⋆ in the label. This crystal structure of **3** were resolved by Shang -Da Jiang from 1st Physics Institute at the University of Stuttgart and Dr. Wolfgang Frey from the Organic Chemistry department of the University of Stuttgart.

Table 2.5: Selected Bond Angles (°) for **3**

O2-Dy1-O4	86.0(6)	O1-Dy1-O3	67.3(6)
O2-Dy1-O7	133.9(6)	O8-Dy1-O3	134.0(6)
O4-Dy1-O7	139.5(6)	O5-Dy1-O3	70.1(6)
O2-Dy1-O1	74.3(6)	O2-Dy1-N1	67.6(6)
O4-Dy1-O1	137.6(6)	O4-Dy1-N1	74.9(6)
O7-Dy1-O1	72.6(6)	O7-Dy1-N1	110.4(6)
O2-Dy1-O8	134.6(5)	O1-Dy1-N1	127.2(6)
O4-Dy1-O8	74.5(6)	O8-Dy1-N1	67.9(6)
O7-Dy1-O8	71.3(6)	O5-Dy1-N1	137.8(6)
O1-Dy1-O8	143.9(6)	O3-Dy1-N1	128.2(6)
O2-Dy1-O5	142.1(6)	O2-Dy1-N2	71.2(6)
O4-Dy1-O5	78.5(6)	O4-Dy1-N2	136.5(5)
O7-Dy1-O5	71.8(6)	O7-Dy1-N2	68.6(6)
O1-Dy1-O5	94.4(6)	O1-Dy1-N2	71.6(6)
O8-Dy1-O5	73.8(6)	O8-Dy1-N2	95.5(6)
O2-Dy1-O3	72.1(6)	O5-Dy1-N2	140.3(6)
O4-Dy1-O3	71.0(6)	O3-Dy1-N2	130.5(6)
O7-Dy1-O3	120.9(6)	N1-Dy1-N2	62.4(6)

Adding an additional chelating sites allows linking two magnetic blocks, complex **3** crystallises in the C 2/c group, with an inversion centre on the bpm bridge. The selected bond parameters are listed in Table 2.2. In each molecule, three hfac ligand provides six donor oxygen atoms coordinating to each Dy(III) ion, and the other three coordination sites are occupied by two nitrogen atoms from the bridge ligand bpm and one oxygen atom from ethyl acetate, respectively. Dy–O(hfac) bond lengths in the range of 2.337(2)–2.403(2) Å, and Dy1–O(EtOAc) (Dy1–O5) is 2.386(2) Å. The O-Dy-O angles are between 67.3(6) and 143.9(6)°. The Dy-N1 and Dy-N2 bond lengths are 2.589(2) and 2.599(2) Å, respectively. Taking into account the positions of the oxygen atoms and the nitrogen atoms, the coordination geometry about central Dy(III) ion can be described as a distorted mono-capped square anti-prismatic configuration, where the two square planes are defined as the O1-O2-O4-O5 and N1-N2-O7-O8, and O3 from one hfac ligand sits in the capping position (see Figure 2.5b). The dihedral angle θ and distance between the two planes are 1.69° and 2.525 Å, respectively. All bond distances are similar to those found in **1** and **2**. The intramolecular Dy...Dy distance is 6.767(1) Å. In general, the Dy–O(hfac) bond distances tend to be shorter than the Dy–N bond distances, as expected based on the negative charge of the hfac ligand compared to the neutral tBu-bpy and bpm ligands.

Molecular Structure of $[Dy(hfac)_3]_3$HAT, 4

As mentioned before, a faster crystallisation of the compounds when the strategy is expanded to three magnetic centres (**4**) or more, leads to big, low-quality crystals unsuited for X-ray diffraction measurement. This is hardly a problem, as the combined use of element analysis, MALDI-TOF mass spectra and magnetic data analysis allows clear determination of the nuclearity of the complexes. Mass spectra collected in a negative reflector mode show signals at m/z = 2585 that correspond to the cluster ion $[M]^- = [Dy(hfac)_3]_3(HAT)$ and its selected fragments $[M\text{-}5F]^-$, $[M\text{-}1Dy(hfac)_3]^-$ and $[M\text{-}2(hfac)\text{-}bpm\text{-}Dy\text{-}H]^-$ (Figure 2.6). The isotopic distribution of the $[M]^+$, $[M\text{-}5F]^-$, $[M\text{-}1Dy(hfac)_3]^-$ and $[M\text{-}2(hfac)\text{-}bpm\text{-}Dy\text{-}H]^-$ signals is present, listed in Figure 2.6 and Table 2.6, confirming the proposed molecular structure, and unambiguous assignment of selected typical peaks is possible.

Table 2.6: Characteristic peaks detected in the negative channel of MALDI-TOF mass spectra of complex **4**, with their assignments.

Mass[amu]	Assignment	Fragments
2585	$[M]^-$	$[Dy(hfac^*)_3]_3(HAT)^{**}$
2491	$[M\text{-}5F]^-$	$[Dy(hfac)_3]_2(HAT)[Dy(hfac)_2](C_5HFO_2)$
1801	$[M\text{-}1Dy(hfac)_3]^-$	$[Dy(C_5HF_6O_2)]_3(HAT)$
990	$[M\text{-}2(hfac)\text{-}bpym\text{-}Dy\text{-}H]^-$	$Dy(hfac)_4$

* hfac = hexafluoroacetylacetonate (Formula: $C_5HF_6O_2$)
** HAT = 1,4,5,8,9,12-hexaazatriphenylene (Formula: $C_{12}H_6N_6$).

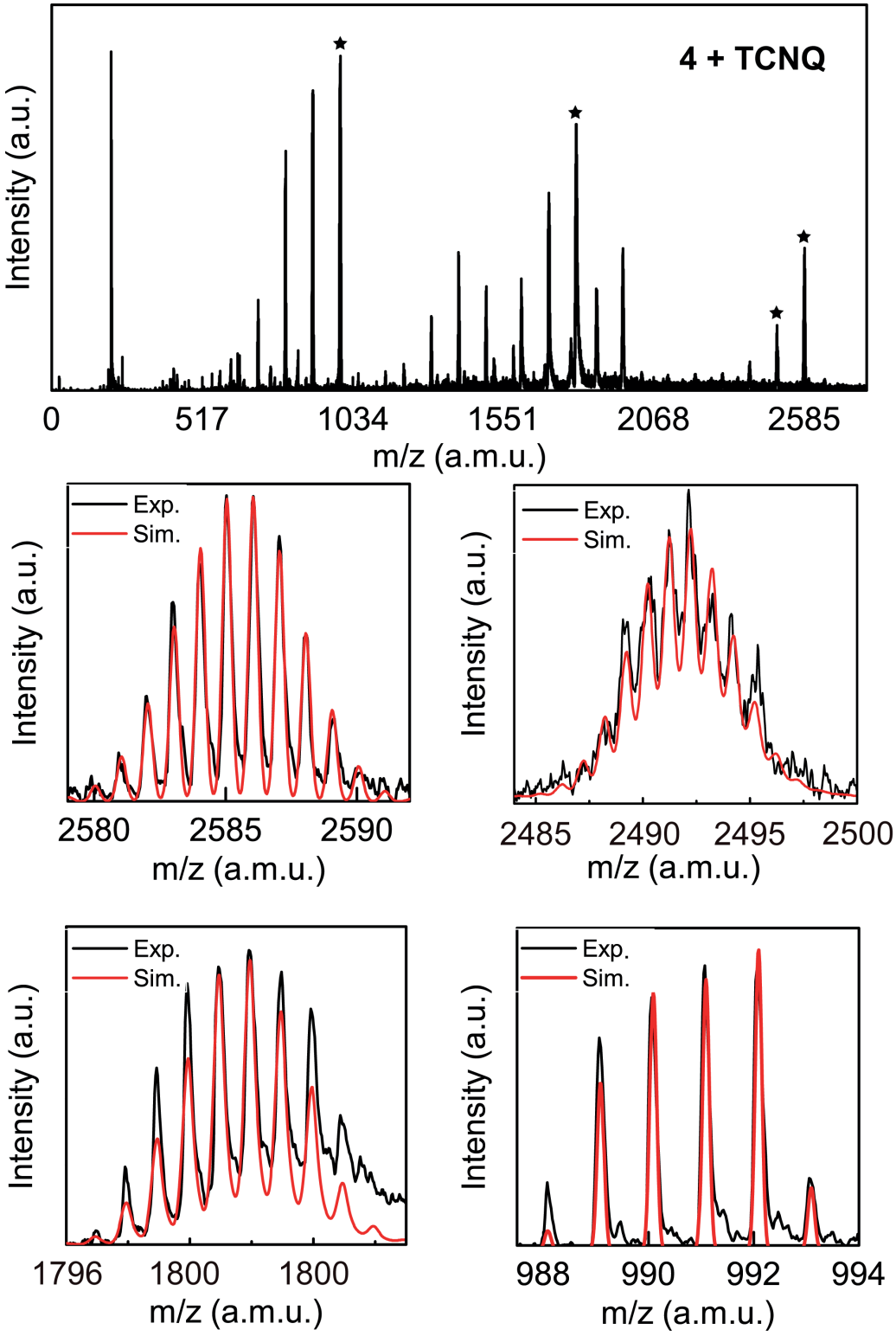

Figure 2.6: MALDI–TOF mass spectra of complex **4** in the negative ion model. Experimental (black) and calculated (red) isotopic distribution of $[M]^-$, $[M\text{-}5F]^-$, $[M\text{-}1Dy(hfac)_3]^-$ and [M-2(hfac)-bpm-Dy-H]$^-$. This mass spectra of compound **4** were performed by M. Sc. Christian Cervetti from the 1st Physics Institute of the University of Stuttgart with the help of Dr. Stephan Rauschenbach from the Max Planck Institute at Stuttgart.

2.3.2 Magnetic properties

Static magnetic properties

In order to probe into the magnetic properties of **1** – **4**, static magnetic susceptibility measurements for each compound were performed on powder samples under a static field of 0.1 T in the range of 300 – 1.8 K. The products (χ_MT) of temperature (T) with the molar magnetic susceptibility (χ_M) for **1** – **4** are given in Figure 2.7a.

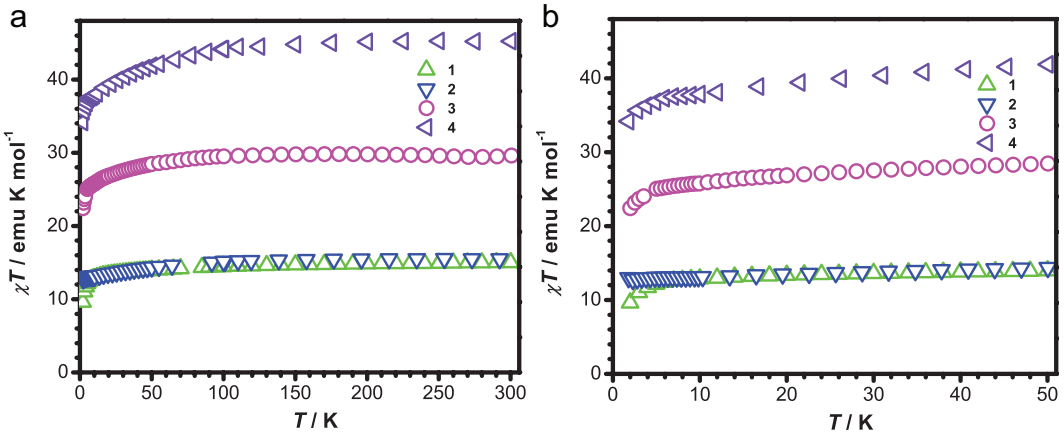

Figure 2.7: a. χ_MT product versus temperature for compounds **1** – **4** between 1.8 and 300 K. All curves were acquired with a static magnetic field of 0.1 T. b. χ_MT curve under 50 K. The static properties of compounds **1**, **2** and **4** were performed by Dipl. Chem. Alexa Paretzki and Dr. Lapo Bogani at the 1st Physics Institute of the University of Stuttgart, Germany.

At room temperature, the χ_MT values of **1** – **4** are 15.01, 15.49, 29.6 and 45.2 emu K mol^{-1}, respectively. These values are in good agreement to the theoretical value 14.17 emu K mol^{-1} for one Dy(III) ion, 28.34 emu K mol^{-1} for two non-interacting Dy(III) ions and 42.51 emu K mol^{-1} for three free Dy(III) ions[18]. On cooling down to ca. 80 K, the χ_MT product remains almost constant, before rapidly decreasing to a minimum of 9.61 (**1**), 12.99 (**2**), 22.42 (**3**), and 34.16 (**4**) emu K mol^{-1} at 1.8 K, respectively (Fig. 2.7b). Such behaviours are likely due to the progressive thermal depopulation of the excited Stark sublevels of the ground state of the Dy(III) ion[123, 124]. Comparison between **1** and **2** shows almost same behaviour, with the same progressive depopulation of the Stark sub-levels, confirming the robustness of hfac ligand as the magnetic shielding and terminal blocks.

We carried out Hall probe studies on magnetisation hysteresis of complexes **1** – **4**. Generally, in the hysteresis loop measurements, a external magnetic field aligns the magnetic moments of the samples achieving a saturation state. After that, the magnetic field is recycled from the high field to zero field. And it continues going to the negative fields and then back to positive ones. The width of the magnetic hysteresis loops is influenced by two factors temperature and sweep rate of the magnetic field. Therefore, we cycled the applied magnetic fields at sweep rate 50 mT s^{-1} at different temperatures.

The hysteresis loops and their corresponding derivative plots are shown for complexes **1** – **4** (Figure 2.8), indicating temperature dependent behaviour. For all complexes, a

butterfly-shaped loop is observed, which is attributed to the fast magnetisation tunnelling process occurring near the zero field[95]. Specifically, for **1** and **3**, it is possible to observe two-step hysteresis loops at around 0.2 T and close to zero. These are evident by the presence of equivalent peaks in the derivative plots in Figure 2.8. The presence of the hysteresis loops indicates that below 2.7 K (**1**), 1.5 K (**2**), 2.1 K (**3**) and 1.5 K (**4**) the magnetisation of all compounds is blocked. The largest magnetic hysteresis loop for each complexes opens at 0.3 K. This kind of behaviour is the fingerprint of SMMs[125] for all complexes. The loops steps arises from the fast relaxation of the magnetisation at avoided level crossings and/or QTM[126]. These studies indicate that **1** and **3** also have an easy axis of magnetisation and undergo much faster relaxation, in agreement with the AC susceptibility measurements (see below).

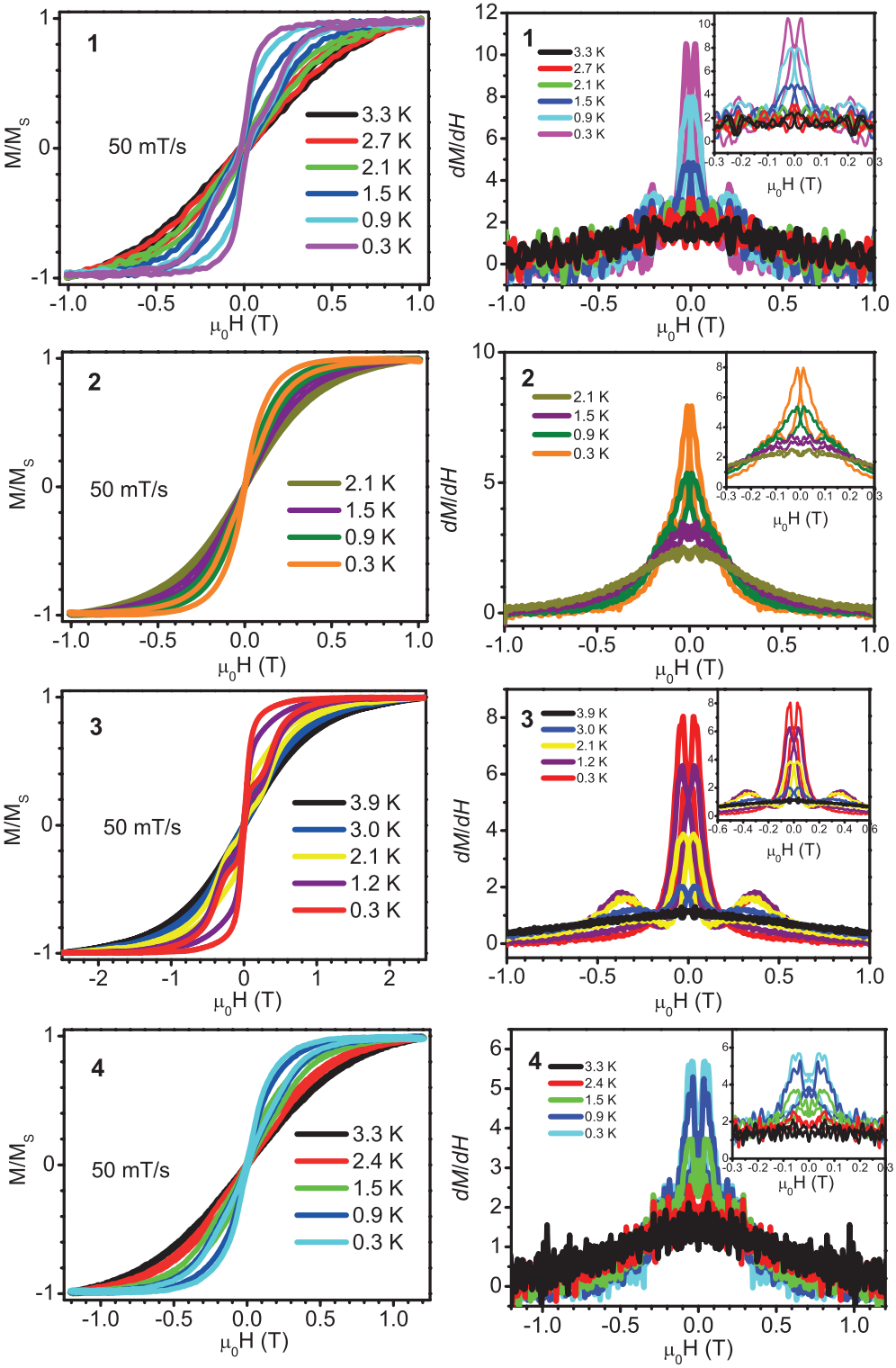

Figure 2.8: (left) Low temperature dependence of the hysteresis loops measured with a 500 Oe/s sweep rate at variable temperatures for **1** – **4**. (right) Derivative plots for the hysteresis data on **1** – **4**. These low temperature magnetic hysteresis loop measurements were performed by Dr. Wolfgang Kröner and Prof. Dr. Paul Müller at Department of Physics at Universät Erlangen-Nürnberg, Germany.

Dynamic magnetic properties

To investigate the magnetisation dynamics, the temperature dependent AC susceptibility data were collected for **1** – **4** at zero static field. Out-of-phase χ_M'' components are non-vanishing only when the system relaxation rate is comparable to the frequency. In Dy(III)-based SMMs a fast tunnelling mechanism can be active in zero static magnetic field[127], and a characterisation of dynamic susceptibility verse magnetic field (H) becomes necessary and important.

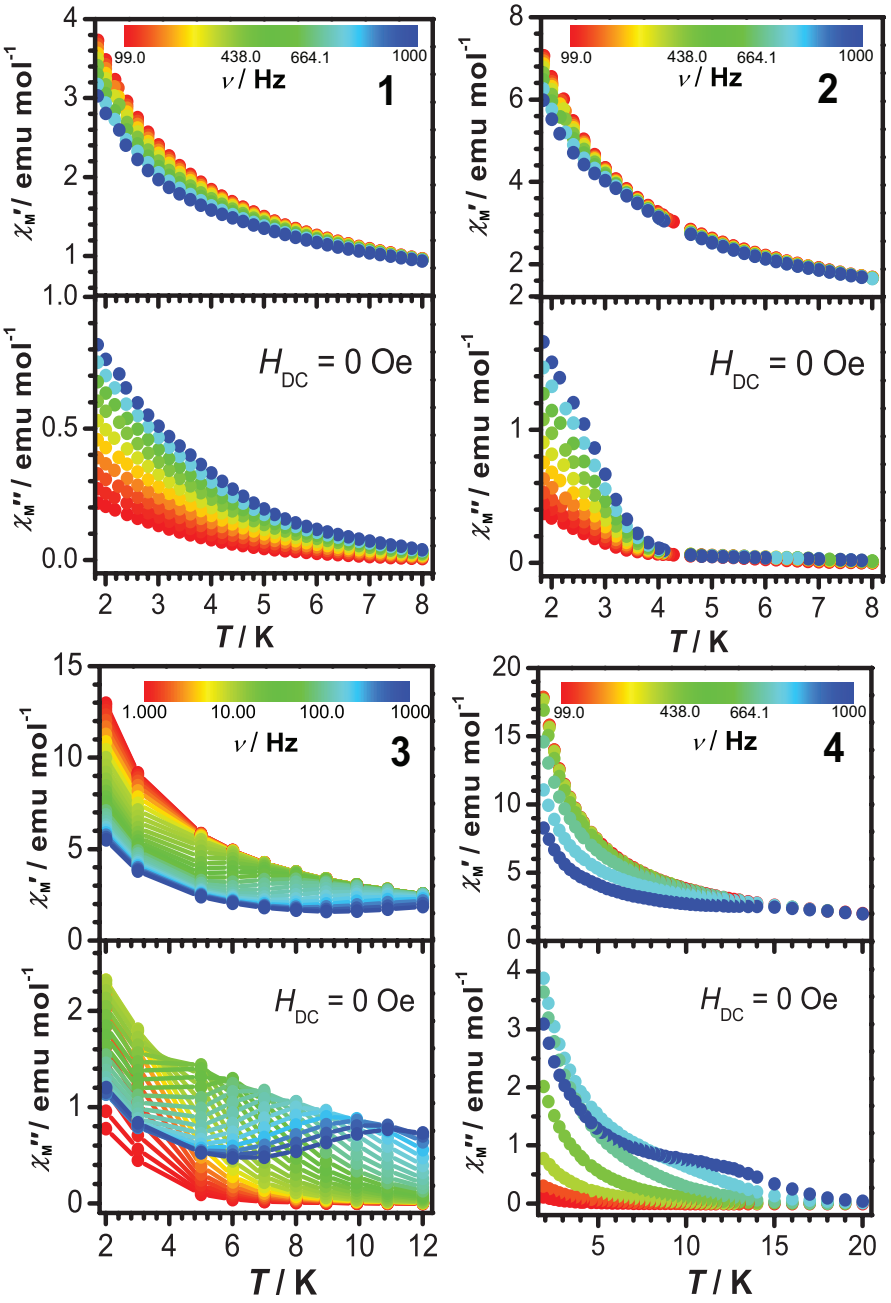

Figure 2.9: Temperature-dependent in-phase χ_M' and out-of-phase χ_M'' components of AC susceptibilities for **1** – **4** at different frequencies. The dynamic properties of compounds **1**, **2** and **4** were performed by Dipl. Chem. Alexa Paretzki and Dr. Lapo Bogani at the 1st Physics Institute of the University of Stuttgart, Germany.

Temperature-dependent AC susceptibility measurements in zero static field on **1** – **4** show frequency-dependent out-of-phase χ_M'' signals in the investigated temperature range (Figure 2.9). Nevertheless, distinct peaks of AC susceptibility was only observed for **3**, indicating the presence of faster magnetic relaxation in another three complexes. The absence of χ_M'' peaks for **1** was alos reported in Ref. [119], and the peaks can be found only at frequencies higher than 1000 Hz. At lower temperature (below ca. 5 K) a steady increase of χ_M' and χ_M'' signals can be seen for all compounds, indicating that there is a crossover from a thermal activation to a temperature-independent regime in the relaxation rates[127–129], the behaviour of which is often seen in Dy(III)-based SMMs.

The indicative parameter of spin-disorder F can be extracted from the data of the temperature-dependent χ_M'' signals (see Figure 2.9) using the Mydosh's formula $F = (\Delta T_P/T_P)/\Delta(\log(\nu))$, where ΔT_P is the difference between the highest and lowest blocking temperatures corresponding to the extremes of the investigated frequency ν that appears. This gives $F = 0.24$ for **3**, in the normal range $0.1 < F < 0.3$[75] for superparamagnetic materials, which suggest the magnetic behaviour of all compounds could not originate from spin glass behaviour.

Thus, we focus on the case of **3** under zero field. Further evidence of slow magnetic relaxation for **3** was obtained by analysing the frequency-dependence of AC susceptibility (Figure 2.10).

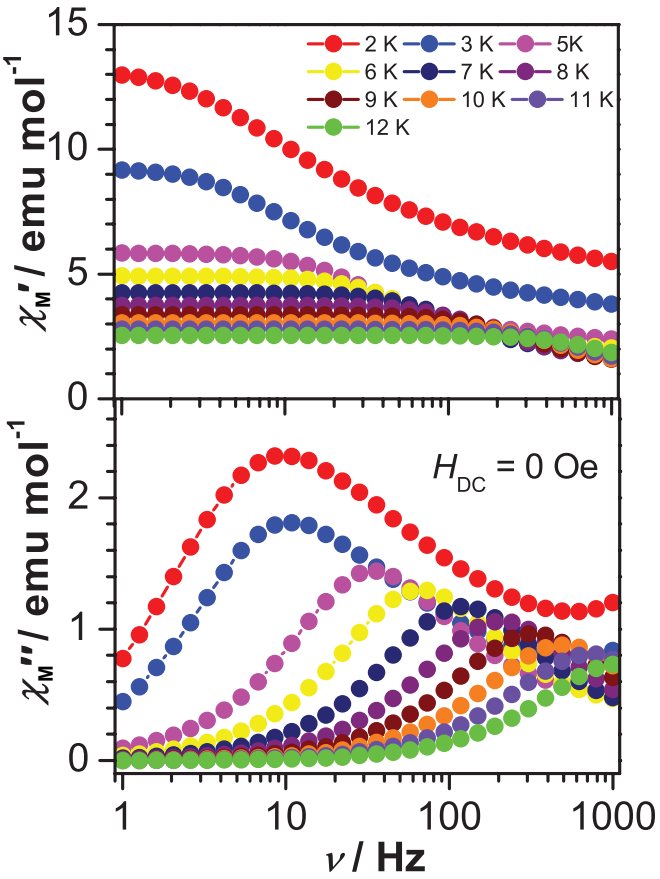

Figure 2.10: Frequency-dependence of the molar in-phase χ_M' and out-of-phase χ_M'' components of AC susceptibility for **3** under zero static field at different temperatures between 2 and 12 K.

The correlation between the peaks at higher temperatures (> ca. 5 K) and their corresponding frequencies can produce a linear plot of lnτ as a function of T^{-1}, Figure 2.11. The line is given in Figure 2.11a, in good agreement with the Arrhenius law, $\tau = \tau_0 \exp(U_{\text{eff}}/k_B T)$, where T is the temperature of the maximum χ_M'' at different frequencies and $\tau = 1/(2\pi\nu)$ (ν is the corresponding frequency). The best fitting ($R^2 > 0.98$) results give the attempt rate $\tau_0 = 7.58 \times 10^{-6}$ above 6 K, which is consistent with the expected τ_0 of 10^{-6} – 10^{-11} for SMMs[130]. The effective energy barrier U_{eff}/k_B is 37 ± 2 K. The Cole-Cole diagram was obtained from 1 to 1000 Hz in zero static field in the term of χ_M' and χ_M'' between 2 and 12 K, Figure 2.11b. We can have direct access to the width of the distribution of the relaxation rate by fit to the generalised Debye model (see **Chapter 1**). A distribution coefficient α values are obtained with the fit to the diagram. **3** possess α value in the range between 0.04 and 0.23, indicating a narrow distribution of relaxation process.

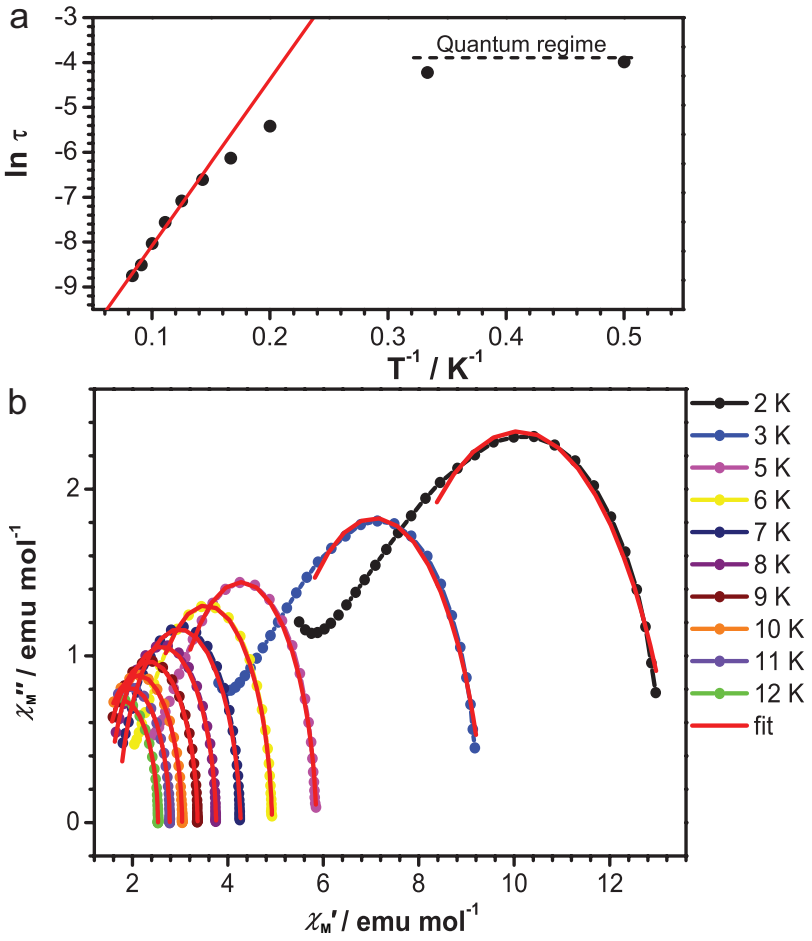

Figure 2.11: a. Plots of lnτ versus T^{-1} for **3** in $H_{DC} = 0$ Oe, and the fitting to Arrhenius law (solid line, red); b. Argand diagram for **3** in $H_{DC} = 0$ Oe between 2 and 12 K.

A tunnelling relaxation channel is present in all compounds, as indicated by the up-turns of χ_M'' signals at lower-T and $H = 0$ Oe (Figure 2.9), which can be suppressed in nonzero magnetic field ($H \neq 0$ Oe). A different relaxation mechanism becomes dominant in H

≠ 0 Oe, leading to the presence of an almost field-independent out-of-phase peaks that appears at different temperatures for the different systems. Thus, the AC measurements were performed at 10 K with various applied static fields in the frequency range 1 – 1000 Hz on compound **3**. The results are shown in Figure 2.12. No frequency-dependent peaks are observed for the out-of-phase χ_M'' signals under different external fields. Therefore, a moderate external field of 4 kOe was selected to measure the AC susceptibilities for all complexes **1** – **4**.

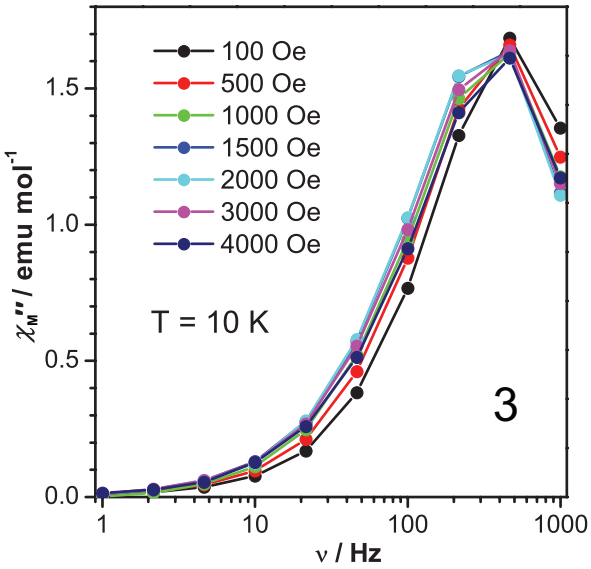

Figure 2.12: Frequency-dependence of the molar out-of-phase χ_M'' components of AC susceptibility for **3** at 10 K under different static fields.

Temperature-dependent χ_M' and χ_M'' components of AC susceptibility in the static field of 4 kOe, at which the tunnelling mechanism is suppressed, have been measured on **1** – **4** (Figure 2.13). Both χ_M' and χ_M'' signals for **1** – **4** are frequency dependent, and χ_M'' peaks appear in the investigated temperature regions. Specifically, for mononuclear compounds **1** and **2**, frequency dependence of the AC signals appear below ca. 5 K. For dimer compound **3** and trinuclear compound **4**, frequency dependence of AC signals appear below ca. 12 K. Such behaviour indicates the presence of slow relaxation of magnetisation. This relaxation follows the thermally activated mechanism and the energy barrier for **1** – **4** will be given by data fitting using the Arrhenius law (see below).

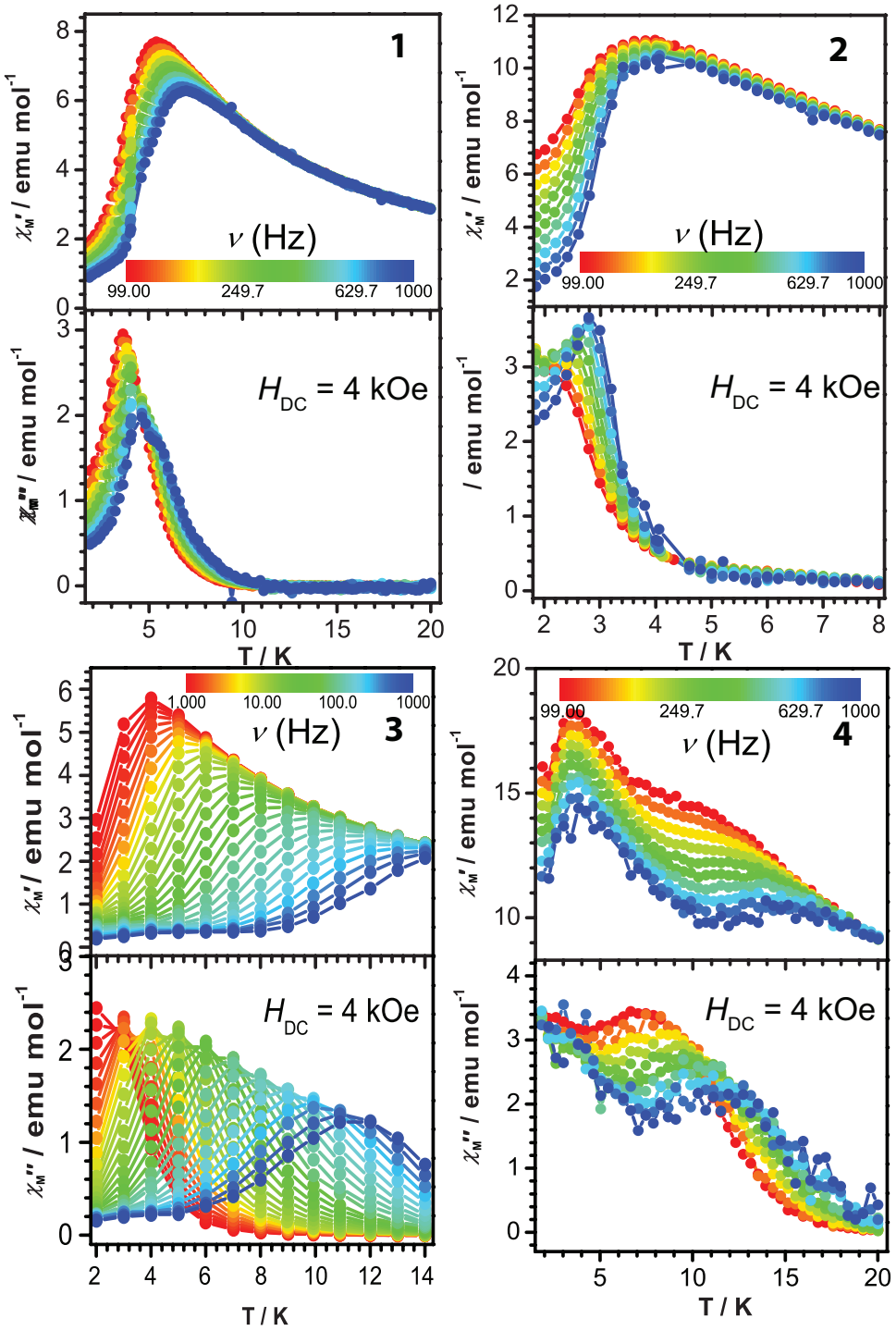

Figure 2.13: Temperature-dependent molar in-phase χ_M' and out-of-phase χ_M'' components of AC magnetic susceptibility, as measured in H_{DC} = 4 kOe for complexes **1** – **4**. The dynamic properties of compounds **1**, **2** and **4** were performed by Dipl. Chem. Alexa Paretzki and Dr. Lapo Bogani at the 1st Physics Institute of the University of Stuttgart, Germany.

Variable frequency-dependent AC susceptibilities were also measured for complexes **1** – **4** under the static field of 4 kOe at various temperatures, as shown in Figure 2.14. The decline in the χ_M' signal concomitant with the appearance of the peaks in the χ_M'' component again indicate slow relaxation of magnetisation.

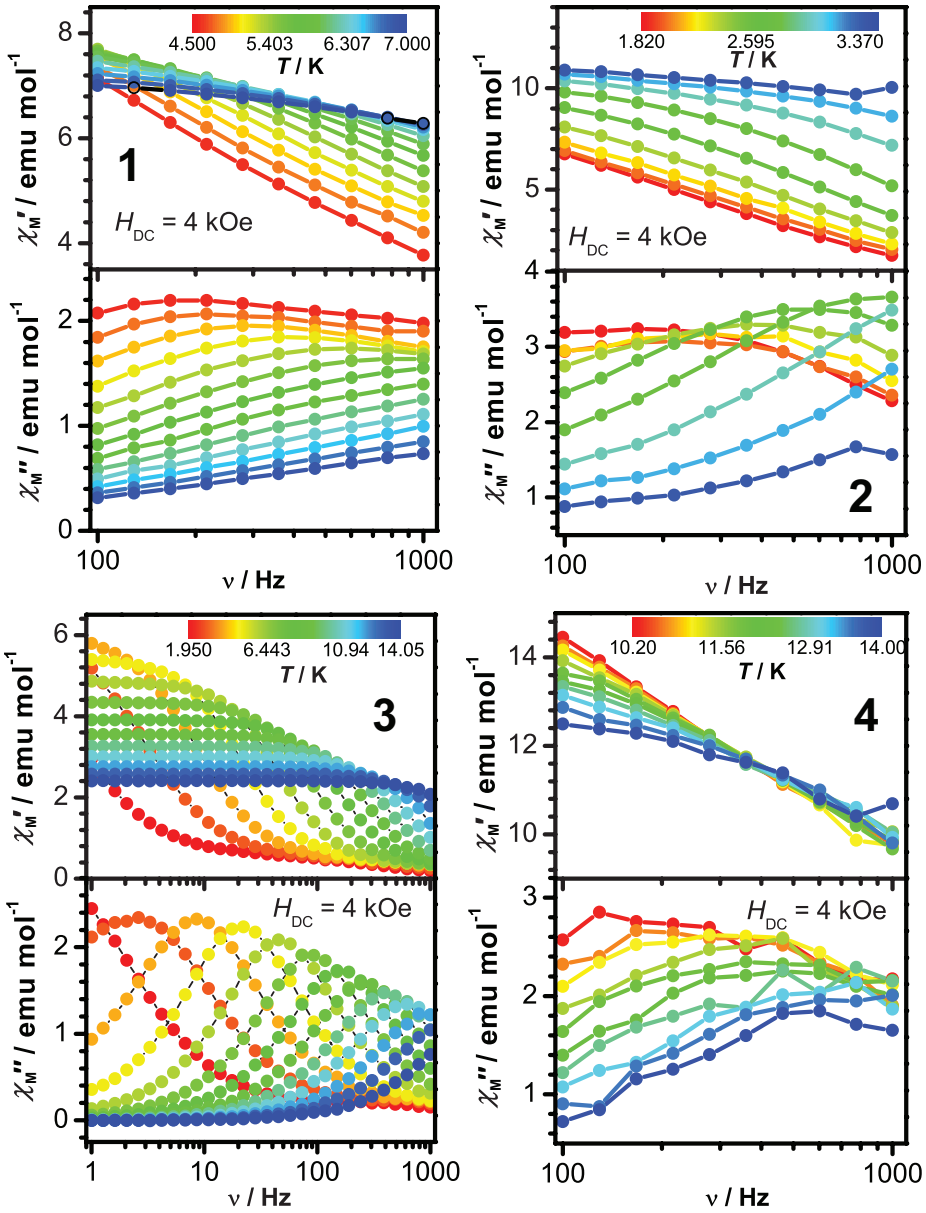

Figure 2.14: Frequency-dependence of the molar in-phase χ_M' and out-of-phase χ_M'' components of AC susceptibilities for **1** – **4** under $H_{DC} = 4$ kOe at different temperatures. The dynamic properties of compounds **1**, **2** and **4** were performed by Dipl. Chem. Alexa Paretzki and Dr. Lapo Bogani at the 1st Physics Institute of the University of Stuttgart, Germany.

It is observed that, the temperature of the χ_M'' maximum changes depending on frequency of magnetic field, indicating the presence of a dynamical blocking of the magnetisation via a thermally activated process.

Relaxation time τ extracted from AC susceptibility as a function of oscillating frequency of fields (Figure 2.14) can also characterise this mechanism. Linear regression on the Arrhenius plots (Figure 2.15) affords good agreement (R^2 >0.97) for all compounds, giving the values of the effective energy barrier $U_{eff}/k_B = 41 \pm 2$ K and $\tau_0 = 1.3 \times 10^{-8}$ for **1**, $U_{eff}/k_B = 8 \pm 1$ K and $\tau_0 = 1.7 \times 10^{-5}$ for **2**, $U_{eff}/k_B = 41 \pm 1$ K and $\tau_0 = 6.8 \times 10^{-6}$ for **3**, and $U_{eff}/k_B = 84 \pm 5$ K and 3.4×10^{-7} for **4**. To elucidate the details of the relaxation

dynamics for the four complexes, Argand plots constructed from Figure 2.14 are shown in Figure 2.16. By fit to the generalised Debye model, the distribution coefficient α values for obtained with being 0.25 – 0.57 (2.6 – 9.0 K) for **1**, 0.33 – 0.70 (1.8 – 3.6 K) for **2**, 0.01 – 0.20 (2 – 14 K) for **3** and 0.10 – 0.26 (11.0 – 16.8 K) for **4**. All compounds show the narrow distribution of relaxation time, which is comparable to those found in Dy(III)-based SMMs.

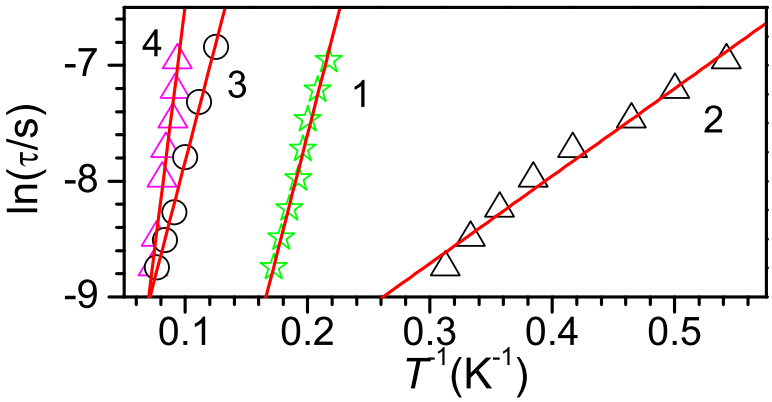

Figure 2.15: Arrhenius laws extracted for **1** – **4**, from the frequency-dependent χ_M'' signals in H_{DC} = 4 kOe.

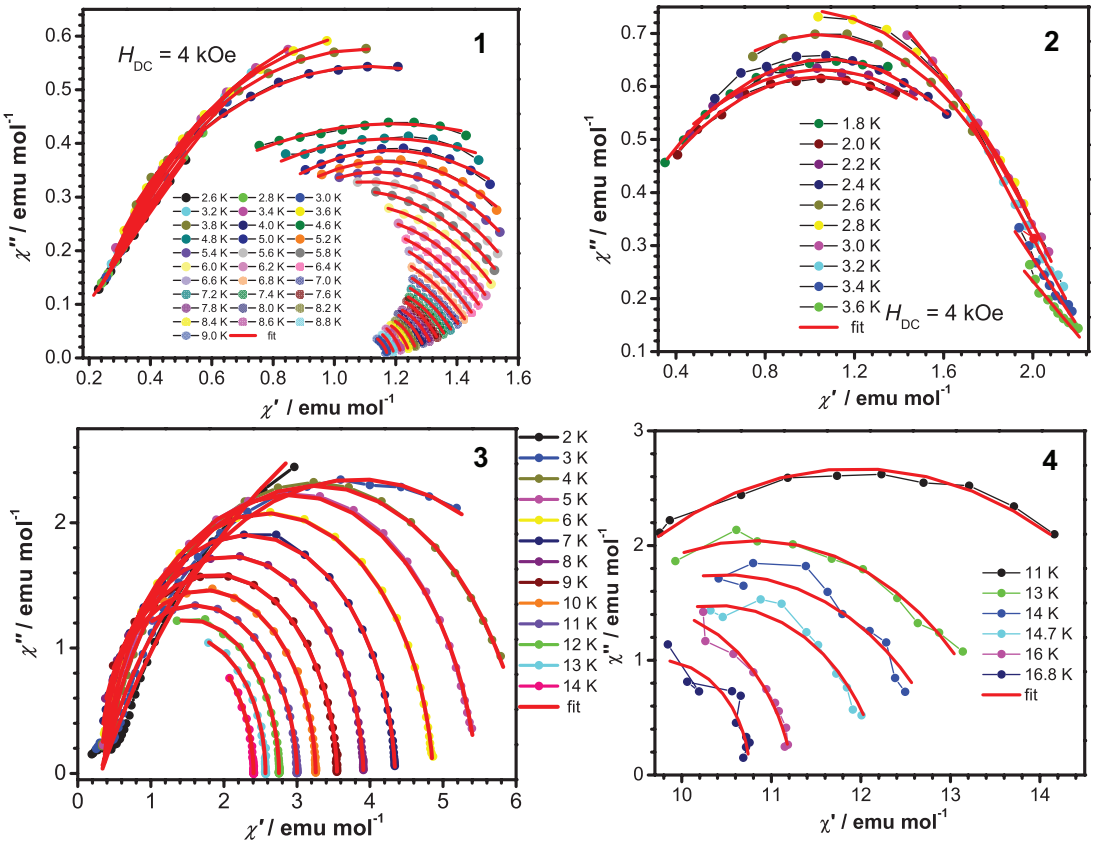

Figure 2.16: Argands plots for **1** – **4** obtained using the frequency-dependent AC susceptibility data in H_{DC} = 4 kOe.

Clearly, slow magnetic relaxation characteristic of SMMs behaviour can be observed for **3** and **4** below ca. 12 K, while for mononuclear **1** and **2** below ca. 5 K. Such a difference can be due to the different local environments about dysprosium(III) ion in **1** – **4**. As described above, the coordination geometry is a distorted square anti-prism in **1**, **2** and **3**, while there is a distorted mono-capped square anti-prism in **3**.

3 Solvent substituent on Dy(III)-SMMs behaviour

The single crystal X-ray diffraction measurements were performed by Dr. Wolfgang Frey from Organic Chemistry Institute at the University of Stuttgart. The crystal structures were resolved by Dr. Shang -Da Jiang at the 1st Physics Institute at the University of Stuttgart and Dr. Wolfgang Frey from the Organic Chemistry department of the University of Stuttgart. The element analysis of all compounds were measured by Ms. Barbara Förtsch from Inorganic Chemistry department of the University of Stuttgart. The effective-point-charge simulations were done by Dr. Shang -Da Jiang from the School of Chemistry at the Peking University, P.R. China.

3.1 Introduction

As introduced in **Chapter 2**, amounts of mono- and polynuclear lanthanide containing complexes have been reported in the past two decade, thanks to the flexibility of the coordination and supramolecular chemistry. From the viewpoint of interaction between structure and superparamagnetic property, the ligand field strongly influence the local anisotropy of the lanthanide ions and thus govern the magnetic behaviour of the investigating systems.

$Ln(hfac)_3X$ (X= hfac[131], monoglyme[132], DPEPO[133], etc.) complexes are well known in the literature for their interesting magnetic and photophysical properties. Herein, we investigated how the inclusion of different coordinating solvents influences the magnetic properties of a centrosymmetric Dy(III) dimer. The synthesis, solid state structures and magnetic properties of a series of neutral dysprosium(III)-based dimers, sharing the general formula $[Dy(hfac)_3R]_2$bpm (hfac = hexafluoroacetylacetonate; bpm = 2,2′ -bipyrimidine), in which R = nothing (**5**), water (H_2O, **6**), ethyl acetate (EA, **3**), and methyl propionate (MP, **7**) are included.

3.2 Experimental Section

3.2.1 Chemical reactants

All reactants were purchased from Sigma-Aldrich and used without further purification. The starting compound $Dy(hfac)_3{\cdot}2H_2O$ was synthesised as described in **Chapter 2**.

3.2.2 Synthesis Paths

$Dy(hfac)_3{\cdot}2H_2O$ was reacted with bpm in acetonitrile to afford $[Dy(hfac)_3]_2bpm$ (**5**).

$[Dy(hfac)_3]_2bpm$ (**5**) was synthesised by adding dropwise a 5 ml solution of acetonitrile and 2,2′-bipyrimidine (0.5 mmol, 79.1 mg) to a hot solution (ca. 60 °) of 20 ml acetonitrile and $Dy(hfac)_3(H_2O)_2$ (1.0 mmol, 819.7 mg) under vigorous stirring. After refluxing 2 hours, the reaction was cooled naturally down to room temperature. Volatile organic solvents were removed under reduced pressure and the yellowish residue precipitate was recrystallised from acetonitrile/n-heptane to give single crystals of compound **5** in a few days. Elemental analysis calc. for **5** ($C_{38}H_{12}Dy_2F_{36}N_4O_{12}$): C 26.39; H 0.71; N 3.24. Found: C 26.50; H 1.01; N 3.32.

Following the same procedure, the recrystallisation of **5** in R/heptane ($R = H_2O$, ethyl acetate, and methyl propionate) affords complexes **6**, **3**, and **7**. The schematic diagrams of compounds **5**, **6**, **7** are shown in Figure 3.1. The synthetic details for all compounds are provided as below.

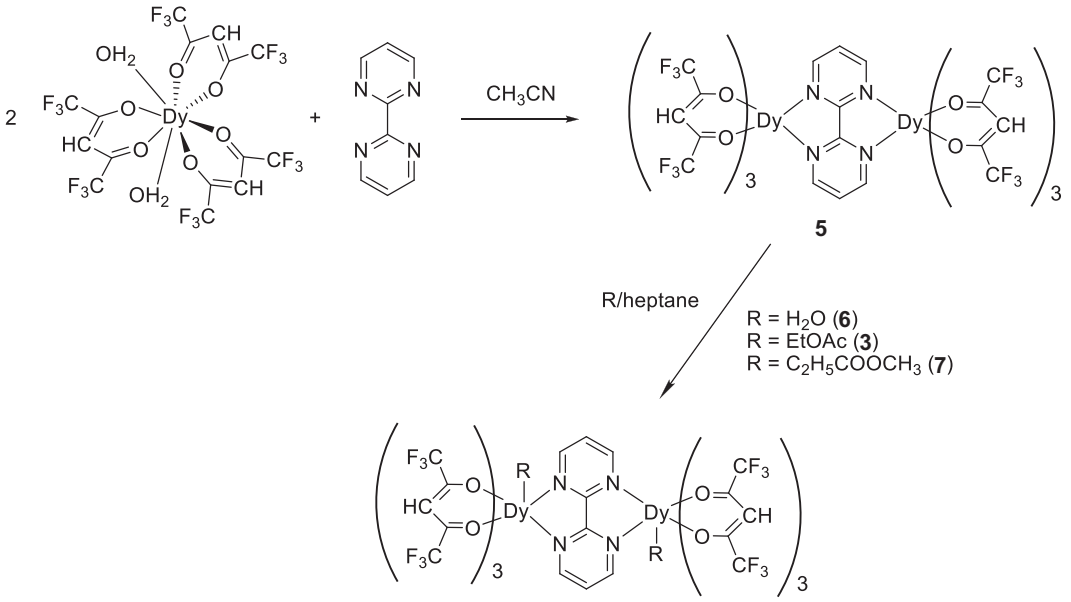

Figure 3.1: Synthesis scheme of $[Dy(hfac)_3R]_2bpm$ where R represents selected solvents in this chapter, where R = nothing (**5**), H_2O (**6**), EtOAc (**3**), and $C_2H_5COOCH_3$ (**7**).

$[Dy(hfac)_3(H_2O)]_2bpm$ (**6**) was obtained by dissolving **5** (0.1 mmol, 172.5 mg) in 10 ml of water. After cooling 20 ml n-heptane was added and the solution was stored at 4 °C. Overnight single crystals were obtained in good crystallographic quality. Elemental analysis calc. for **6** ($C_{38}H_{16}Dy_2F_{36}N_4O_{14}$): C 25.85; H 0.91; N 3.18. Found: C 26.00; H 0.99; 3.28.

$[Dy(hfac)_3(C_2H_5COOCH_3)]_2bpm$ (**7**) was obtained, by dissolving compound **5** (0.1 mmol, 172.5 mg) in 10 ml of the corresponding solvent. After 20 ml n-heptane was added and the solutions were stored at 4 °C. Single crystals of **7** was obtained in good crystallographic quality in a few days. Elemental analysis calc. for **7**: $C_{46}H_{28}Dy_2F_{36}N_4O_{16}$: C 28.99; H 1.48; N 2.94; Found: C 29.24; H 1.63; N 3.12.

Elemental analyses were carried out with a Perkin–Elmer Analyzer 240. X-ray diffraction data were collected using a Bruker Kappa APEX II duo single crystal X-ray diffractometer at 110(2) K (Mo Kα radiation, $\lambda = 0.71073$ Å). The structures were solved and refined by full-matrix leasts-quares techniques on F_2 using SHELX-97[118]. Absorption correction was done numerically or by the multi-scan technique. All data were corrected for Lorentz and polarisation effects, and the non-hydrogen atoms were refined anisotropically. Hydrogen atoms were included in the refinement process using the riding model. All single crystal measurements and molecular structures have been done by Dr. Wolfgang Frey. CCDC reference numbers for compounds **5**, **6**, **3**, and **7** are 1410460, 1410459, 1410458, and 1410460 respectively. These data can be obtained free of charge from the Cambridge Crystallographic Data Centre (CCDC).

Magnetic susceptibility measurements in external field (both DC and AC) were performed on powder samples with a Quantum Design MPMS-XL 7 SQUID system and corrected for the diamagnetism of the sample and the diamagnetic contribution of the sample holder, as independently determined. All samples were immobilised into grease to prevent field orientation of the microcrystalline powders.

3.3 Results and Discussion

3.3.1 Structure Characterisation

Selected crystallographic parameters for compounds **5** – **7** are summarised in Table 3.1, and 3.2, respectively. The bond lengths and bond angles for **3** can be found in **Chapter 2** and are not shown here.

Characterisation via single-crystal X-ray diffraction analysis shows that all complexes crystallise in different space groups. Complexes **5** and **6** crystalline in the triclinic space group $P\bar{1}$, **3** in the monoclinic space group C2/c, and **7** in the monoclinic space group $P2_1/c$. The four complexes differ in the substituents on the solvent molecules, which leads to different coordination environments around Dy(III) ions. The Dy(III) ions in the dimer molecules are related by inversion symmetry from the planar bpm moiety, and therefore possess the same single-ion electronic structure. Key crystallography features of complexes **5** – **7**, including Dy–O and Dy–N bond distances, are summarised for easy comparison in Table 3.3. The detailed structural information for each compound will be described as below.

Table 3.1: Crystallographic data and refinement parameters for **5** and **6**

Complex	**5**	**6**
M_w	1724.46	1761.55
temperature (K)	110(2)	110(2)
λ(Å)	0.71073	0.71073
crystal size (mm)	0.46 × 0.30 × 0.25	0.41 × 0.37 × 0.14
colour	colourless	colourless
crystal habit	blocks	blocks
crystal system	triclinic	triclinic
space group	$P\bar{1}$	$P\bar{1}$
a, b, c (Å)	11.0346(1)	12.1431(8)
	16.4936(1)	15.6332(1)
	31.321(3)	15.6893(1)
α (°)	101.858(4)	76.729(4)
β (°)	92.027(4)	78.777(4)
γ (°)	104.213(4)	71.410(3)
V (Å^3)	5385.84(9)	2723.69(3)
Z	4	2
F(000)	3214	1680
D (g cm^{-3})	2.10144	2.14779
μ (mm^{-1})	2.936	3.072
θ range (°)	1.65 - 36.43	1.76 - 30.55
index ranges *h,k,l*	-18 ≤ h ≤ 18	-17 ≤ h ≤ 17
	-27 ≤ k ≤27	-22 ≤ k ≤22
	-52 ≤ l ≤ 52	-22 ≤ l ≤ 22
reflns. collected	272962	57868
indep. reflns.	52268	16669
restraints/parameters	94/1667	57/857
R[a]	0.0336	0.0223
wR[b]	0.0741	0.0487
GOF (for F_2)	1.020	1.036
Rint	0.0438	0.0314
$\Delta\rho_{max}$.; $\Delta\rho_{min}$(e Å^{-3})	2.533; -1.980	1.373; -1.161

[a] $R = \Sigma||F_o|-|F_c||/\Sigma|F_o|$

[b] $R_w = [\Sigma w(F_o^2-F_c^2)^2/\Sigma w(F_o^2)^2]^{1/2}$

Table 3.2: Crystallographic data and refinement parameters for **7**

M_w	1901.72	T (K)	110(2)
λ (Å)	0.71073	crystal size (mm)	0.7 × 0.38 × 0.30
colour	colourless	crystal habit	blocks
crystal system	monoclinic	space group	P 2_1/c
a (Å)	11.8077(8)	b (Å)	17.2751(12)
c (Å)	16.1740(11)		
α (°)	90	β (°)	102.950(3)
γ (°)	90		
V (Å^3)	3215.2(4)	Z	2
F(000)	1832	D (g cm^{-3})	1.964
μ (mm^{-1})	2.476	θ range (°)	2.58 – 30.74
index ranges h	-16 ≤ h ≤ 16	k	-24 ≤ k ≤ 22
l	-17 ≤ l ≤ 23		
reflns. collected	37554	indep. reflns.	9970
restraints/parameters	123/496	R[a]	0.0383
wR[b]	0.0.0888	GOF (for F_2)	1.038
Rint	0.0501	$\Delta\rho_{max}$.; $\Delta\rho_{min}$(e Å^{-3})	2.231; -1.784

[a] $R = \Sigma||F_o|-|F_c||/\Sigma|F_o|$
[b] $R_w = [\Sigma w(F_o^2-F_c^2)^2/\Sigma w(F_o^2)^2]^{1/2}$

Table 3.3: Selected bond distances (Å) and dihedral angles (°) for **5** - **7**

	5	**6**	**7**
Dy1-O1	2.334(2)	2.327(2)	2.343(3)
Dy1-O2	2.293(2)	2.358(2)	2.339(3)
Dy1-O3	2.327(2)	2.327(2)	2.351(3)
Dy1-O4	2.297(2)	2.362(1)	2.344(3)
Dy1-O5	2.320(2)	2.515(2)	2.346(3)
Dy1-O6	2.329(2)	2.332(2)	2.418(3)
Dy1-O7			2.351(3)
Dy1-N1	2.553(2)	2.585(2)	2.589(2)
Dy1-N2	2.577(2)	2.596(2)	2.599(2)
Dihedral angles(°) for **5**			
θ_1	O2 [O1 N1] N2[a]	13.89	
θ_2	O4 [O3 O5] O6	0.99	
Dihedral angles (°) for **6**			
θ_1	O1 [O2 N2] N1	7.56	
θ_2	O4 [O3 O6] O1W	1.04	
Dihedral angles (°) for **7**			
θ_1	O2 [O1 N1] N2	13.89	
θ_2	O4 [O3 O5] O6	0.99	

[a] A [B C] D is dihedral angle between ABC plane and BCD plane;

Figure 3.2a illustrates the molecular structure of **5**. Selected bond distances and angles for it are listed in Table 3.4. The coordination sphere of each dysprosium atom is comprised of six oxygen atoms from three hfac ligands and two nitrogen atoms from the bridging bpm ligand, forming an 8-coordinate distorted square anti-prismatic geometry (Figure 3.2b). The approximate square planes are defined as O1-O2-N2-N1 and O3-O4-O6-O5, respectively. Both planes are almost parallel, with dihedral angle of 1.69°. The shortest intra- and intermolecular distances between two Dy(III) ions are 6.712(9) and 7.460(7) Å, respectively. The Dy-O(hfac) lengths are found in the range of 2.293(2)–2.334(2) Å (av. 2.307 Å), comparable to those containing Dy(hfac)$_3$ motif in the literatures[119, 121, 132]. Structural study also reveals the Dy-N1 and Dy-N2 bond lengths are 2.553(2) and 2.577(2) Å (Table 3.4).

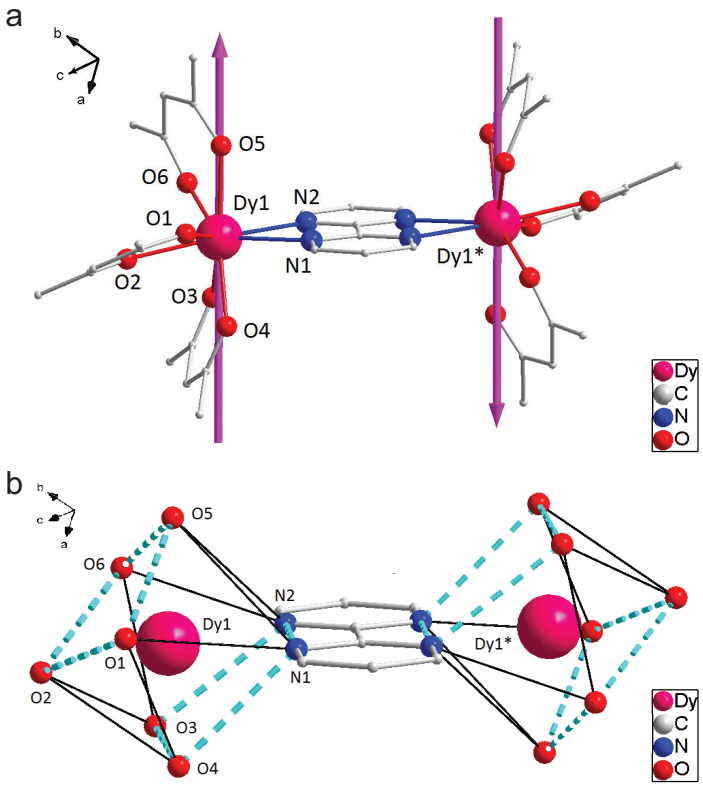

Figure 3.2: a. Molecular structure of **5**. Hydrogen atom are omitted for clarify. b. Distorted square antiprismatic geometry around Dy(III) in compound **5**: the approximate square plans defined as O1-O2-N2-N1 and O3-O4-O6-O5 (turquoise dashed lines), and the dihedral angle and distance between the centroids of two planes are 1.69° and 2.525 Å, respectively. Symmetry-equivalent positions are denoted by a star ∗ in the label. Symmetry code: -x+1, -y+1, -z+1. This crystal structure of **1** were resolved by Dr. Shang -Da Jiang at the 1st Physics Institute of the University of Stuttgart and Dr. Wolfgang Frey from the Organic Chemistry department of the University of Stuttgart.

Table 3.4: Selected Bond Angles (°) for Compound **5**

O2-Dy1-O4	79.4(6)	O2-Dy1-O5	149.8(6)
O4-Dy1-O5	125.0(6)	O2-Dy1-O3	84.5(7)
O4-Dy1-O3	74.3(6)	O5-Dy1-O3	85.8(6)
O2-Dy1-O6	135.7(6)	O4-Dy1-O6	78.1(6)
O5-Dy1-O6	72.1(6)	O3-Dy1-O6	124.4(6)
O2-Dy1-O1	72.6(6)	O4-Dy1-O1	139.7(6)
O5-Dy1-O1	77.3(6)	O3-Dy1-O1	74.7(6)
O6-Dy1-O1	141.6(6)	O2-Dy1-N1	95.5(7)
O4-Dy1-N1	140.8(6)	O5-Dy1-N1	76.4(6)
O3-Dy1-N1	144.4(6)	O6-Dy1-N1	79.2(6)
O1-Dy1-N1	71.5(6)	O2-Dy1-N2	70.4(6)
O4-Dy1-N2	78.6(6)	O5-Dy1-N2	127.1(6)
O3-Dy1-N2	146.0(6)	O6-Dy1-N2	68.1(6)
O1-Dy1-N2	116.7(6)	N1-Dy1-N2	63.3(6)

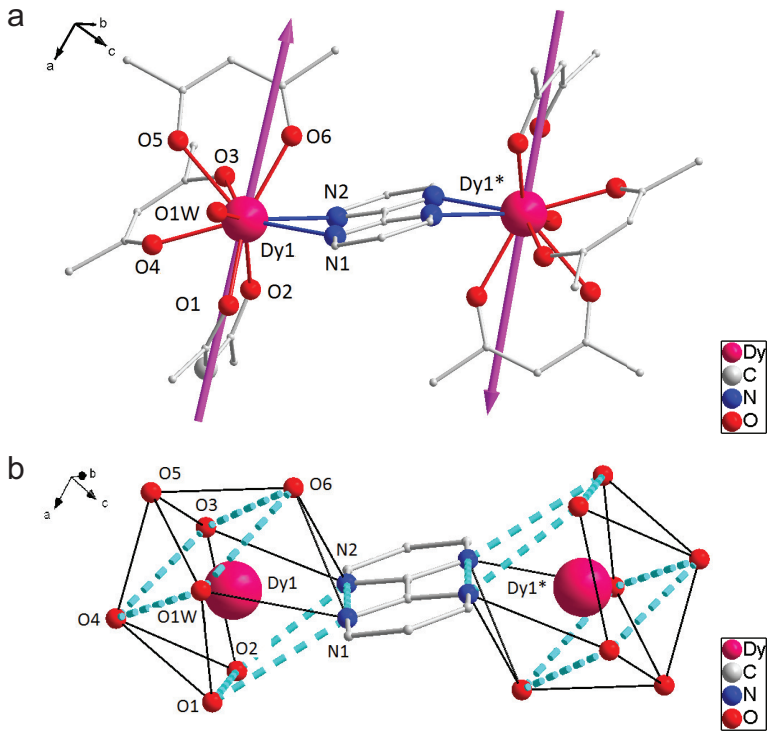

Figure 3.3: a) Molecular structure of **6**. Hydrogen atom are omitted for clarify. b) Distorted square antiprismatic geometry around Dy(III) in compound **6**: the approximate square plans defined as O1-O2-N2-N1 and O4-O3-O6-O1W. Symmetry-equivalent positions are denoted by a star $*$ in the label. Symmetry code: -x+1, -y+1, -z. This crystal structure of **6** were resolved by Dr. Shang -Da Jiang at the 1st Physics Institute of the University of Stuttgart and Dr. Wolfgang Frey from the Organic Chemistry department of the University of Stuttgart

Table 3.5: Selected Bond Angles (°) for Compound **6**

O3-Dy1-O6	80.2(5)	O2-Dy1-O5	133.0(5)
O3-Dy1-O1	137.8(5)	O4-Dy1-O5	67.8(5)
O6-Dy1-O1	141.8(5)	O1W-Dy1-O5	67.9(5)
O3-Dy1-O2	74.1(5)	O3-Dy(1)-N1	133.7(5)
O6-Dy1-O2	132.9(5)	O6-Dy(1)-N1	69.8(5)
O1-Dy1-O4	71.4(5)	O1-Dy(1)-N1	77.2(5)
O3-Dy1-O4	75.0(5)	O2-Dy1-N1	101.2(5)
O6-Dy1-O4	135.2(5)	O4-Dy1-N1	149.6(5)
O1-Dy1-O4	72.9(5)	O1W-Dy1-N1	75.8(5)
O2-Dy1-O1W	74.3(5)	O5-Dy1-N1	125.5(5)
O3-Dy1-O1W	138.0(5)	O3-Dy1-N2	74.1(5)
O6-Dy1-O1W	87.0(5)	O6-Dy1-N2	68.5(5)
O1-Dy1-O1W	66.4(5)	O1-Dy1-N2	112.4(5)
O2-Dy1-O1W	137.3(5)	O2-Dy1-N2	66.7(5)
O4-Dy1-O5	87.3(5)	O4-Dy1-N2	135.3(5)
O3-Dy1-O5	70.2(5)	O1W-Dy1-N2	136.7(5)
O6-Dy1-O5	69.0(5)	O5-Dy1-N2	127.8(5)
O1-Dy1-O5	119.7(5)	N1-Dy1-N2	62.6(5)

By coordinating one water molecule to each Dy(III) ion in **6** (Figure 3.3a), a nine-coordinated geometry of each Dy(III) ion is obtained with six positions occupied by oxygen atoms from the three hfac ligands with the Dy-O(hfac) lengths in the range of 2.327(2) – 2.362(1) Å (av. 2.322(1) Å), two positions by nitrogen atoms from the bridging bpm ligand with the Dy1-N1 and Dy1-N2 bond lengths of 2.585(2) and 2.596(2) Å, and one position by oxygen from water of 2.398 Å (Dy-O1W), respectively. The coordination geometry of each Dy(III) centre in **6** can be described as a distorted mono-capped square anti-prism where the two square planes are defined as the O1, O2, N2, N1 and O1, O4, O3, O6 atoms, and O5 is on the capping position (Figure 3.3 b).

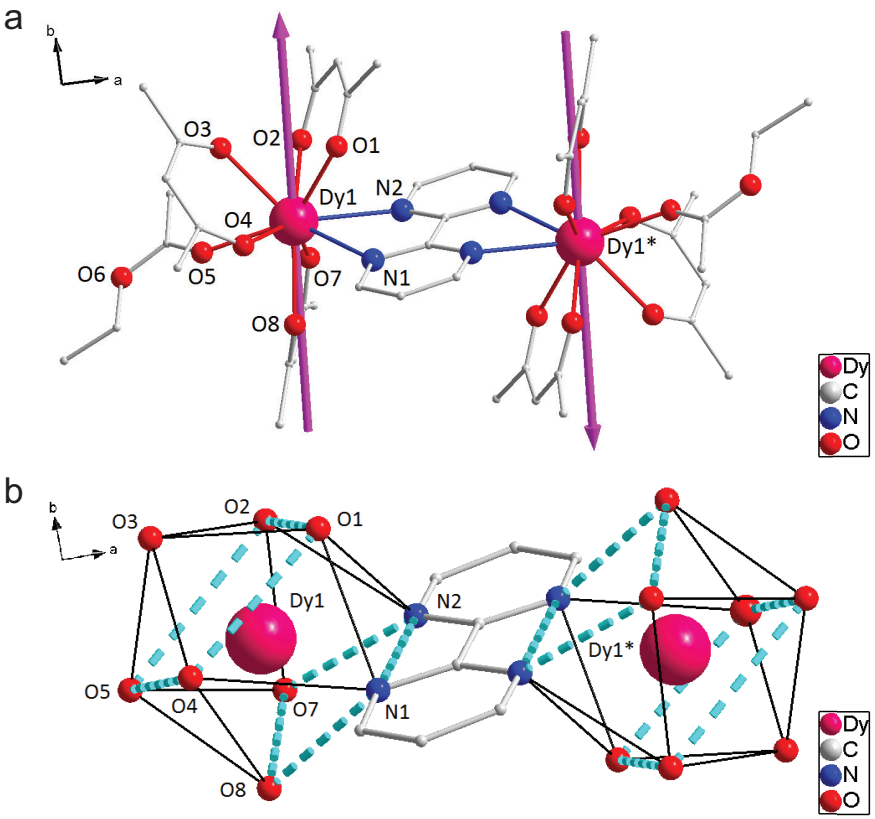

Figure 3.4: a) Molecular structure of **3**. Hydrogen atom are omitted for clarify. b) Distorted square-anti-prismatic geometry around Dy(III) ions in compound **3**: the approximate square plans defined as O1-O2-O5-O4 and O7-O8-N1-N2. Symmetry-equivalent positions are denoted by a star $*$ in the label. Symmetry code: -x+0.5, -y+1.5, -z+1. This crystal structure of **3** were resolved by Dr. Shang -Da Jiang at the 1st Physics Institute of the University of Stuttgart and Dr. Wolfgang Frey from the Organic Chemistry department of the University of Stuttgart.

The molecular structure and atomic numbering of **3** are shown in Figure 3.4 and detailed analysed in **Chapter 2**.

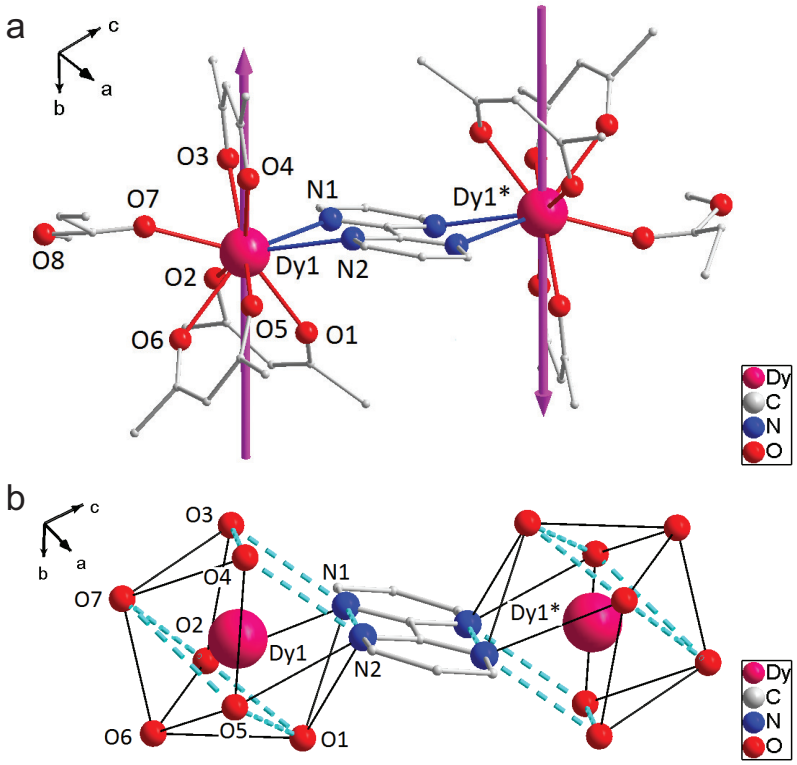

Figure 3.5: a. Molecular structure of **7**. Hydrogen and Fluorine atoms have been omitted for clarify. b. the two square planes defined as the O1, O2, O7, O5 and O3, O4, N2, N1 atoms, and O6 is on the capping position. Symmetry-equivalent positions are denoted by a star $*$ in the label. Symmetry code: -x, -y+1, -z+1. This crystal structure of **7** were resolved by Dr. Shang -Da Jiang at the 1st Physics Institute of the University of Stuttgart and Dr. Wolfgang Frey from the Organic Chemistry department of the University of Stuttgart.

Table 3.6: Selected and Bond Angles (°) for Compound **7**

O2-Dy1-O1	74.4(9)	O5-Dy1-O6	69.6(9)
O2-Dy1-O4	147.8(1)	O7-Dy1-O6	68.5(1)
O1-Dy1-O4	134.8(9)	O3-Dy1-O6	127.3(1)
O2-Dy1-O5	133.3(9)	O2-Dy1-N2	128.7(9)
O1-Dy1-O5	78.4(9)	O1-Dy1-N2	69.0(9)
O4-Dy1-O5	74.9(9)	O4-Dy1-N2	68.3(9)
O2-Dy1-O7	87.6(1)	O5-Dy1-N2	72.0(9)
O1-Dy1-O7	142.6(1)	O7-Dy1-N2	142.0(1)
O4-Dy1-O7	74.4(1)	O3-Dy1-N2	101.5(1)
O5-Dy1-O7	91.8(1)	O6-Dy1-N2	130.9(1)
O2-Dy1-O3	77.0(1)	O2-Dy1-N1	72.3(9)
O1-Dy1-O3	131.1(1)	O1-Dy1-N1	67.7(9)
O4-Dy1-O3	72.4(1)	O4-Dy1-N1	103.4(9)
O5-Dy1-O3	146.6(1)	O5-Dy1-N1	129.2(9)
O7-Dy1-O3	73.2(1)	O7-Dy1-N1	137.6(1)
O2-Dy1-O6	66.8(1)	O3-Dy1-N1	66.2(1)
O1-Dy1-O6	74.2(1)	O6-Dy1-N1	129.8(1)
O4-Dy1-O6	126.7(1)	N1-Dy1-N2	61.3(9)

Figure 3.5a shows the molecular structure of compound **7**. Each methyl propionate molecule was incorporated to coordinate each Dy(III) ion, making the coordination geometry of Dy(III) ion is a distorted octahedron. The distances between Dy atom and six surrounding oxygen atoms from the three hfac ligands were found to be in the range of 2.339(3) - 2.351(3) Å (av. 2.356(3) Å), and the lengths of Dy-N where nitrogen atoms are from the bridging bpm ligand are 2.633(3) Å for Dy1-N1 and 2.601(3) Å for Dy1-N2, respectively, the bond length between the oxygen atom from solvent molecule methyl propionate (MP) and Dy(III) ion is 2.351(3) Å, little larger than that of Dy-O(hfac), causing the distorted coordination environment of each Dy(III) ion.

3.3.2 Magnetic properties

Magnetic measurements including DC and AC magnetic response were performed on a commercial Quantum Design MPMS-XL 7 SQUID magnetometer. Samples prepared for SQUID measurements were polycrystalline samples embedded in grease to avoid in-field orientation of the crystallites. Measurements were corrected for the diamagnetic contribution, as calculated with the Pascal′s constants, and for the diamagnetism of the sample holder as independently determined at the same temperature and magnetic fields.

Static Magnetic Measurements

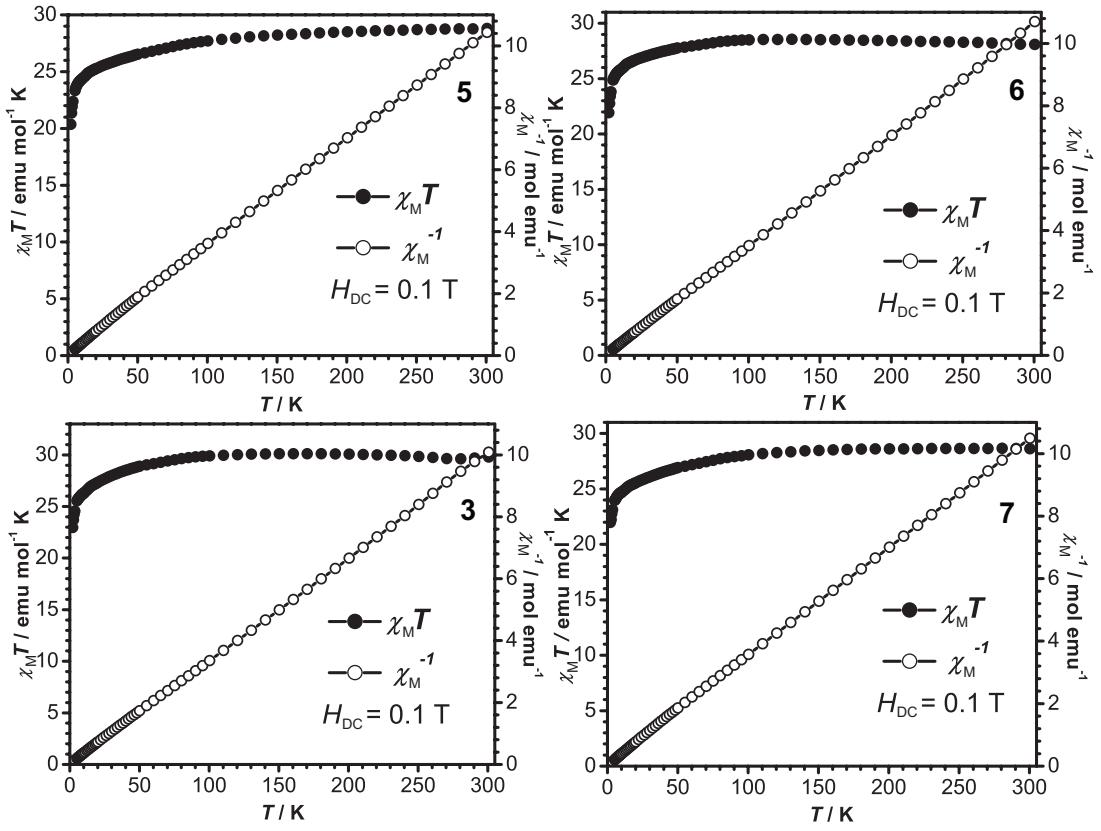

Figure 3.6: Direct current magnetic properties of the compounds. Temperature dependence of the χ_MT product for the compounds **3**, **5** – **7**, recorded at H_{DC} = 0.1 T.

Direct-current (DC) magnetic susceptibilities have been measured on randomly oriented samples **3**, **5** – **7** under an applied dc field of 0.1 T and in the temperature range of 300 – 1.8 K, Figure 3.6.

At 300 K, the χ_MT values of compounds **3**, **5** – **7** are 29.79, 28.80, 28.08, and 28.63 emu K mol^{-1}, respectively, compatible with the theoretical value 28.34 emu K mol^{-1}, for two non-interacting Dy(III) ions ($^6H_{15/2}$, S = 5/2, L = 5, g$_J$ = 4/3)[134]. Upon cooling, χ_MT descends gradually until ca. 80 K, and then decreases more abruptly, reaching values of 20.4 (**5**), 21.9 (**6**), 23.0 (**3**), and 21.9 (**7**) emu K mol^{-1}, respectively, at 1.8 K. This behaviour is ascribed to the progressive thermal depopulation of the excited m$_J$ sub-levels of the ^{6}H$_{15/2}$ ground state of the Dy(III) ion[123, 124].

The M versus H plots for **3**, **5** – **7** at 1.8 K shows a rapid increase in the magnetisation at a low field (Figure 3.7) and a linear increase at a high field to reach the values of magnetisation for **5**, **6**, **3**, and **7** at 1.8 K and 7 T is 10.4 Nβ, 10.8 Nβ, 11.8 Nβ, 11.2 Nβ, and 11.4 Nβ respectively. These values are smaller than the expected saturation magnetisation ones, M_s/Nβ = 2g$_J$J, (for a Dy(III) ion, M$_s$/Nβ = 20, g$_J$ = 4/3, J = 15/2) for the two Dy(III) ions[135]. The large discrepancy from the theoretical saturation value is likely because of crystal effects leading to a significant magnetic anisotropy[20].

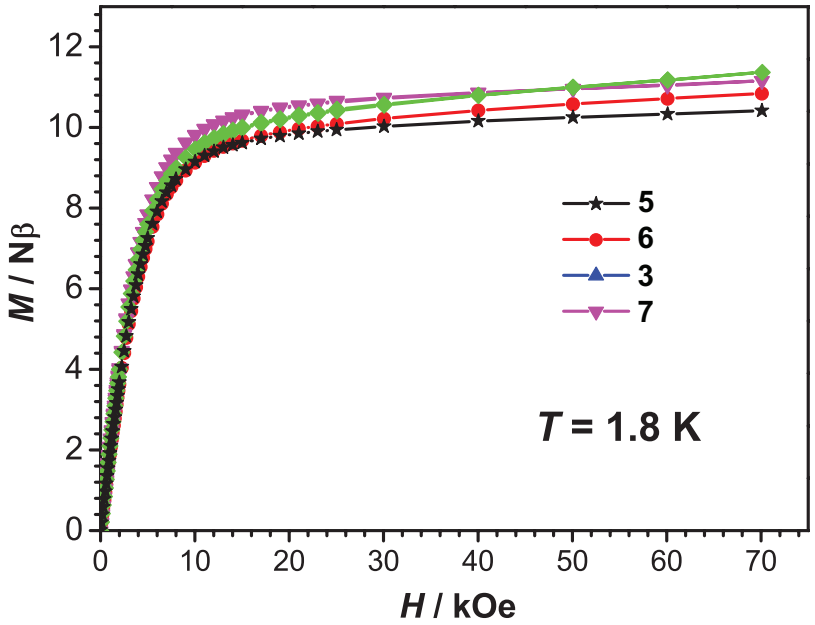

Figure 3.7: Field dependence of the magnetisation ($\boldsymbol{M}$) for **3**, **5** – **7** at T = 1.8 K, indicating for a significant magnetic anisotropy and/or low-lying excited state present in these systems.

Recently, the semiempirical electrostatic model based on the Radical Effective Point Charge (REC)[136] has been proved as an effective theoretical method as *abinitio* calculations[137] to better understand magnetic behaviour of SMMs[80, 138–143]. Here, we used this REC model to predicate and understand magnetic easy axis and their orientation for each dimer by taking into account the oblate 4f-electron cloud of Dy(III) ion in the ground state interacting with its environment in the Ising limit. For these calculations, we employed the SIMPRE computational package[144, 145]. All simulation was performed

on the molecular structures of **3** and **5** – **7** determined by single-crystal X-ray diffraction. Recalling the compressed electron cloud presumed by Ising limit, the direction of the magnetic easy axis tends to orient the quantised axis along the direction of larger and closer negative charges[138]. In the studied case of Dy(III)/β-diketone using the REC model, the effective charge of each coordinating oxygen atom from the hfac ligand is -1/3[140], while those for nitrogen atom from bpm ligand and oxygen atom from solvent molecules are negligible, because the two coordinating nitrogen atoms and one oxygen atom from solvent molecule bear relatively small charges and are further from the Dy(III) center[140, 142]. The calculated magnetic anisotropy axis of the Dy(III) ions in **3**, **5** – **7** are shown in their corresponding molecular structures. For all complexes, the calculated magnetic easy axes of the individual Dy(III) centres were almost parallel to each other. Their orientation is closely perpendicular to the vector connecting the two Dy(III) ions. More specific, the magnetic anisotropy axis in **5** passes through the trans-hfac$^-$ ligands due to the two anti-side β-diketone ligands with four large negative charged oxygen atoms lowering the potential energy compared with the bpm and the last hfacligands, consistent with the reported mononuclear Dy(III)/β-diketone[142]. Although adding one additional solvent molecule, the similar magnetic easy axis through trans-hfac ligands in the rest complexes (**3**, **6** and **7**) can be calculated. Such behaviour can be attributed to minimum repulsive contacts between ligand and f-electron charge clouds[80] by means of placing oblate electron density plane of Dy(III) ion between two largely negative trans-hfac ligands[142].

Dynamic Magnetic Measurements

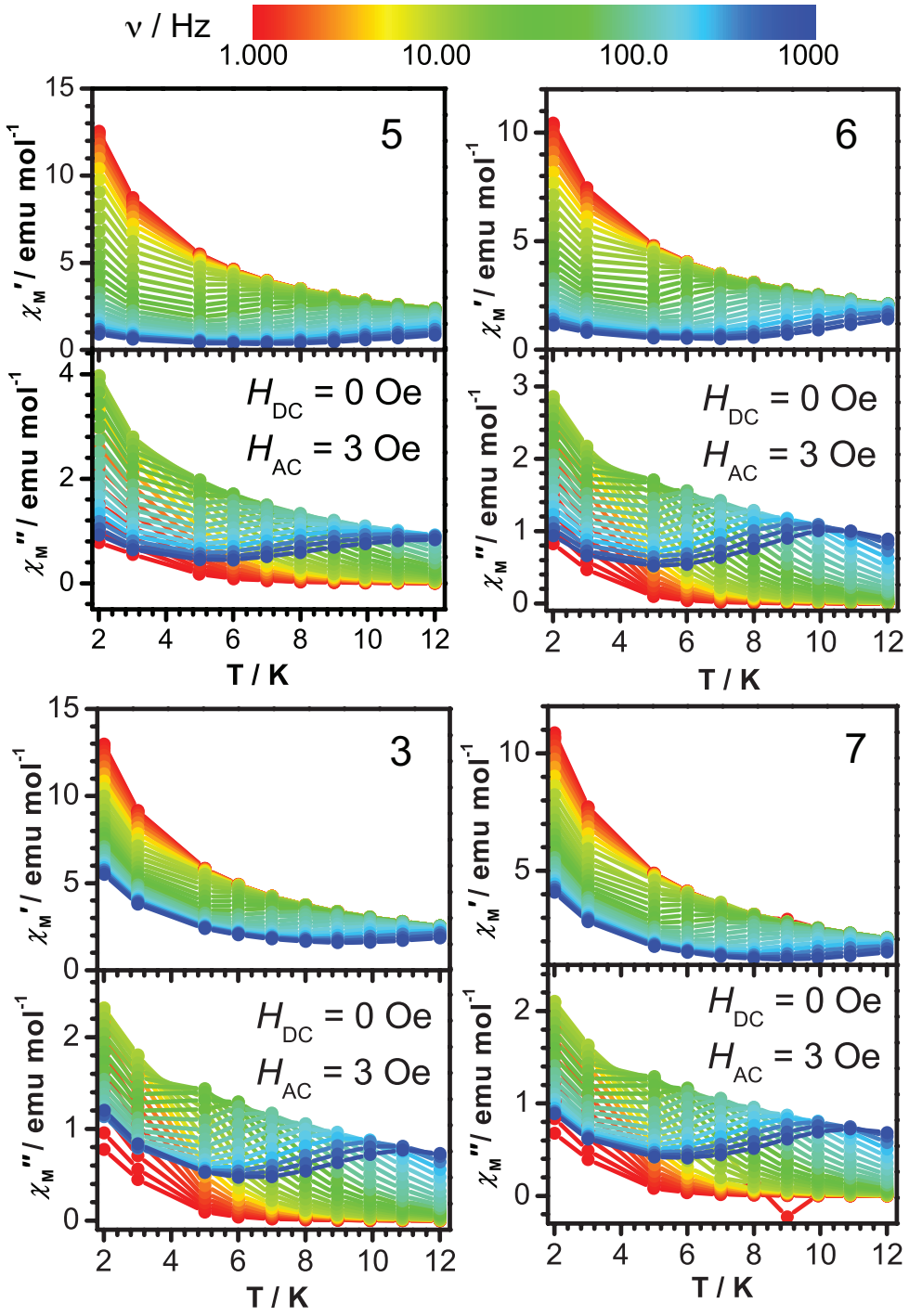

Figure 3.8: Temperature-dependence of the molar in-pahse χ_M' and out-of-phase χ_M'' components of AC susceptibility for **3**, **5** – **7** under zero static field at different frequencies. The different frequencies of the oscillating field are represented in the colorscale, common for all graphs.

To probe the magnetisation dynamics of **3**, **5** – **7**, AC magnetic susceptibilities at various temperatures and frequencies have been performed on powder samples to determine whether or not they exhibit SMMs behaviour.

Temperature-dependent AC susceptibilities for **3**, **5** – **7** are shown in Figure 3.8. All four complexes show a frequency dependence of the out-of-phase (χ_M'') susceptibility, indicating the presence of slow relaxation of magnetisation associated SMMs behaviour. On further cooling, a distinct increase of the tail of χ_M' and χ_M'' signals is observed below ca. 5 K, which can be defined as crossing temperature from the thermally activated dominated relaxation to the quantum tunnelling dominated mechanism[61, 146–148]. The appearance of this tail indicates the existence of QTM.

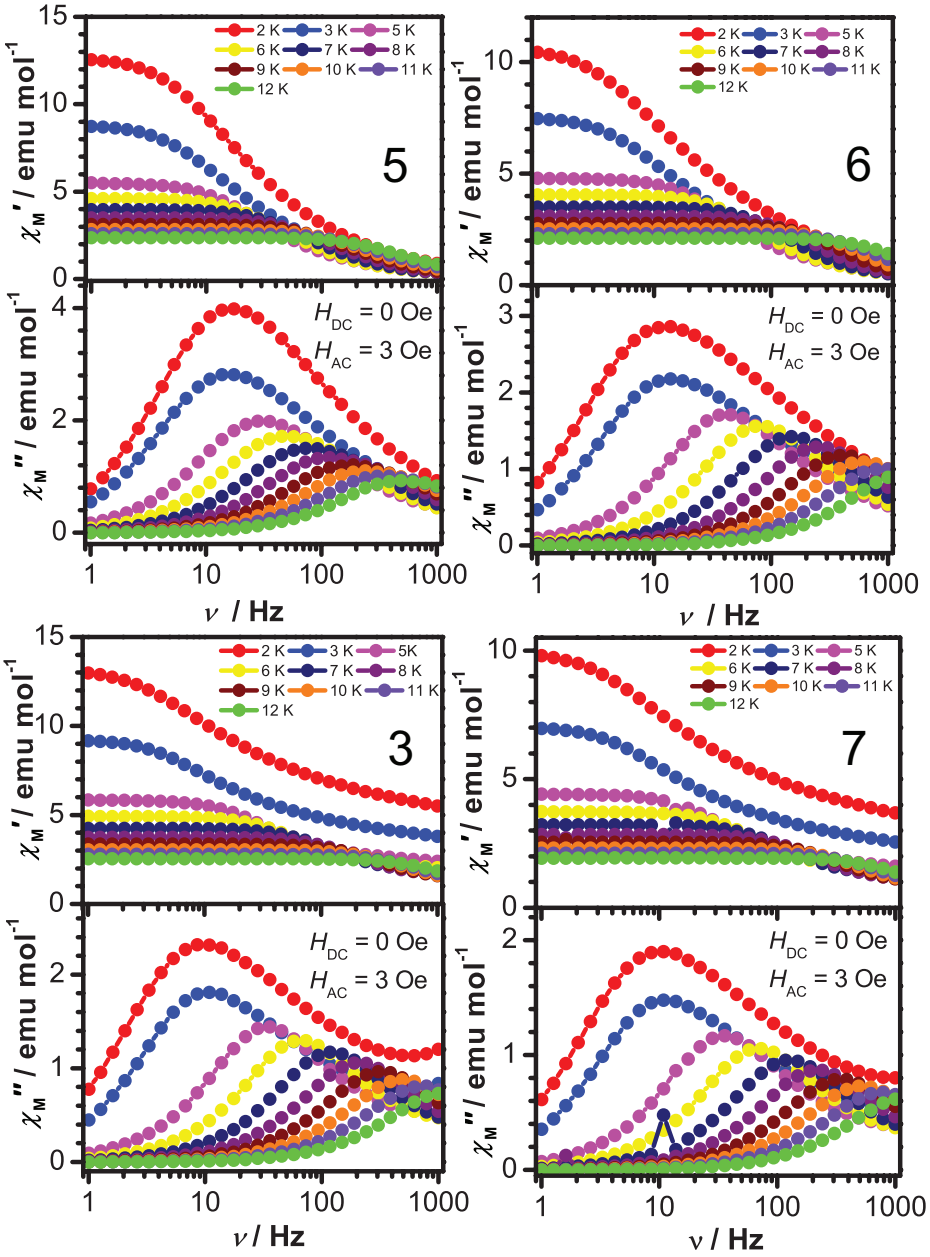

Figure 3.9: Frequency dependence of the molar in-phase χ_M' and out-of-phase χ_M'' components of ac susceptibilities for **3** and **5** – **7** under zero static field at different temperatures.

Further evidence of slow magnetic relaxation for **3**, **5** – **7** was obtained by analysing the dynamics of the magnetic properties, and the relaxation time can be extracted from

the curves of AC susceptibility as a function of oscillating frequency of fields (see Figure 3.9). Plotting the exacted time as a function of the inverse of the temperature afforded the Arrhenius plots in Figure 3.10. For **3**, **5** – **7**, it can be seen that relaxation time τ is temperature-dependent below ca. 5 K, consistent with the aforementioned the occurrence of QTM. On the other hand, τ is temperature-dependent above 5 K, showing Arrhenius behaviour. Moreover, a gradual crossover to a temperature-independent regime for all compounds is observed, which implies that the thermal and the quantum tunnelling of magnetisation mechanisms coexist.

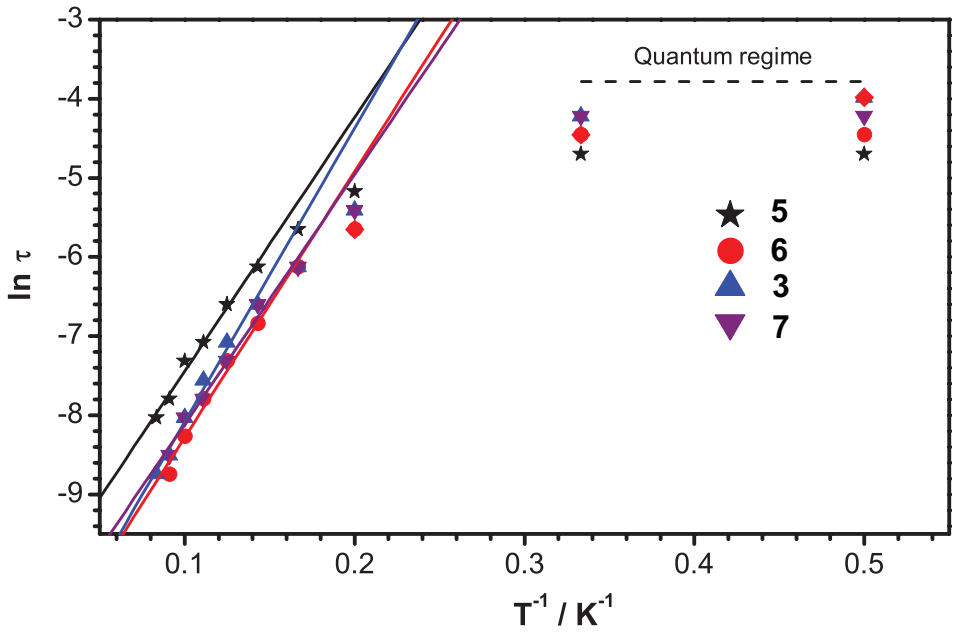

Figure 3.10: Arrhenius plots of the compounds, with colours indicating different compounds (**5**-black; **6**-red; **3**-blue; **7**-purple). Lines are best fits to the data.

The parameter effective energy barrier $U_{\text{eff}}/k_{\text{B}}$ and pre-exponential factor τ_0 for **3**, **5** – **7**, evaluated by a linear fit to Arrhenius law $\tau = \tau_0 \exp(U_{\text{eff}}/k_{\text{B}}\text{T})$ (k_{B} is Boltzaman constant) are obtained, giving value of the effective energy barrier $U_{\text{eff}}/k_{\text{B}} = 32 \pm 2$ K and $\tau_0 = 2.37 \times 10^{-5}$ for **5**, $U_{\text{eff}}/k_{\text{B}} = 34 \pm 2$ K and $\tau_0 = 8.82 \times 10^{-6}$ for **6**, $U_{\text{eff}}/k_{\text{B}} = 37 \pm 2$ K and $\tau_0 = 7.58 \times 10^{-6}$ for **3**, and $U_{\text{eff}}/k_{\text{B}} = 32 \pm 2$ K and $\tau_0 = 1.28 \times 10^{-5}$ for **7**, $\text{R}^2 > 0.98$, respectively. These results are comparable in magnitude to the anisotropy barriers of dinuclear Dy(III) SMMs in the literature[25, 65, 149]. The relatively large value of τ_0 confirms that QTM remains operative even where the thermally activated relaxation is prevailing.

The analysis of peak temperature T_p in χ_{M}'' signals (Figure 3.9) that shift toward higher temperatures with increasing frequencies was made by using Mydosh formula $F = (\Delta\text{T}_p/\text{T}_p)/\Delta(\log\nu)$[75, 150], where ΔT_p is the difference between the highest and lowest blocking temperatures corresponding to the extremes of the investigated frequency ν that appears. The extracted F values for **5**, **6**, **3**, **7** are 0.28, 0.23, 0.24, and 0.24, respectively, in the normal range $0.1 < \text{F} < 0.3$[75] for superparamagnetic materials, which suggest the magnetic behaviour of all compounds could not originate from spin glass behaviour.

To elucidate the details of the relaxation dynamics for the four complexes, the frequency-dependency AC susceptibility signals (Figure 3.9) for **3**, **5** – **7** were further analysed and the corresponding Argand plots were constructed between 2 and 12 K (Figure 3.11). We can have direct access to the width of the distribution of the relaxation rate by fit to the generalised Debye model (see **Chapter 1**).

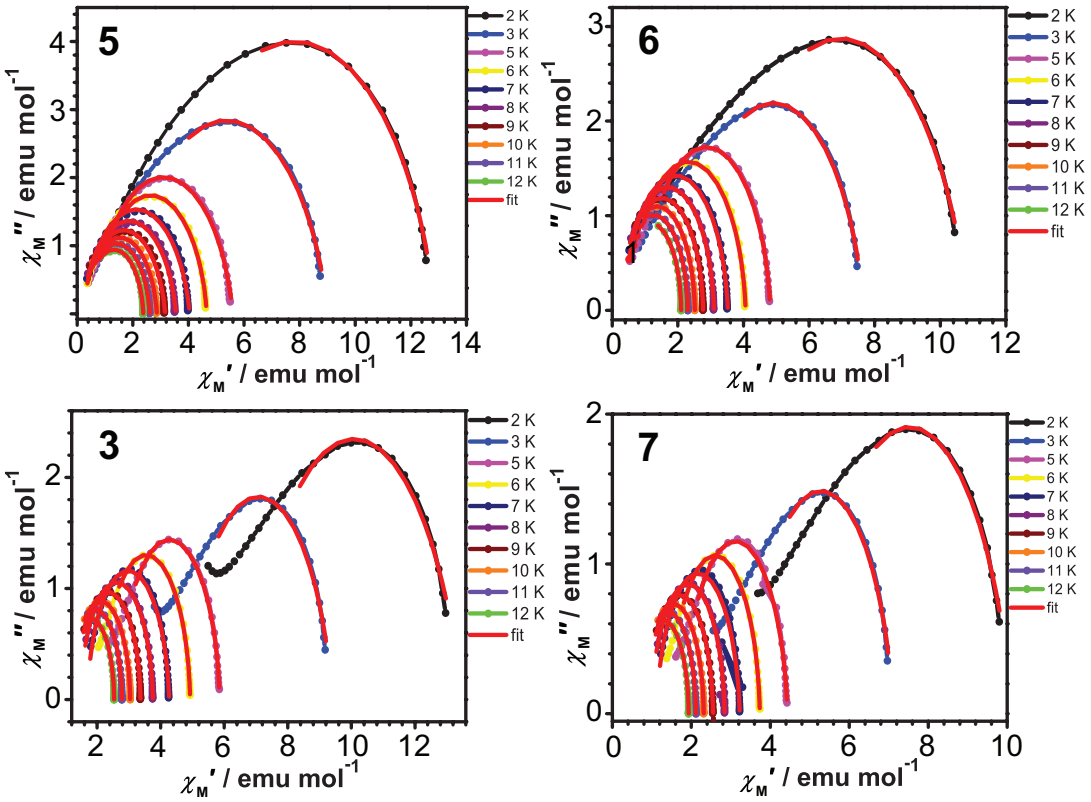

Figure 3.11: Argand plots obtained under zero static magnetic field for compounds **3** and **5** – **7** between 2 K and 12 K, with red lines representing fit with an generalised Debye model.

The fit provides a distribution coefficient α values with being $\alpha = 0.07$ (12 K) – 0.15 (2 K) for **5**, $\alpha = 0.01$ (12 K) – 0.19 (2 K) for **6**, $\alpha = 0.02$ (12 K) – 0.23 (2 K) for **3**, and $\alpha = 0.01$ (12 K) – 0.19 (2 K) for **7**, $R^2 > 0.99$, all indicating a narrow distribution of relaxation process in the investigated temperature ranges.

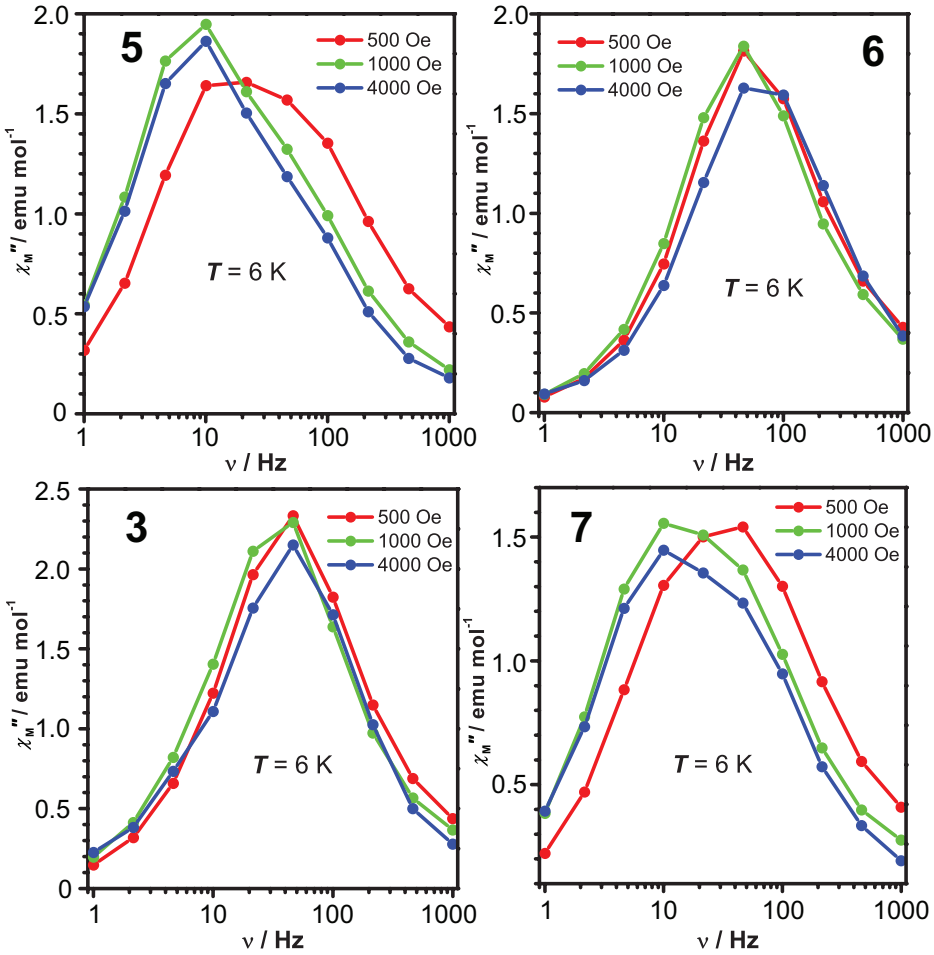

Figure 3.12: Field dependence of the molar out-of-phase χ_M'' components of AC susceptibility for complexes **3**, **5** – **7** at 6 K.

The QTM can be partly or fully suppressed by applying a external static field, always resulting in an increase of the effective anisotropy barrier. Thus, AC susceptibilities for **3**, **5** – **7** were measured under an external static field of H_{DC} = 4 kOe, Figure 3.14 (this magnetic was chosen because it induces the slow relaxation rate, see Figure 3.12).

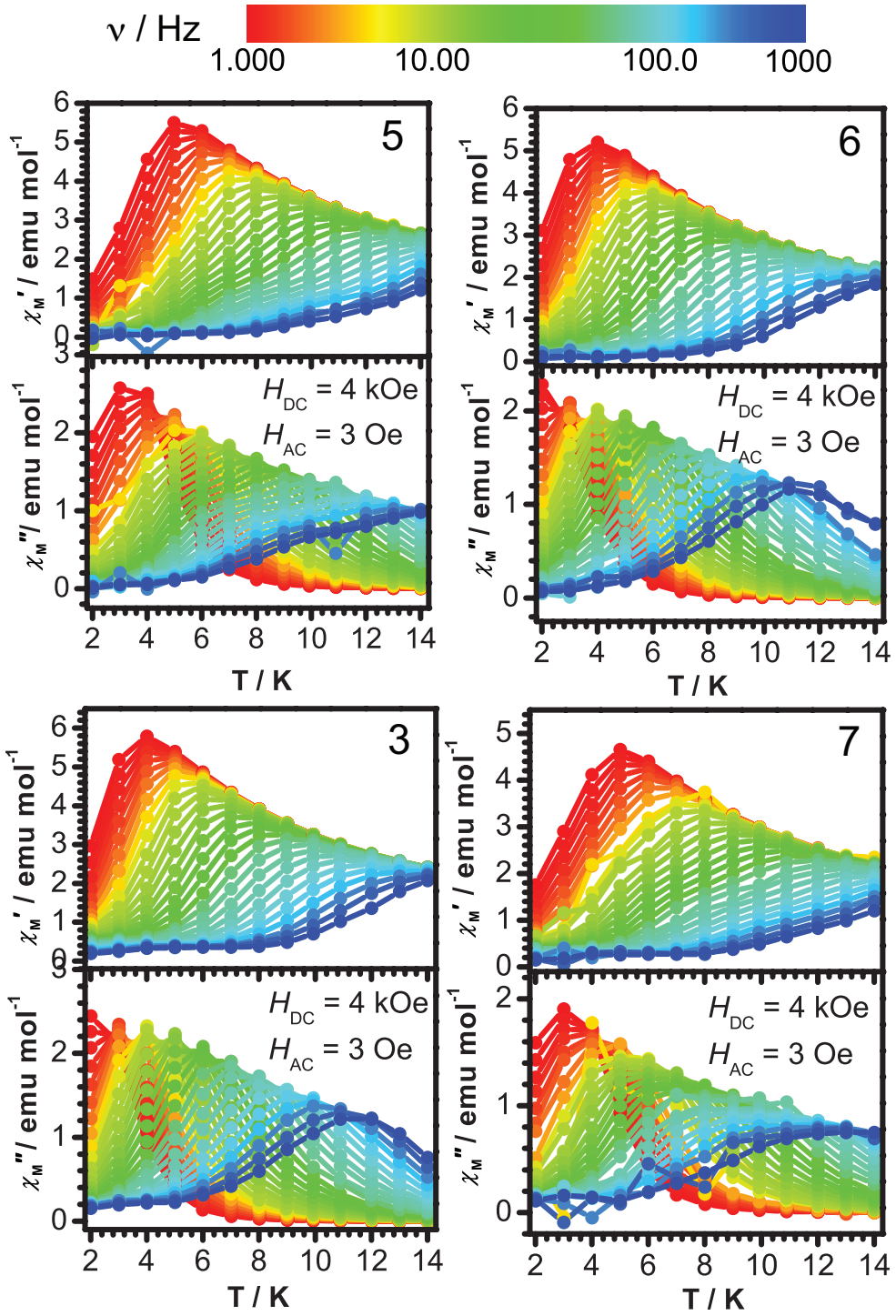

Figure 3.13: Temperature dependent in-phase χ_M' and out-of-phase χ_M'' components of AC susceptibilities in $H_{DC} = 4$ kOe for compounds **3**, **5** – **7**. The different frequencies of the oscillating field are represented in the color-scale, common for all graphs.

For **3**, **5** – **7**, the χ_M' and χ_M'' signals display an overall reduction in height due to saturation effects on depressing the AC susceptibility. The results distinctly demonstrate the disappearance of the tail at the low temperature and an enhancement of the high-temperature frequency-dependent peak. Interestingly, no significant shift of the maximum

position of χ_M'' for **3**, **5** – **7** was observed for DC fields up to 4 kOe, compared to that found under zero static field.

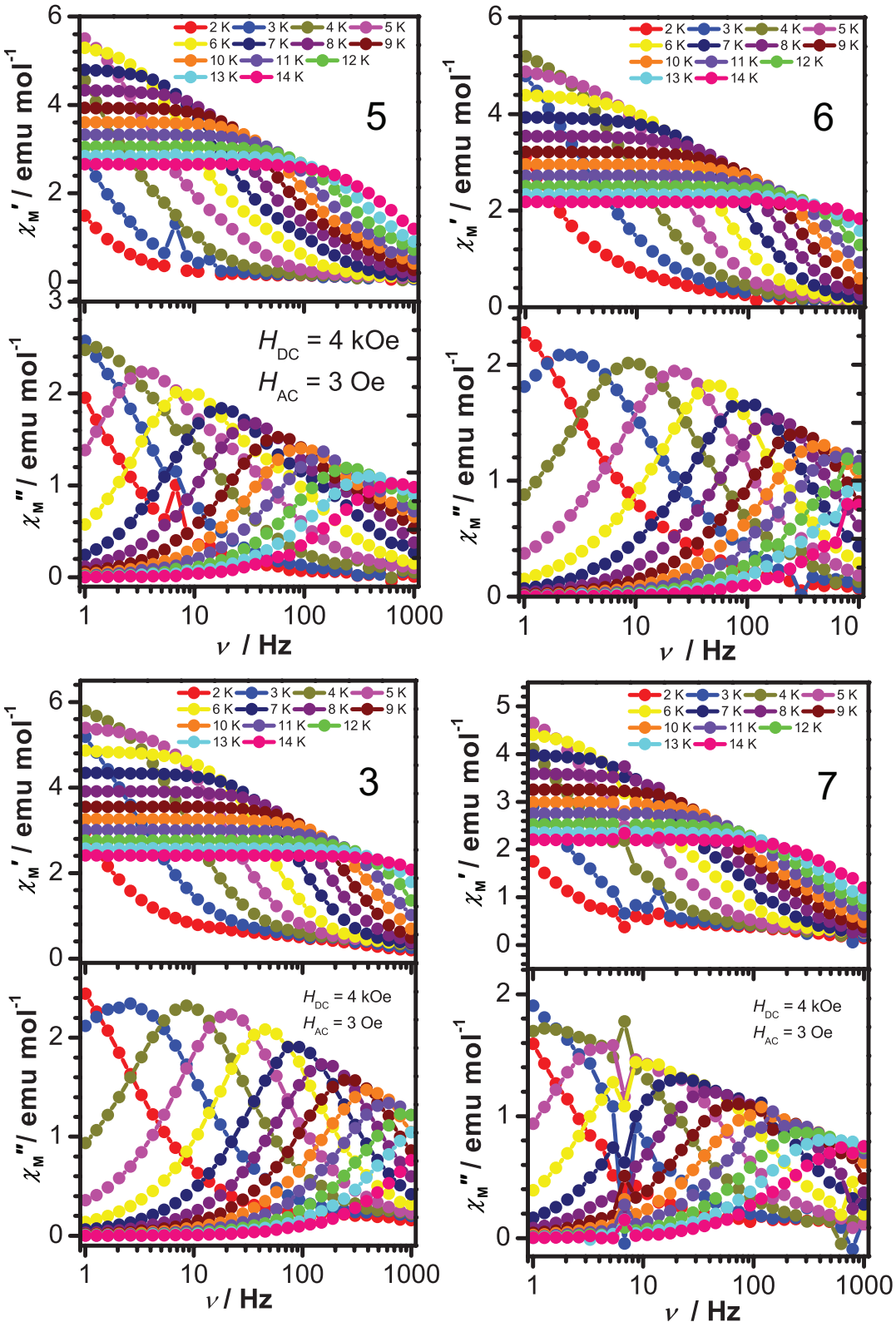

Figure 3.14: Frequency dependent molar in-phase χ_M' and out-of-phase χ_M'' components of AC susceptibility in 4 kOe in the temperature range of 2 and 14 K for **3**, **5** – **7**.

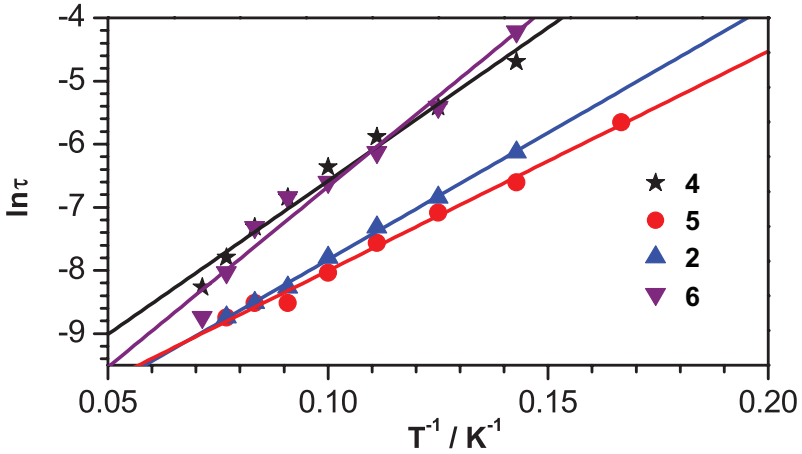

Figure 3.15: Arrhenius plots of complexes **3**, **5** – **7** under 4 kOe: **5**-black, **6**-red, **3**-blue and **7**-purple. Lines are fits to the experimental data.

Linear regression on the Arrhenius plots for **3**, **5** – **7** (Figure 3.14) leads to a small increase of the thermal energy barrier, being $U_{\text{eff}}/k_{\text{B}} = 49 \pm 3$ K and pre-exponential factor $\tau_0 0 = 1.08 \times 10^{-5}$ for **5**, $U_{\text{eff}}/k_{\text{B}} = 35 \pm 1$ K and $\tau_0 = 1.04 \times 10^{-5}$ for **6**, $U_{\text{eff}}/k_{\text{B}} = 40 \pm 1$ K and $\tau_0 = 7.14 \times 10^{-6}$ for **3**, $U_{\text{eff}}/k_{\text{B}} = 57 \pm 4$ K and $\tau_0 = 4.17 \times 10^{-5}$ for **7**, $R^2 > 0.97$, respectively.

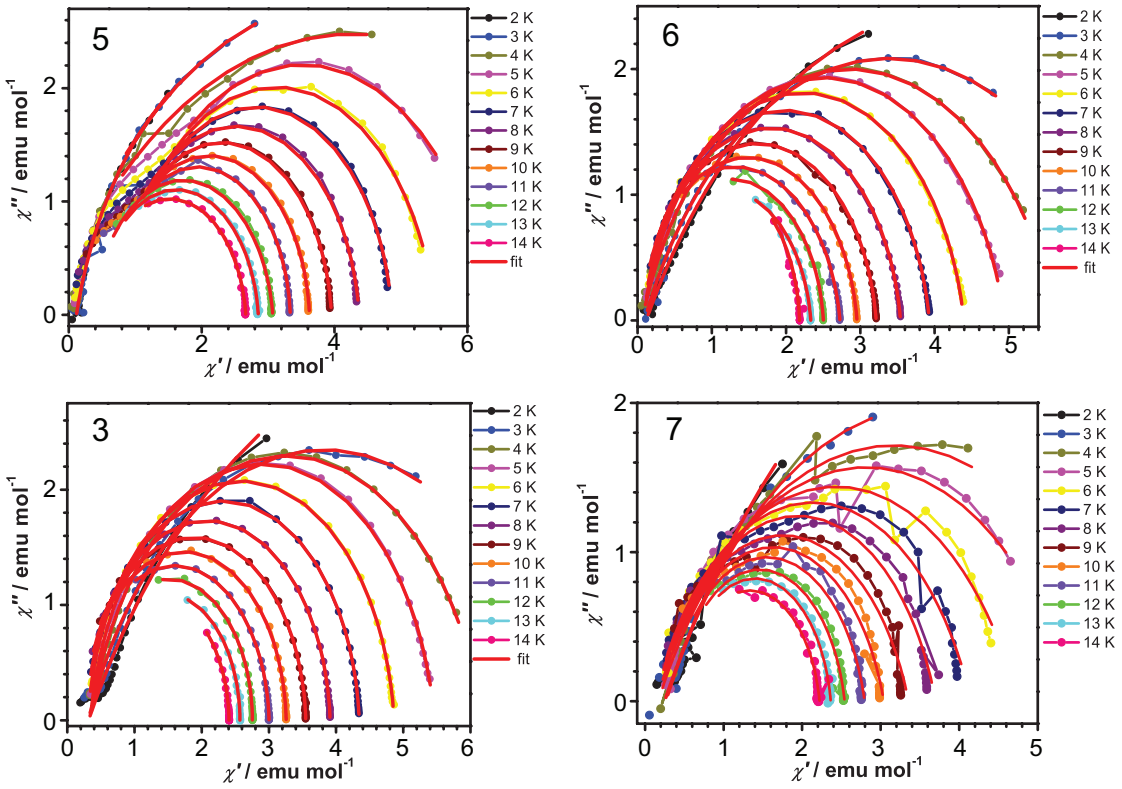

Figure 3.16: Argand plots obtained under 4 kOe in the temperature range of 2 and 14 K for **3**, **5** – **7**.

The robustness of dynamics was checked by analysis of Argand diagrams by using an extended Debye model (Figure 3.16), The distribution coefficient α values are 0.07 (14 K)

– 0.16 (2 K) for **5**, 0.03 (14 K) – 0.34 (2 K) for **6**, 0.02 (14 K) – 0.34 (2 K) for **3** and 0.11 (14 K) – 0.37 (2 K) for **7**, $R^2 > 0.97$, respectively. These ranges indicate a narrow width of the relaxation process in these systems.

4 Intact Dy(III)-SMMs on Surfaces via Sublimation

The molecular evaporation setup was built with the help of Dr. Stephan Rauschenbach and Dipl. Chem. Sabine Abb at Max Planck Institute at Stuttgart. The SiO_2/Si substrates were provided by M. Sc. Kristina Vaklinova at Max Planck Institute at Stuttgart. The MALDI-TOF mass spectra measurements were done with the help of Dr. Stephan Rauschenbach at Max Planck Institute at Stuttgart. The X-ray photoelectron spectroscopy (XPS) on the samples were performed by Dr. Mitssuharu Konuma at Max Planck Institute at Stuttgart.

4.1 Introduction

Nowadays, utility of SMMs as a electronic unit for the spintronics devices has attracting attention because of their unique magnetic properties on individual molecules, i.e. magnetic hysteresis loops and quantum tunnelling of the magnetisation. However, organising SMMs into real devices while preserving their magnetic properties is a challenging topic. The structural integrity and a reservation of the performance of the SMMs is critical.

As mentioned in **Chapter 2**, fluorinated β-diketones[151] are good shielding blocks which can effectively limit the intramolecular interactions and render the molecules robust. Another advantage of the ligand of this kind is to improve the thermal stability of the complexes, the point of which is supported by the fact that Fe_4 SMMs can be evaporated with facilitate sublimation, when employ of pivaloyltrifluoroacetone (Hpta) instead of dipivaloylmethane (Hdpm)[152]. This makes it possible to evaporate molecular nanomagnets containing fluorinated β-diketones (specially hfac) onto various surfaces.

In this chapter, $[Dy(hfac)_3EtOAc]_2bpm$ (hfac = hexafluoroacetylacetonate, EtOAc = ethyl acetate, bpm = 2,2′-bipyrimidine, compound **3**) introduced in **Chapter 2**, henceforth referred to *Dy dimer*, was chosen to be thermally sublimated on various surfaces in high vacuum (HV). The morphology of the resulting films is analysed using atomic force microscopy (AFM) in tapping mode. MALDI-TOF mass spectrometry is employed in testing the structural stability of the deposited clusters while the electronic integrity is addressed by XPS spectra. Finally the magnetic response of thick films obtained by thermal evaporation of 48 hours is investigated by means of static and dynamic susceptibility and magnetisation measurements.

The experiments are available to be performed within the nanoscale science department of Prof. Klaus Kern at the Max Planck Institute at Stuttgart. Molecular structure of this

Dy dimer and the coordination environment surrounded each Dy(III) ion have been well investigated in **Chapter 2**.

4.2 Experimental Section

4.2.1 Thermal Evaporation and Surfaces

An evaporator, shown in Figure 4.1 is equipped with two quartz crucibles covered by separate shutters. The temperature of the crucible was ramped slowly at 5 – 7 °C per minute up to the sublimation temperature in the range 100–300 °C. The slow ramp rate can ensure an homogeneous heating of the powders inside the crucible. The temperature was monitored using a type K thermocouple. The entire evaporation procedure was carried out at a base pressure lower than 4.0×10^{-7} mbar. During the powder sublimation procedure the sample holder was placed in a shadowed position inside the vacuum chamber, thus avoiding the risk of substrate contamination. The molecular film morphology and thickness were controlled and obtained by varying the evaporation time.

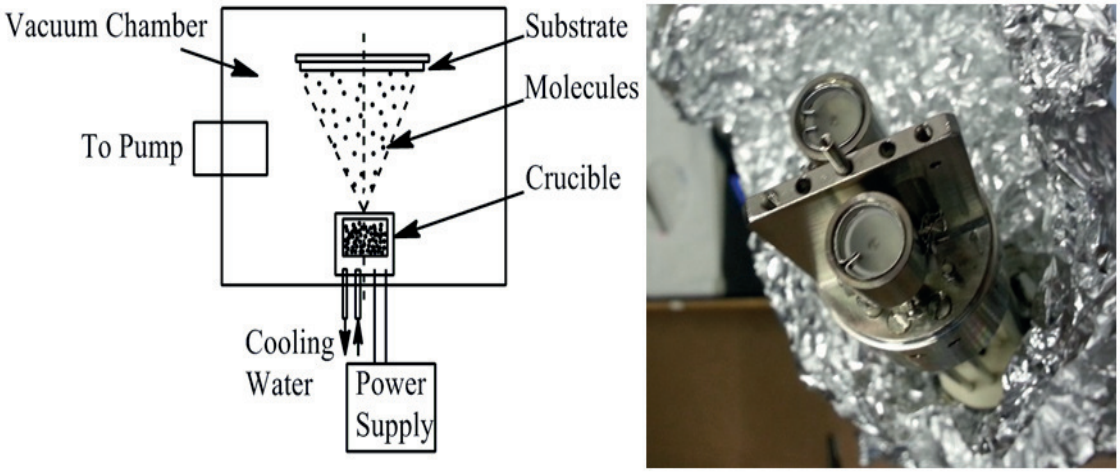

Figure 4.1: Home-made molecular evaporation system. (left) Scheme of the entire molecular evaporation system; (right) two crucibles filled with SMMs powder, each covered by a shutter.

The usual adoptive surfaces are silicon oxide (SiO_2) substrates. Here, ahead of depositing target objects on them, the substrates were treated with aim to obtaining flat and clean surfaces. SiO_2 (300 nm thick)/Si substrates were washed in organic solvents following a polarity gradient: N-ethyl pyrrolidone (NEP), acetone and isopropanol in an ultrasonic bath for 15 min each, shown in Figure 4.2. The use of NEP is to get ride of the PMMA on top of substrate. The samples were eventually dried with an argon jet and immediately loaded in the molecular evaporator, in high-vacuum (HV). Following the three-steps washing, the topography of the resulting structure was imaged by the AFM (see Figure 4.2) and the roughness was determined.

To find the best evaporation conditions we assessed the thermal stability of *Dy dimer* by performing different evaporations at several temperatures on a steel plate and testing

the structural stability of the molecules by means of Matrix-Assisted Laser Desorption / Ionisation Time of Flight (MALDI-TOF) mass spectrometry.

XPS spectra were obtained at room temperature employing an ESCA spectrometer (AXIS Ultra, Kratos Analytical, Manchester, UK) equipped with a hemispherical electron energy analyser. The spectra were measured using monochromatized Al Kα radiation (hν = 1486.58 eV, 150W) and calibrated by setting the C 1s core level peak at 284.80 eV.

The film morphology and thickness were studied in ambient conditions using a Bruker Dimension Icon AFM in tapping mode. Silicon Nitrate tips from Olympus (model: AC200TS) with resonance frequency in the range of 150 kHz and tip radius of 9 $\pm$ 2 nm.

4.3 Results and Discussion

The roughness values are calculated by the AFM software (Nanoscope) as that of the root mean square values of surface height measurements. All the measurements used for calculating roughing are taken from the central areas of the structures, to avoid edge effected and over 2 $\times$ 2 μm^2. In this case, the SiO_2/Si roughness is 0.1 nm (see Figure 4.2).

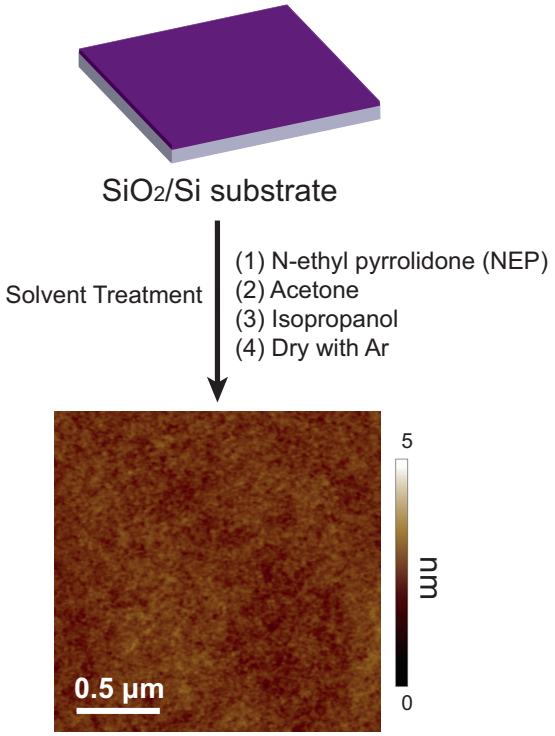

Figure 4.2: AFM topography of SiO_2 surface after washed in organic solvents following a polarity gradient: N-ethyl pyrrolidone (NEP), acetone and isopropanol in an ultrasonic bath for 15 min each. Colour scale range: 0 to 5 nm from black to white.

4.3.1 Deposition

MALDI-TOF mass spectrometry measurements were performed on an AXIMA Resonance MALDI-TOF mass spectrometry (Shimadzu Scientific Instruments, Kyoto, Japan). Negative ion spectra were acquired with a variable repetition rate N_2 laser and were calibrated using fullerene species (including the peaks of $[C_{62}]^-$ (mass = 744 amu), $[C_{68}]^-$ (mass = 816 amu), $[C_{78}]^-$ (mass = 936 amu), $[C_{90}]^-$ (mass = 1080 amu) and others) under the same experimental conditions. Isotopic distributed patterns were simulated using the mMass software, version 5.4.0. Note that no matrix was used.

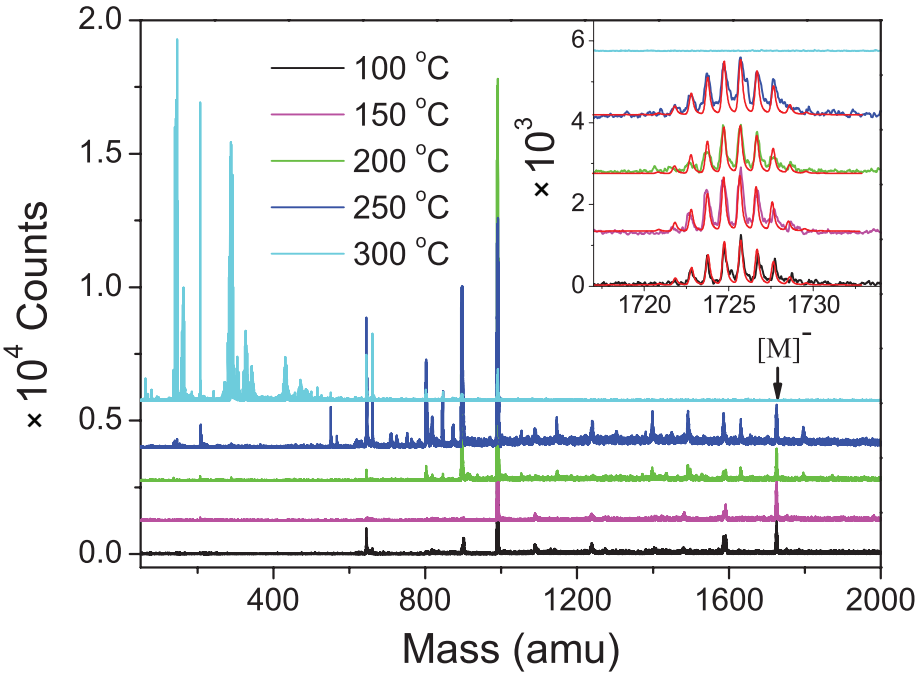

Figure 4.3: MALDI-TOF mass spectra acquired on different samples evaporated on a steel plate at different temperatures, showing the peaks characteristic of intact molecules up to 200 °C, and the decomposition of the molecules above 250 °C. All spectra are recorded in the negative ion mode.

Figure 4.3 shows the negative ion mode MALDI-TOF mass spectra for films evaporated at temperature ranging between 100 and 300 °C. At the lowest temperature, the spectra reports a low level of fragmentation with few characteristic peaks at masses > 1000 amu and a flat response at masses < 600 amu. In particular, the peak at 1725 amu together with its isotopic pattern, Figure 4.3 inset, is the signature of intact $[Dy(hfac)_3]_2bpm^-$ ion. It is probable that the co-crystallising and volatile ethyl acetate molecules are lost under the HV experimental conditions. The recorded isotopic distribution perfectly matches the pattern expected for the intact system. Upon increasing the crucible temperature up to 250 °C, the mass spectra start to show clear signatures of incipient molecular decomposition with the gradual appearance of additional peaks at masses < 600 amu. At temperatures above 250 °C the system decomposes completely affording no peaks in the high mass and several very intense peaks with masses < 600 amu.

The above results demonstrate that intact molecules can be evaporated at temperatures below 200 °C and thus the temperature region for evaporation is well defined. In the following, an evaporation temperature of 150 °C was used.

4.3.2 Surface Characterisation

MALDI-TOF mass spectrometry

To study in detail the fragmentation behaviour of *Dy dimer* molecule, we performed the deposition at 150 °C on an insulating substrate (SiO_2) and compared its MALDI-TOF mass spectrum with the one from the source powder material, shown in Figure 4.4. The characteristic peaks detected in the whole region and their assignments are listed in Table 4.1.

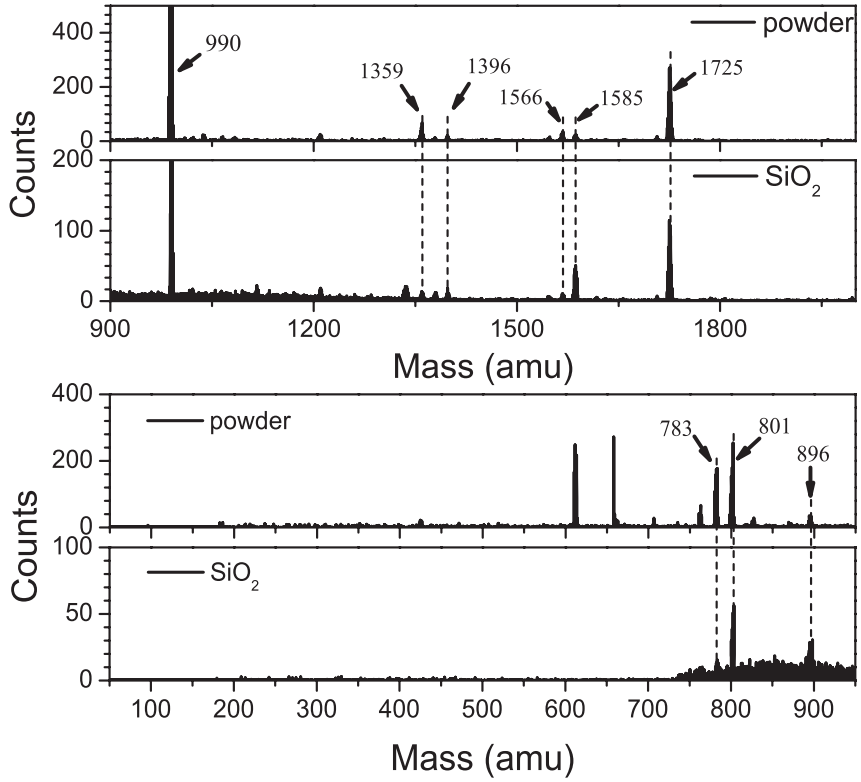

Figure 4.4: Comparison of high mass region of the MALDI–TOF mass spectra acquired on the pristine powder (top) and on thin layers evaporated on SiO_2 surface with sub-monolayer thickness (bottom). All spectra are recorded in the negative mode. The MALDI-TOF mass spectra measurements were done with the help of Dr. Stephan Rauschenbach at Max Planck Institute at Stuttgart.

The spectrum of the deposited molecules matches very well the powder one, exhibiting the molecular peak at 1725 amu together with other peaks of lower mass characteristic of fragments created during the desorption/ionisation process. The peaks associated isotopic patterns allow a quick and precise distinction between molecular fragments containing 1 Dy atom (where an asymmetric peak pattern is expected) or 2 Dy atoms (where the peak pattern is symmetric, with the highest-intensity peaks at the centre).

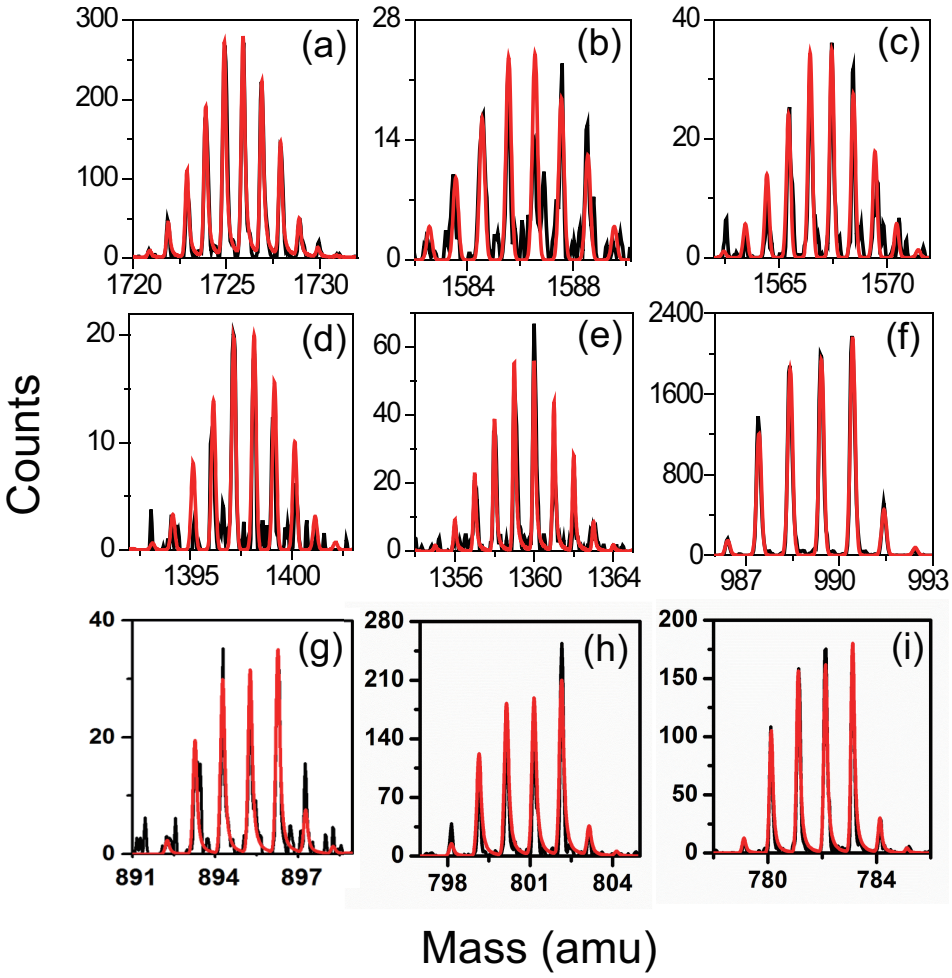

Figure 4.5: MALDI-TOF mass spectra of powder and molecules on SiO_2 substrate. All spectra are recorded in the negative ion mode.

Table 4.1: Characteristic peaks detected in the negative channel of MALDI-TOF mass spectra, with their assignments. All peaks are detected in both the powder and sub-monolayer of molecules on SiO_2 surface.

Mass[amu]	Assignment	Fragments
1725	$[M]^-$	$L^*{}_3Dy(R_1{}^{**})DyL_3$
1585	$[M\text{-}2R_2{}^{***}\text{-}H]^-$	$L_3Dy(R_1)Dy(C_5F_6O_2)_2(C_3HO_2)$
1566	$[M\text{-}2R_2\text{-}F\text{-}H]^-$	$L_3Dy(R_1)Dy(C_5HF_5O_2)(C_4HF_3O_2)_2$
1396	$[M\text{-}4R_2\text{-}3F\text{+}5H]^-$	$L_3Dy(R_1)Dy(C_5HF_3O_2)(C_3HO_2)_2H_5$
1359	$[M\text{-}5R_2\text{-}2F\text{+}H_2O\text{-}H]^-$	$L_3Dy(R_1)Dy(C_3HO_2)_2(C_4FO_2)H_2O$
990	$[M\text{-}2L\text{-}R_1\text{-}Dy\text{-}H]^-$	DyL_4
896	$[M\text{-}2L\text{-}R_1\text{-}Dy\text{-}5F]^-$	$L_3Dy(C_5O_2HF)$
801	$[M\text{-}3L\text{-}R_1\text{-}Dy\text{+}H_2O\text{-}H]^-$	$L_2Dy(C_5F_6O_2)H_2O$
783	$[M\text{-}3L\text{-}R_1\text{-}Dy\text{-}H]^-$	$L_2Dy(C_5F_6O_2)$

* L = hexafluoroacetylacetonate (Formula: $C_5HF_6O_2$)
** R_1 = bpm
*** R_2 = CF_3

Figure 4.5 shows the excellent agreement between the isotopic pattern of each fragment and the simulations. The peaks above 1000 amu, show the presence of two Dy centers and are assigned to ion fragments formed by loss of CF_3 groups and F atoms, as shown in Figure 4.5 a - e. Below 1000 amu, the peak at 990 amu (see Figure 4.5f) is attributed to the ion fragment with formula $Dy(hfac)_4$, arising from the rearrangement of *Dy dimer* after the loss of one Dy atom, two hfac groups, and one bpm bridge-ligand. This fragment is particularly stable, and the species can also be synthesised chemically and constitutes a typical sub-product in the synthesis of the $Dy(hfac)_3(H_2O)_2$ building block.

XPS spectra analysis

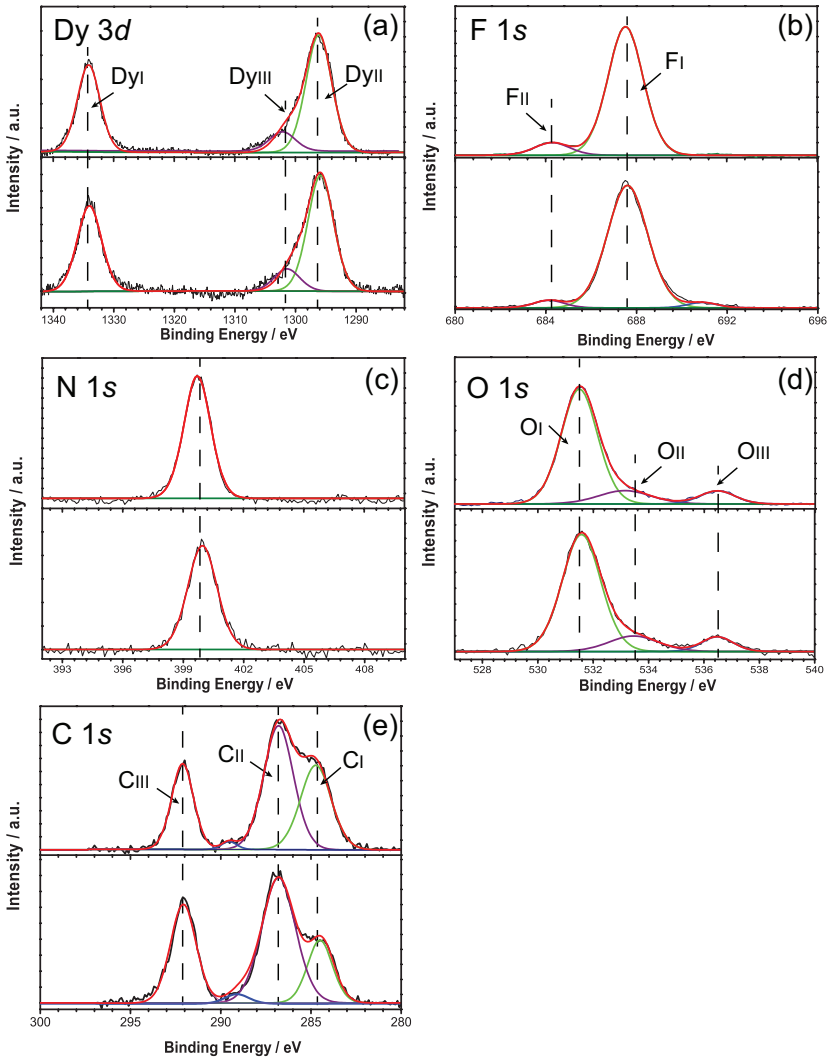

Figure 4.6: Detailed XPS spectra of Dy 3*d* (a), F 1*s* (b) and N 1*s* (c) and O 1*s* (d) peaks carried out on the powder (bottom), thin films on SiO_2 (top). (e) deconvolution of the C 1*s* peaks for the powder and sub-monolayer samples, as predicted considering the molecular building blocks in molecular structure. These XPS measurements were performed by Dr. Mitssuharu Konuma at Max Planck Institute at Stuttgart.

The electronic structure of the sub-monolayer of molecules has been investigated through X-ray photoelectron spectroscopy (XPS). The analysis of XPS data evidences the electronic stability of *Dy dimer* on SiO_2 surfaces. Survey scans were in the 0–1400 eV range and detailed scans were recorded for the C 1*s*, N 1*s*, O 1*s*, F 1*s* and Dy 3*d* peaks. Shirley method[153] was used to evaluate the background and experimental spectra were numerically fitted with the 70% Gaussian + 30% Lorentzian line-shapes (ratio G/L = 30).

Similar to MALDI-TOF mass spectra measurement, source powder sample was firstly characterised as reference. The Dy 3*d*, F 1*s*, N 1*s*, O 1*s* and C 1*s* XPS spectra of the powder and thin films on SiO_2 surface are shown in Figure 4.6, and the corresponding core-level photoelectron binding energy (BE) are collected in Table 4.2.

Table 4.2: Comparison of nominal and experimental composition (% at) as evaluated for by XPS for powder and films. The BE values of the different peaks are also indicated (eV)

Samples	BE (± 0.05 eV)		BE (± 0.05 eV)
Powder			
Dy $3d_{5/2}$	1296.00	F 1*d*	687.40
Dy $3d_{3/2}$	1333.40	N 1*s*	400.00
O 1*s*	531.70		
SiO_2			
Dy $3d_{5/2}$	1295.80	F 1*s*	687.60
Dy $3d_{3/2}$	1333.65	N 1*s*	400.10
O 1*s*	531.50		

Table 4.3: Comparison of nominal and experimental composition (% at) as evaluated for various surfaces by XPS spectra. The BE values of the different peaks are also indicated (eV)

Sample	BE (eV)	FWHM (eV)	% Calc	% Found
Powder				
C_I	284.80	1.80	21.05	21.27
C_{II}	287.20	2.13	47.37	47.22
C_{III}	292.35	1.81	31.58	31.51
SiO_2				
C_I	284.80	1.96	21.05	29.59
C_{II}	286.90	1.95	47.37	47.90
C_{III}	292.20	1.41	31.58	22.51

In the Dy 3*d* region, the $3d_{5/2}$ and $3d_{3/2}$ doublet, at 1296 eV (Dy_I) and 1333 eV (Dy_{II}) respectively, remain unchanged upon molecular evaporation, in comparison with that of the powder. Additionally, one new contribution (Dy_{III}) appears at ca.1299.5 eV, which can be assigned to the interaction with oxygen atoms in Dy_2O_3 impurity[154, 155]. In the F 1*s* and N 1*s* regions, only single contributions can be distinguished at 687.4 and 400.0 eV, respectively, excluding a small contribution at 684.0 eV due to F atoms semi-ionically bound to C atoms[94, 156].

In Table 4.2, we compare the binding energies (BE) of different core elements including Dy 3*d*, F 1*s* and N 1*s* in the XPS spectra of *Dy dimer* in the form of powder and thin-layer on SiO_2 surface. Positions of these peaks are basically identical, which proves the deposited films are composed of intact molecules, without any substantial change in the molecular oxidation state. A further analysis of the C 1*s* signal was attempted by peak deconvolution, and three distinct components were found, as reported in Figure 4.6e. The detail analysis of the deconvoluted high resolution of the C 1*s* peaks and atomic percentages, compared with calculated values, are listed in Table 4.3, which agree with the observed composition.

The C 1*s* region contains three components (see Figure 4.6 e): one at 284.80 eV (C_I) that can be ascribed to C-H and C-C bonding[94]; one at higher ca. 287.00 eV (C_{II}) that is ascribed to C-O and C-N in the hfac and bpym groups[157] and one at ca. 292.30 eV (C_{III}) that can be coherently assigned to carbon atoms covalently bound to fluorine atoms as the CF_3 group in hfac ligands[18, 94, 122, 123].

AFM image analysis

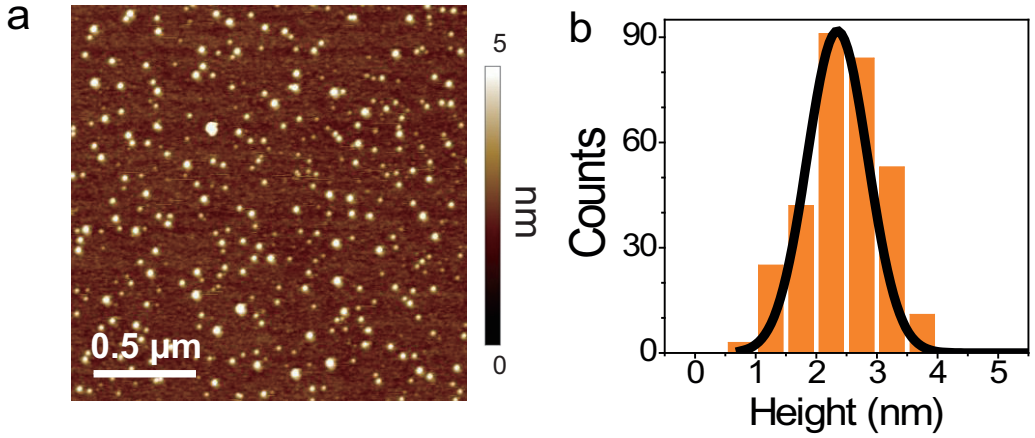

Figure 4.7: a. Height image of the *Dy dimer* molecules in a sub-monolayer deposition on SiO_2 surface for 5 minutes, showing a dense coverage of *Dy dimer*; b. Statistical distribution of molecular diameters extracted from AFM height profiles of the deposited objects in a (bars), and the diameters follow a centre at 2.2 nm with fit to the Gaussian function (black solid curve).

Figure 4.7a represents a typical topographical top-view AFM image ($2 \times 2\ \mu m^2$) after deposition of 5 min, which reveals spherical agglomerates, evenly distributed on the surface. As revealed by statistical analysis of this AFM image in Figure 4.7b, the average height of these objects is 2.2 ± 0.3 nm, a value approximately double the size of individual molecule which is 1.0 – 1.4 nm (average: 1.2 nm), as extracted from X-ray single-crystal diffraction measurements. Moreover, the size of the agglomerates seems to be rather mono-disperse. This provides the fact that indeed truly individual *Dy dimer* molecules were imaged by AFM.

The molecular evaporation technique allows not only the deposition of unaltered *Dy dimer* but also the control of thickness of the deposited films from multilayer down to sub-

monolayer range by adjusting evaporation time. The different topography in deposited structures on SiO_2 surfaces shows a clear dependence on evaporation time (Figure 4.8).

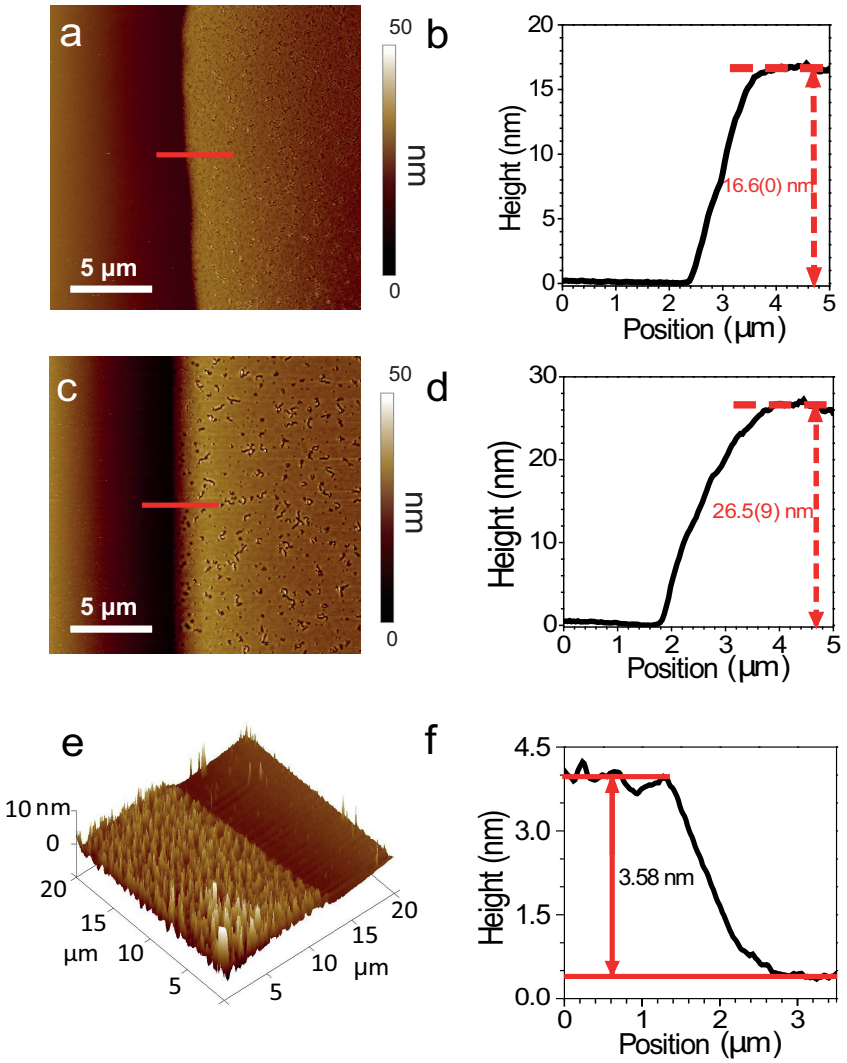

Figure 4.8: AFM characterisation of the deposited molecules with different thickness. (a) and (c) AFM image of the step and relative cross sections of thin films deposited for 10 min and 30 min, respectively; (b) and (d) Height of the crossed region for 10 min and 30 min is 16.6(0) nm and 26.5(9) nm, respectively; (e) three-dimensional plot of the AFM height image of a thin film (three molecular layers) close to the masked area; (f) height profile showing the average height of the deposited film.

Among these images, Figure 4.8a and c are AFM images of films after 10 and 30 min evaporation, respectively. The corresponding films heights are 16.6 nm and 26.5 nm, respectively. Both images clearly demonstrate continuous and uniform think films; while the roughness increases with thickness, suggesting the formation of separated islands on the thick layer. The results evidence that our molecular evaporation is an effective method for producing SMMs films of well-defined morphology, with thicknesses ranging from several tens of nm down to sub-monolayer coverage (see Figure 4.8).

The integrity and morphology of the *Dy dimer* film on surfaces is a necessary but not a

sufficient condition to retain the single-molecule magnet behaviour. Therefore a magnetic characterisation has been performed on the evaporated films of multilayers, as shown hereafter.

4.3.3 Magnetic Characterisation

To study the films magnetic properties, a multilayer sample of total mass equal to around 1.1 mg was produced by thermal evaporation at 150 °C for 48 hours. At this point, it is worthy to note that this sample contains a collection of randomly oriented *Dy dimer* molecules arranged on the surfaces. The SiO_2/Si substrate was chosen, because of its diamagnetic properties and also providing flat surfaces. All the magnetic measurements were performed with the external magnetic field perpendicular to the surfaces of the sample.

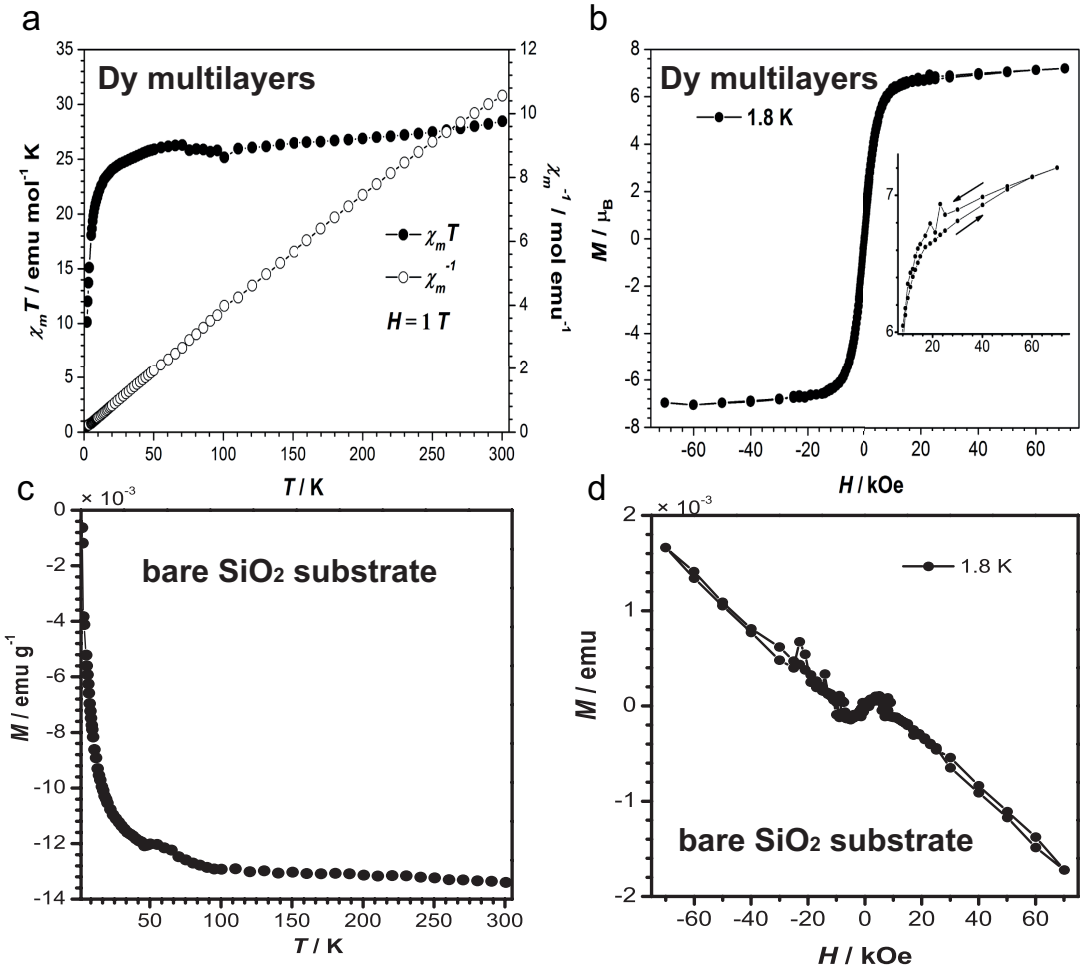

Figure 4.9: Magnetic characterisation of the multilayer systems. a. Temperature dependence of the $\chi_M T$ product for the deposited film on SiO_2 substrate; b. Field dependence of the magnetisation (M) on *Dy dimer* multilayer on SiO_2 substrate at T = 1.8 K, respectively; c. Temperature dependence of magnetisation for SiO_2 substrate; d. Field dependence of the magnetisation of SiO_2 substrate at T = 1.8 K. Both c and d indicate the diamagnetic behaviour of SiO_2 substrate.

Static magnetic susceptibility together with magnetisation data of the films on substrate are shown in Figure 4.9. To accurately account for the bare substrate contribution, measurements were carried on the bare substrate under the same conditions. All the data were corrected for the diamagnetic contribution of the SiO_2 substrate (see Figure 4.9c and d).

Static magnetic susceptibility studies were carried out in an applied magnetic field of 10 kOe in the temperature range 1.8 – 300 K. The plot of $\chi_M T$ as the function of temperature is shown in Figure 4.9a. At 300 K, the $\chi_M T$ value of 28.5 emu K mol^{-1}, is in good agreement with the theoretical value of 28.34 emu K mol^{-1} for two non-interacting Dy(III) atoms ($^6H_{15/2}$, $S = 5/2$, $L = 5$, g = 4/3). Upon lowering the temperature, the $\chi_m T$ product decreases slowly firstly, and then drops rapidly below T = 50 K, down to a minimum value of 10.1 emu K mol^{-1} at 1.8 K. This behaviour agrees perfectly with the behaviour of crystalline powders of the *Dy dimer* (see **Chapter 2**), and is largely due to the thermal depopulation of the Dy(III) Stark sub-levels[158]. The bistable magnetic properties of SMMs can be evidenced via the magnetic hysteresis curve, which is also present in the deposited structures, Figure 4.9b.

The significant amount of magnetic material on surface also allows a characterisation via AC susceptibility. The bare substrate used to hold the film was firstly measured. the imaginary components results is shown in Figure 4.10c. No frequency dependent χ'' peak was observed. The powder sample baked at 150 °C was also measured, for better comparison with the multilayer on substrate. The temperature dependence of the ac susceptibility in the frequency range of 1 – 1000 Hz for baked sample and the deposited film under zero static magnetic field are reported in Figure 4.10a and b, respectively. Both show nearly same magnetic behaviour. Figure 4.10b reveals a frequency dependent maximum in the out-of-phase component χ'' at frequencies higher than 32 Hz, a behaviour that is typical for SMMs associated to thermally activated process. Below ca. 5 K, χ'' exhibit an appreciable increase characteristic of dysprosium(III)-based SMMs indicative of dominant quantum tunnelling.

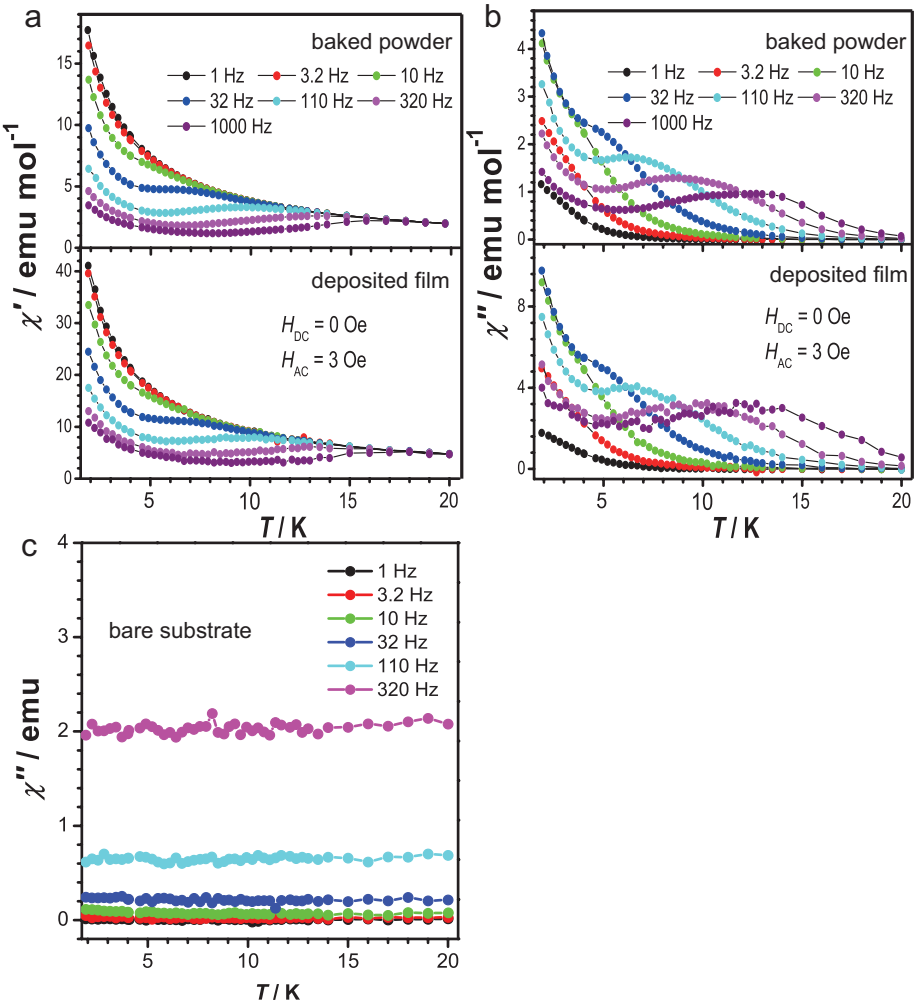

Figure 4.10: Real and imaginary components of the magnetic susceptibility in zero static field. a. Temperature dependence of the imaginary part of the AC susceptibility for baked *Dy dimer* (top) and deposited film on SiO_2 substrate (bottom) at 150 °C. b. Temperature dependence of the imaginary part of the ac susceptibility for baked *Dy dimer* (top) and deposited film on SiO_2 substrate (bottom) at 150 °C. c. Imaginary component of bare substrate as a function of temperature with no peaks, used to linearly subtract its diamagnetic effect. All lines are guides to the eye.

Magnetisation relaxation times below 12 K (Figure 4.11a) and Cole-Cole diagrams at 3 and 6 K (Figure 4.11b) were extracted from the frequency dependence of the AC susceptibility in zero-dc field on the deposited film sample (4.12). Above 5 K, Figure 4.11a, the relaxation follows thermal activated mechanism described by Arrhenius law [$\tau = \tau_0 \exp(U_{\text{eff}}/(k_B T)]$, where k_B is the Boltzmann constant, giving a per-exponential factor $\tau_0 = 8.53 \times 10^{-6}$ s and an energy barrier $U_{\text{eff}} = 35 \pm 2$ K, comparable to that for bulk powder samples. On lowering the temperature below ca. 5 K, the system enters the temperature-independent regime dominated by the quantum-tunnelling relaxation characterised by constant τ_0 value of 0.005 s.

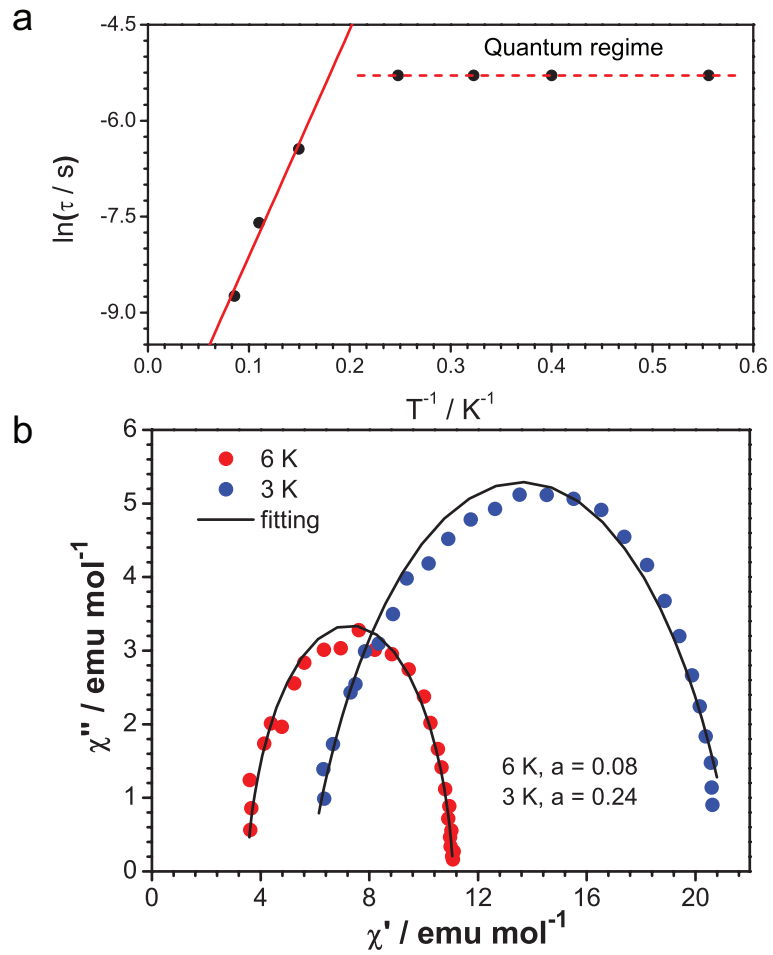

Figure 4.11: a. Temperature dependence of the magnetisation relaxation time ($\ln\tau$ vs. T^{-1}) plot for deposited film on SiO_2 surface under zero static field. The solid line represents the best fit with the Arrhenius law. b. Argand plots measured at T = 3 K and 6 K under zero-dc field. The solid lines are the best fit to the experimental data, obtained with the generalised Debye model with α = 0.2 and 0.08 at T = 3 K and 6 K, respectively.

Figure 4.11b shows two representative Argand curves, acquired at T = 3 and 6 K. The shapes are very close to semicircles, and the data can be fitted with the generalised Debye model (see **Chapter 1**). The fitting parameter α is used to express the presence of a distribution of relaxation times, and it is found to be 0.2 and 0.08 at 3 K and 6 K, respectively. The decrease of on lowering T is likely due to the presence of weak residual intermolecular interactions between SMMs inside the deposited layers.

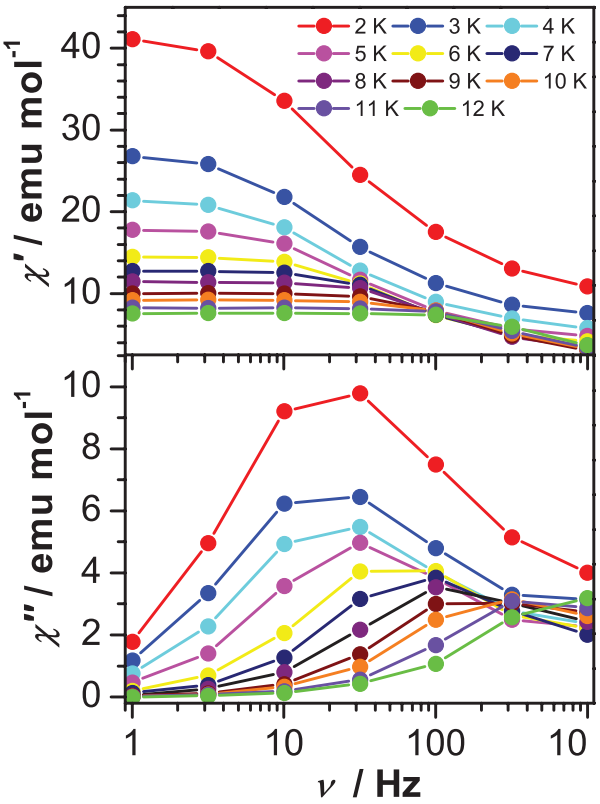

Figure 4.12: Frequency dependence of the AC susceptibility for deposited films on SiO_2 substrate, the AC frequency between 1 and 1000 Hz under a zero static field between 2 and 12 K.

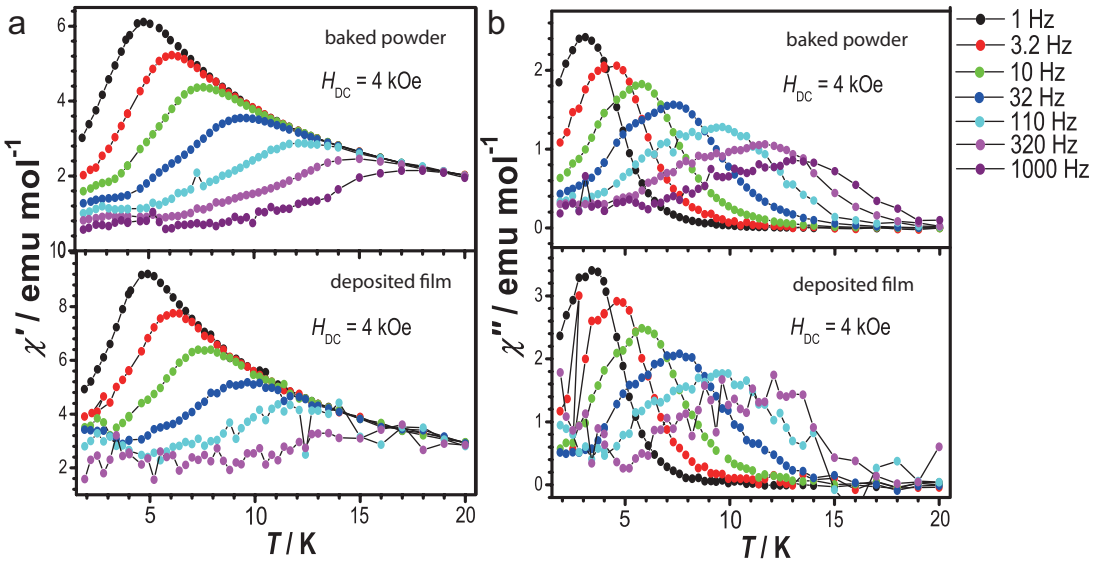

Figure 4.13: Real and real components of the magnetic susceptibility in 4 kOe magnetic field for powder sample and deposited film. a. Temperature dependence of the real part of the ac susceptibility for baked *Dy dimer* (top) and deposited film on SiO_2 substrate (bottom) at 150 °C. b. Temperature dependence of the imaginary part of the AC susceptibility for baked *Dy dimer* (top) and deposited film on SiO_2 substrate (bottom) at 150 °C. All lines are guides to the eye.

The origin of this increase was verified by applying an external magnetic field which

lifts the degeneracy of the magnetic levels and suppresses the quantum tunnelling process for powder sample and deposited film, as shown in Figure 4.13. The measurements in external field of 4 kOe for both show indeed the disappearance of the low-temperature feature and an enhancement of the high-temperature frequency-dependent peak.

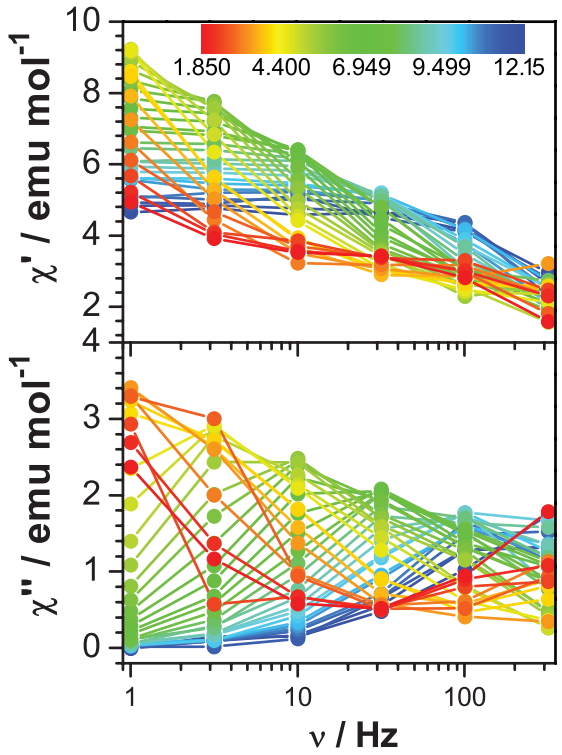

Figure 4.14: Frequency dependence of the AC susceptibility for deposited films on SiO_2 substrate, the AC frequency between 1 and 320 Hz under a zero static field between 2 and 12 K.

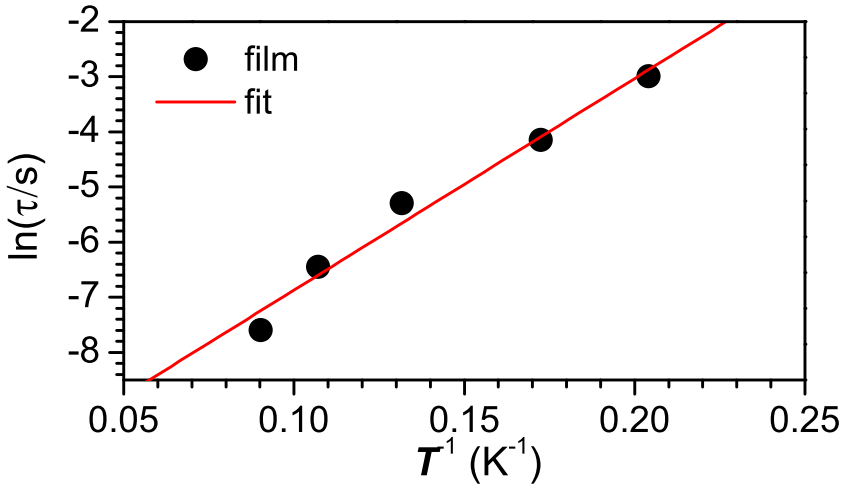

Figure 4.15: Temperature dependence of the magnetisation relaxation time ($\ln\tau$ vs T^{-1}) plot for deposited film on SiO_2 surface under the external field of 4 kOe. The solid line represents the best fit with the Arrhenius law.

Magnetisation relaxation times below 12 K (Figure 4.15) were extracted from the

frequency dependence of the AC susceptibility in a DC field of 4 kOe (Figure 4.14). This relaxation follows thermally activated mechanism described by Arrhenius law [$\tau = \tau_0 \exp(U_{\text{eff}}/(k_{\text{B}}\text{T})]$, where k_{B} is the Boltzmann constant, giving a per-exponential factor $\tau_0 = 2.24 \times 10^{-5}$ s and an energy barrier $\text{U}_{\text{eff}}/k_{\text{B}} = 38 \pm 3$ K, $\text{R}^2 = 0.97$, comparable to that for bulk powder samples measured under 4 kOe (see **Chapter 2**).

5 Noncovalent grafting SMMs onto Nanocarbon materials

Graphene was produced in the cleaning room at Max Planck Institute at Stuttgart. The single wall carbon nanotubes (SWCNTs) were provided from Dr. Mark H. Rmmeli at Leibniz-Institut für Festkörper- und Werkstoffforschung (IFW) Dresden and Dresden University of Technology, Germany. The Raman spectroscopy was performed by Dipl. Chem. Alexander Hoyer at Max Planck Institute at Stuttgart. The MALDI-TOF mass spectra measurements were done with the help of M. Sc. Christian Cervetti and Dr. Stephan Rauschenbach at Max Planck Institute at Stuttgart. The X-ray photoelectron spectroscopy (XPS) on the samples were performed by Dr. Mitssuharu Konuma at Max Planck Institute at Stuttgart. The scanning electron microscopy (SEM) measurement was performed by M. Sc. Kristina Vaklinova at Max Planck Institute at Stuttgart. The high-resolution tunnelling electron microscopy (HRTEM) and energy-dispersive X-ray spectroscopy (EDS) were performed by M. Sc. Nilesh Vats at Max Planck Institute at Stuttgart.

5.1 Introduction

As introduced in previous chapters, SMMs exhibiting unique properties are attractive candidates for potential application in spintronics. Reorganisation of SMMs on surfaces is a key step for practical applications. Along this line, deposition/grafting of SMMs onto suitable substrates, and their connection to nano-electrodes have been undertaken. Carbon-based nanostuctures, such as single-walled carbon nanotubes (SWCNTs)[159], and graphene[160] have been considered as important components in the view of electronics because of their quantum and tunable electronic properties.

A number of different strategies have been proposed to combine SMMs and carbon nanostructures[161]. These mainly focused on two routes: 1) the formation of covalent bonds between SMMs and carbon nanostructures, 2) non-covalent π–π supramolecular interactions between them[93, 106]. Grafting SMMs through covalent methods may introduce electron scattering centres that limit the performance of the final device. In contrast, nonvalent interaction should largely preserve their conductance.

Herein, we report on two SMMs-graphene and SMMs-SWCNTs hybrids created by using molecular evaporation and non-covalent self-assembly approach which allows "the structures to organise themselves into regular patterns or structures by using local forces to find the lowest-energy configuration and to guid this self assembly"[162], respectively.

Towards this aim we chose the *Dy dimer* described in **Chapter 4**, because of its structural robustness and thermal stability up to 200 ^{o}C as well as its good solubleness in organic solvents. A full set of complementary techniques including MALDI-TOF mass spectrometry, high-resolution electron microscopy (HRTEM), X-ray photoelectron spectroscopy (XPS), scanning electronic microscopy (SEM), atomic force microscopy (AFM), Raman spectrometry, and SQUID magnetometry were used to demonstrate the success of the grafting process and the physical properties of the resulting hybrid materials.

5.2 Experimental Section

5.2.1 Preparation and characterisation of Graphene

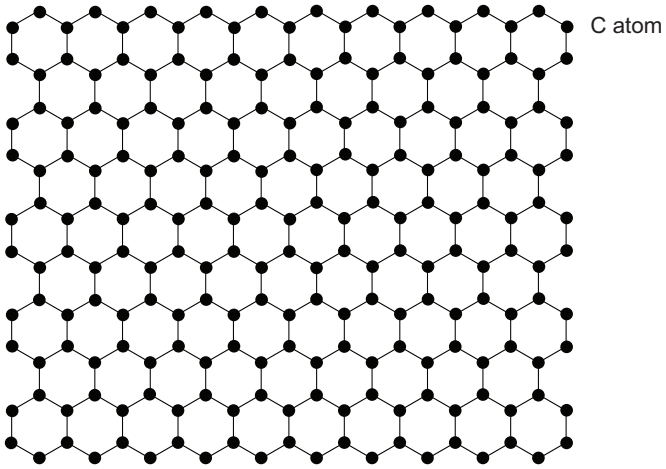

Figure 5.1: Schematic structure of a graphene sheet, a one-atom-thick planar sheet of sp^2-bonded carbon atoms packed in a two-dimensional (2D) honeycomb crystal lattice. Black balls represents the carbon atoms.

Graphene is a one-atom-thick planar sheet of sp^2-bonded carbon atoms packed in a two-dimensional (2D) honeycomb crystal lattice[163] (see Figure 5.1) and is the basic block for carbon materials of other dimensionalities, e.g. fullerenes (0 D), carbon nanotubes (1 D) and graphite (3D)[160]. In the view of spintronics, graphene provides a promising spin channel owing to its long spin-diffusion lengths at room temperature[164–167].

Graphene can be synthesised in various ways, such as micromechanical exfoliation[168], epitaxial growth on SiC[169, 170], chemical reduction of graphite oxide (GO)[171] and chemical vapour deposition (CVD) on metallic substrates[172–174]. However, graphene produced from GO, contains a lot of functional groups and high density of lattice defects. Exfoliated and CVD graphene have fewer defects and exhibit higher conductivity.

In this work, we produced graphene using micromechanical exfoliation of highly oriented pyrolytic graphite (HPOG, Momentive Performance Materials Inc.), firstly proposed in 2004[168]. In this method, graphene is detached from a graphite crystal (e.g. HOPG) using a adhesive tape. After peeling it off, multilayer graphene remains on the tape.

Via repeating peeling the multilayer, graphene is cleaved into thinner flakes of few-layer graphene. Afterwards the graphene is transferred to the substrate (Figure 5.2).

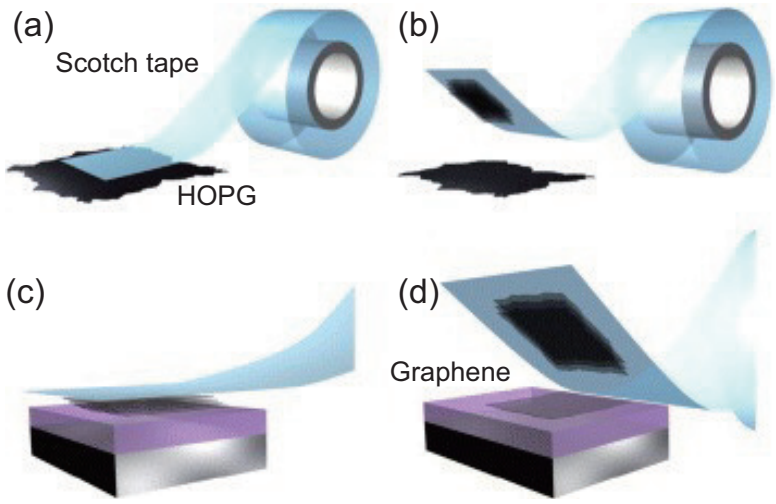

Figure 5.2: Mechanical exfoliation of HOPG. (a) Adhesive tape is pressed against a HOPG crystal so that the top few layers are attached to the tape (b). (c) The tape with multi-layers crystals material is pressed against a surface of choice. (d) Upon peeling off,the bottom layer is left on the substrate. Modified from Ref. [175].

Although graphene is simply prepared as described above, it is not easy to find monolayer graphene on the substrates, because there are also amounts of graphite flakes of various layers produced during the cleavage on the substrates. Therefore, the identification of graphene monolayer is a major hurdle. Research reveals that graphene only becomes visible on Si substrate with a typical 300 nm of SiO_2 capping layer on top because of interference effects[176]. Thus, we chose SiO_2(300 nm)/Si chips as the substrates and the location of graphene can be determined by means of a optical microscopy. Generally, in order to identify graphene of different layers, Raman spectroscopy is often the method of choice, due to its ability to differentiate between monolayer, bilayer and multiplayer graphene[177]. However, mapping with Raman spectroscopy is quite slow[178] and the resolution is limited to around the micro-level (the laser diameter is around 1 μm). Electron microscopy can provide higher resolution analysis, such as SEM, TEM and AFM. Here we adopted AFM technique which is capable of distinguishing layers of graphene, though the correlation between actual and measured thickness is challenging. Because the final measured thickness of graphene can be influenced by adsorbed moisture, electrostatic coupling between AFM tip and graphene as well as the incorrect AFM parameters. Therefore, the obtained thickness of graphene varies between 0.5 nm and 1.5 nm[179], which is larger than what expected from the interlayer graphite spacing (0.35 nm).

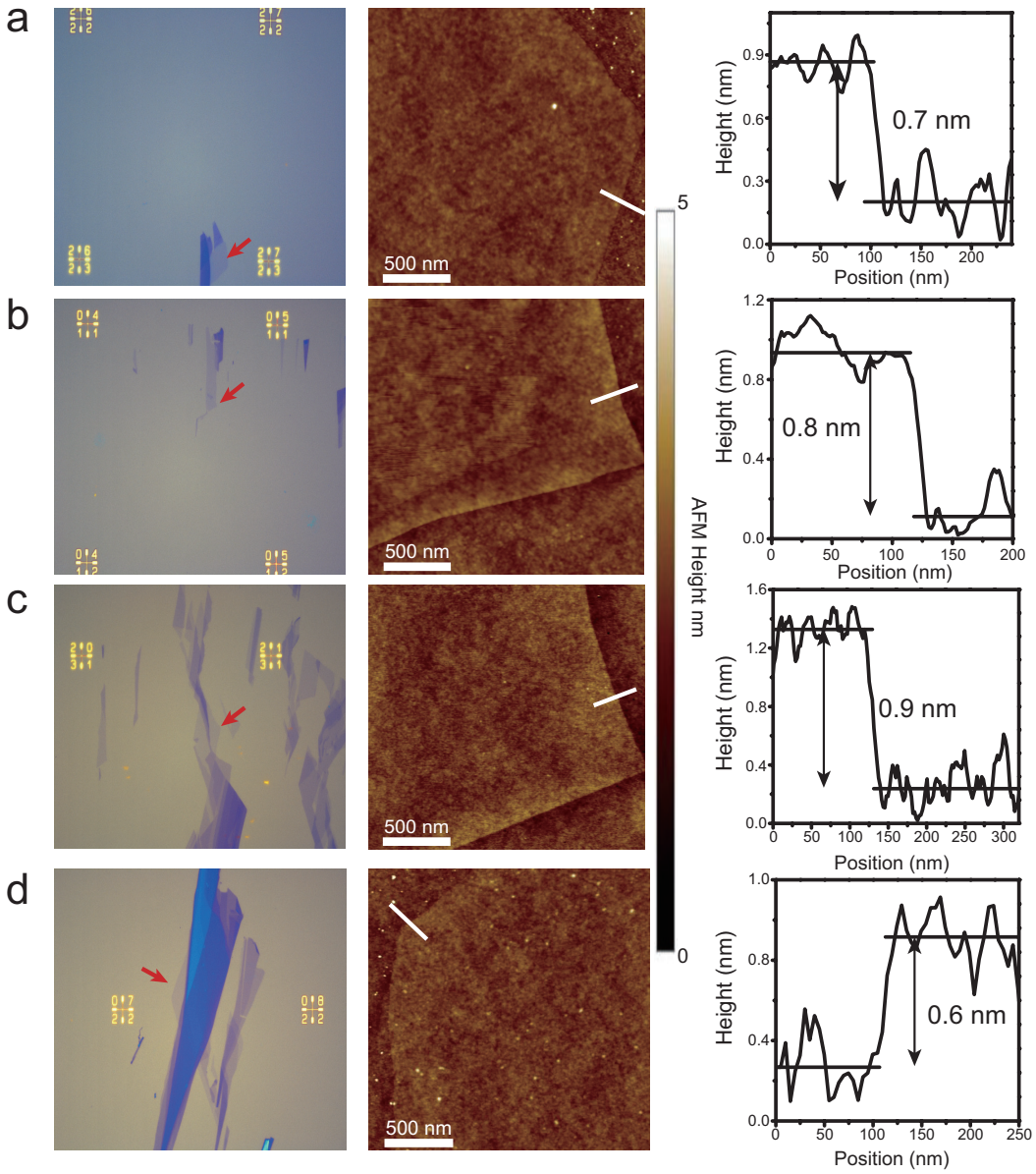

Figure 5.3: Optical hunting and AFM characterisation of micromechanical exfoliated graphene. The left column shows the optical images of graphene on SiO_2 substrate, on which Au marks are used to locate the graphene for following AFM characterisation. The corresponding AFM images of graphene are shown in the middle with the scale bar of 500 nm. The thickness data extracted from the AFM images (middle column) is plotted in the right column, showing the thickness of graphene in the range of 0.6 and 0.9 nm, indicative of monolayer graphene.

In Figure 5.3, optical hunting and AFM characterisation of micromechanical exfoliated graphene are shown. The thickness of graphene sheet is in the range of 0.6 nm and 0.9 nm, indicative of monolayer graphene.

5.2.2 Preparation of SMMs–SWCNTs Hybrids

As mentioned above, 1D single-walled carbon nanotubes (SWCNTs) can be formed by rolling a graphene sheet into a cylinder. The lattice vector (m, n) can be determined by

two basis vectors $\vec{a}_1$ and $\vec{a}_2$ in the graphene plane[180]. The (m, n) indicates the diameter and chirality of tubes. Along different lattice vector (m, n), armchair, zigzag and chiral SWCNTs can be obtained, as shown in Figure 5.4.

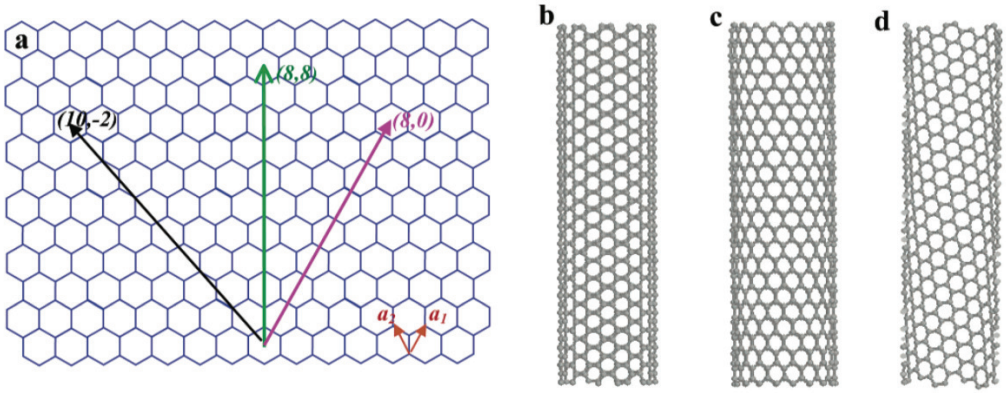

Figure 5.4: a Schematic structure of graphene. SWCNTs can be obtained by rolling a graphene sheet along lattice vectors. $\vec{a}_1$ and $\vec{a}_2$ are two basis vectors. b, c, and d are armchair, zigzag and chiral tubes, along (8,8), (8,0) and (10, -2) vectors, respectively. Reprinted with permission from Ref.[180].

SWCNTs have been synthesised by three main methods, including arc-discharge[181], laser ablation[182] and chemical vapour deposition(CVD)[183]. The first two have common procedure. The solid-state carbon precursors are used as carbon sources for nanotubes growth at thousands of degree Celsius (°C). High-quality and nearly perfect SWCNTs have been obtained by means of these methods. While, CVD makes use of hydrocarbon gases (i.e. CH_4) as carbon atoms sources and metal catalyst as "seeds" to grow SWCNTs at lower temperatures (500 - 1000 °C). The resulting SWCNTs by CVD can be well dispersed in organic solvents.

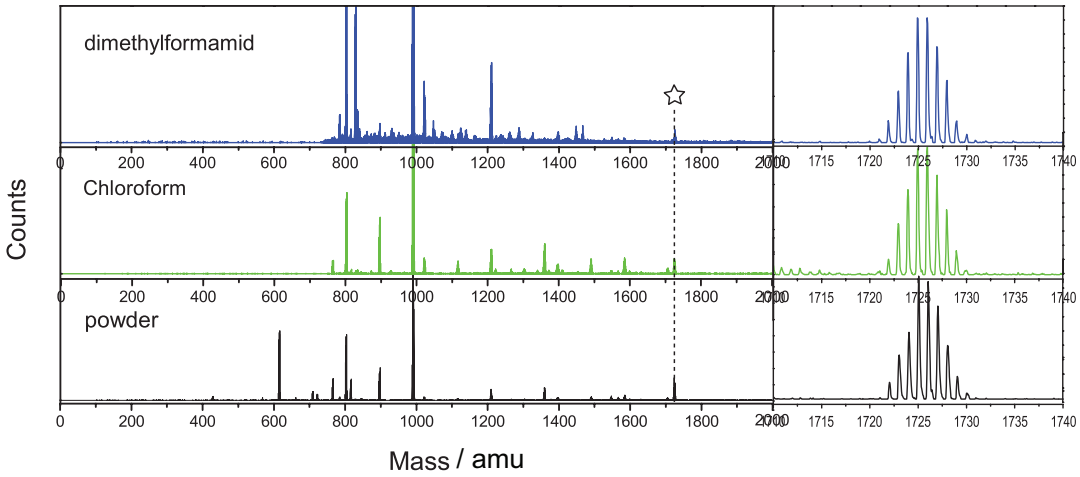

Figure 5.5: Typical negative MALDI-TOF mass spectra of $[Dy(hfac)_3]_2$bpm complex: one dissolved sample in dimithlformaid (top), one sample dissolved in chloroform (middle), and powder sample (bottom) as reference. All measurements were performed under same experimental conditions. The star in column refers to the position of intact molecule at 1725 amu, zoom of which is shown in the right column.

To prepare the hybrids combining SMMs and SWCNTs, we utilised a solution-based deposition in contrast with the previous chapter. *Dy dimer* can be dissoluble in organic solvents such as chloroform and dimitylformamide (DMF). To investigate its structural stability the negative MALDI-TOF mass spectra have been used, Figure 5.5, using powder samples as reference. The peak at 1725 ($\star$) clearly indicate an intact *Dy dimer* molecule, confirming the structural intactness of this magnetic nanosystem, Figure 5.5.

No purify treatment was carried out on SWCNTs to eliminate the catalysts which were employed for growing nanotubes, because normal treatment with inorganic acids i.e. HNO_3, HCl, H_2SO_4, can produce a large amount of defects of tubes, increasing the scattering centres and thus influencing its electronic properties. Moreover, some simple physical treatments, such as electron-beam imaging and AFM can also induce a large number of defects and/or damage the SWCNTs.

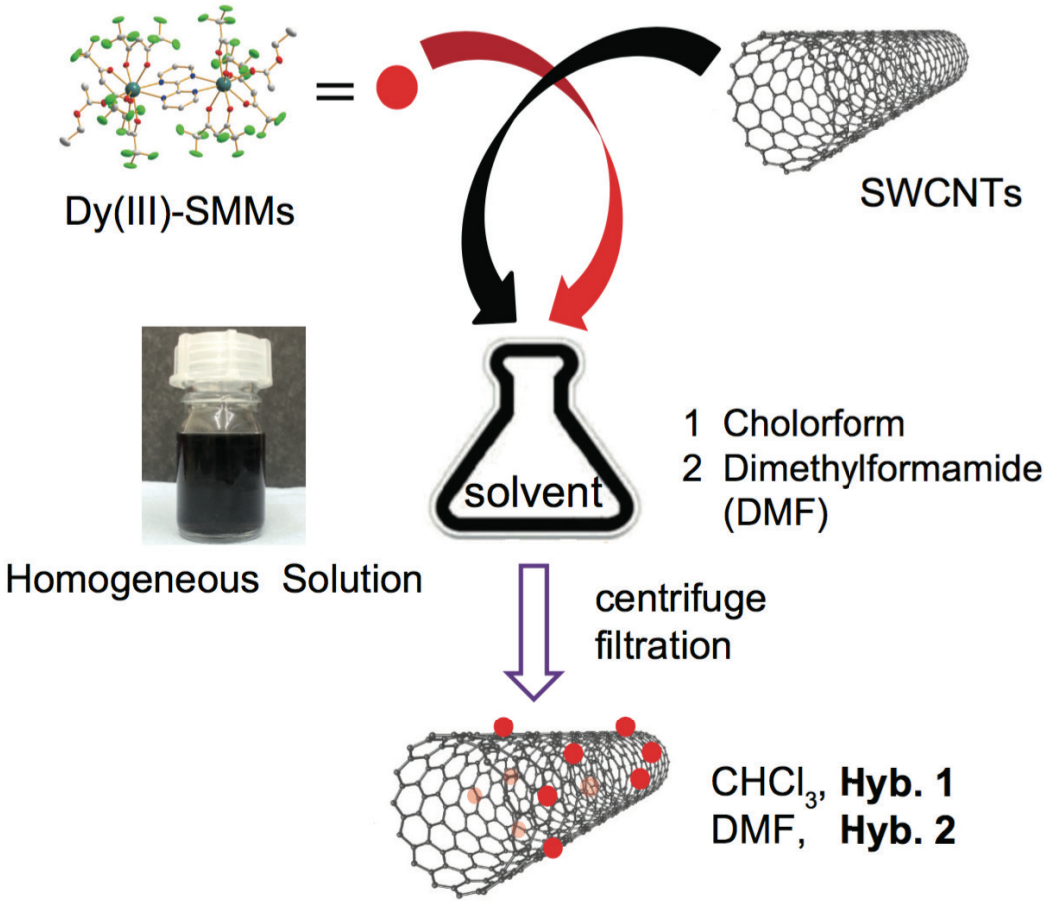

Figure 5.6: The procedure of generating hybrids SMMs-SWCNTs materials in Chloroform and Dimethylformamide (DMF).

The solvents chloroform($CHCl_3$) and dimethylformamide (DMF)[184] were selected for dispersing single-walled carbon nanotubes. The experimental procedure is shown in Figure 5.6. 1.0 mg SWCNTs are dispersed in 20 ml of solvents ($CHCl_3$ or DMF) by means of 24 hours of ultrasonic treatment, generating a dark homogeneous suspension. 5 ml of solvent ($CHCl_3$ or DMF) is used to dissolve 1.11 mg of *Dy dimer*. Then the latter solution was

added into the former one under continuous mechanical stirring and dark homogeneous suspension solution consisting of magnetic molecules and SWCNTs in solvents was then gained with stirring for 20 hours at room temperature, Figure 5.6. Via centrifuge at 1000 rms for 30 min and filtration, the hybrids were obtained in $CHCl_3$ and DMF, namely **Hyb.1** and **Hyb.2**, respectively.

The two hybrids systems were investigated by a full set of complementary techniques, including scanning electron microscopy (SEM), high-resolution tunnelling electron microscopy (HRTEM), energy-dispersive X-ray spectroscopy (EDS), X-ray photoelectron spectroscopy (XPS), and Raman spectrometry, in order to demonstrate the success of grafting SMMs onto SWCNTs. At last, magnetic properties of the hybrids materials were performed on a commercial SQUID magnetometry.

5.3 Results and Discussion

5.3.1 Dy(III)-SMMs on Grephene

As described in **Chapter 4**, this *Dy dimer* shows good structural and electronic integrity upon heating. This constitutes a viable approach to investigating the deposition organisation of SMMs on graphene by sublimation in high vacuum.

The dynamic deposition studied via controlling the evaporation time of *Dy dimer* for 30 s, 60 s, 180 s and 300 s, respectively. Figure 5.7 shows the organisation evolution of SMMs on graphene. Agglomerates of clusters are formed on increasing the evaporation time. Therefore, the organisation of these SMMs on graphene can be well achieved from isolated molecules to films of various thickness for the various measurements, such as electronic transport through individual SMMs.

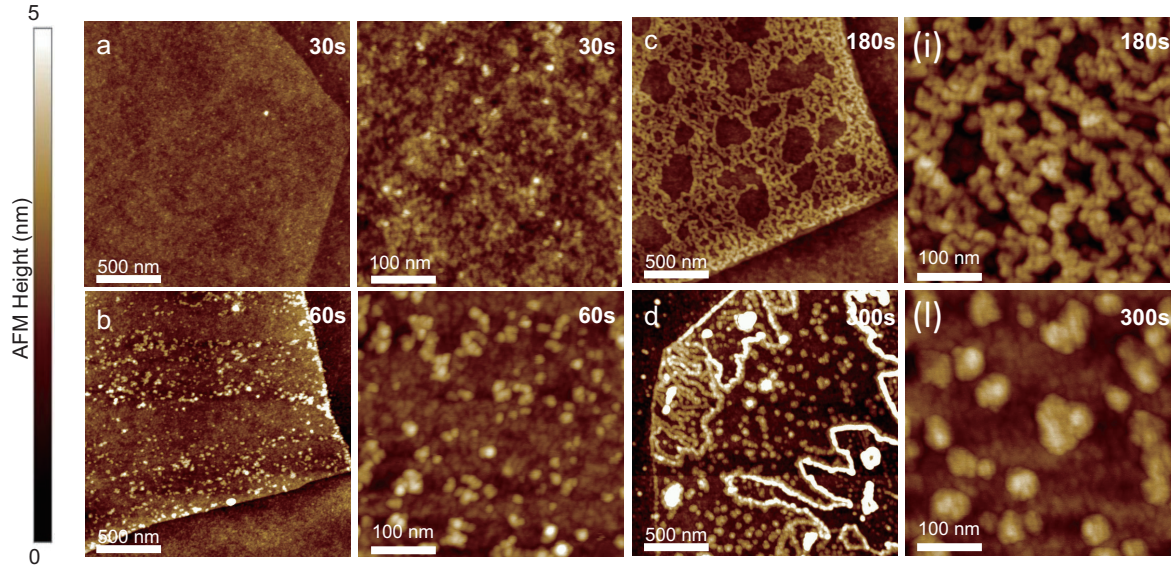

Figure 5.7: Topography comparison of organisation of *Dy dimer* molecules on graphene with deposition time: 30 s, 60 s, 180 s, and 300 s, respectively.

With respect to the techniques traditionally used to study molecules on surfaces, i.e. AFM, and Raman spectroscopy[185] can probe structural and electronic properties of both molecules and graphene in a fast way. The Raman spectra were obtained using a laser excitation of 633 nm (2.31 eV). The corresponding results are shown in Figure 5.8. For all samples, the characteristic G band at ca. 1580 cm^{-1}, caused by the Raman active E_{2g} phonon (in-plane optical mode) and 2D bands at ca. 2700 cm^{-1} were well visible upon the thermally depositing SMMs. Although a slight blue shift of the G band was related to a small charge doping of graphene due to grafting these SMMs, the Raman study show that the electronic properties of graphene sheets remain intact after grafting SMMs in high vacuum. The absence of D band at ca. 1350 cm^{-1}, which is usually associated to disorder, indicated that the integrity of graphene was preserved after the deposition.

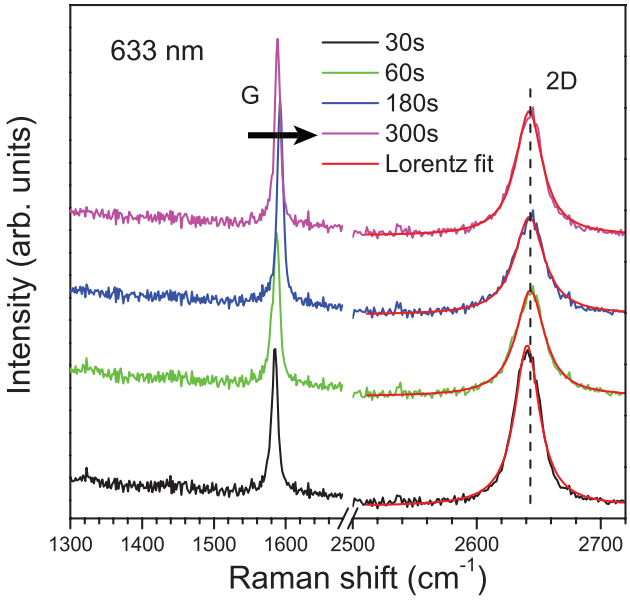

Figure 5.8: Raman spectra acquired from *Dy dimer* molecules deposited on graphene with different evaporation time: 30 s, 60 s, 180 s and 300 s. The G and 2D modes of graphene are indicated. Red solid curves show Lorentzian fitting peaks.This Raman spectroscopy measurement was performed by Dipl. Chem. Alexander Hoyer at Max Planck Institute at Stuttgart.

5.3.2 Dy(III)-SMMs onto SWCNTs

The case of Hyb.1

Scanning Electron Microscopy (SEM) and XPS analysis. SEM experiment were performed on **Hyb.1** specimens, which were prepared by freshly dropping the bulk hybrids materials on one SiO_2 substrate. The sample gives rise to bundles accompanied with a significant amount of round-like particles on top (Figure 5.9). Because the SEM setup we employed is not equipped with energy-dispersive X-ray spectroscopy (EDS) part, we performed XPS spectroscopy on the same sample, since XPS measurement can provide direct evidence for all the expected elements. The result reveals the strong signals of dysprosium from the hybrids (see Figure 5.10).

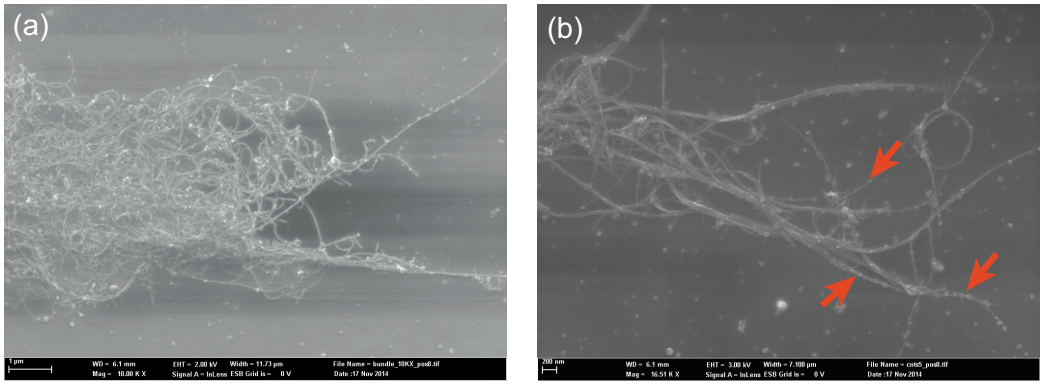

Figure 5.9: Two representative SEM images of **Hyb.1** on one SiO_2 substrate, showing round-like particles staying onto the SWCNTs. (a) The scale bar is 1 μm; (b) The scale bar is 200 nm. Performed by M. Sc. Kristina Vaklinova at Max Planck Institute at Stuttgart.

Figure 5.10 shows high resolution XPS spectra of Dy $3d$ of **Hyb.1** and powder reference. In this image, Dy $3d$ is characterised by a double peak, namely Dy $3d_{3/2}$ and Dy $3d_{5/2}$, at the binding energy of ca. 1296.0 and ca. 1333.4 eV due to the spin-orbit splitting. The energy difference between the two investigated peaks is determined to be ΔE= E(Dy $3d_{3/2}$) - E(Dy $3d_{5/2}$) of 37.4 eV. Furthermore, the Dy $3d_{5/2}$ level is accompanied by a less intense satellite peak at higher binding energies (ca. 1299.5 eV), in excellent agreement with that observed in the case of *Dy dimer* deposited on SiO_2 substrates (see **Chapter 4**).

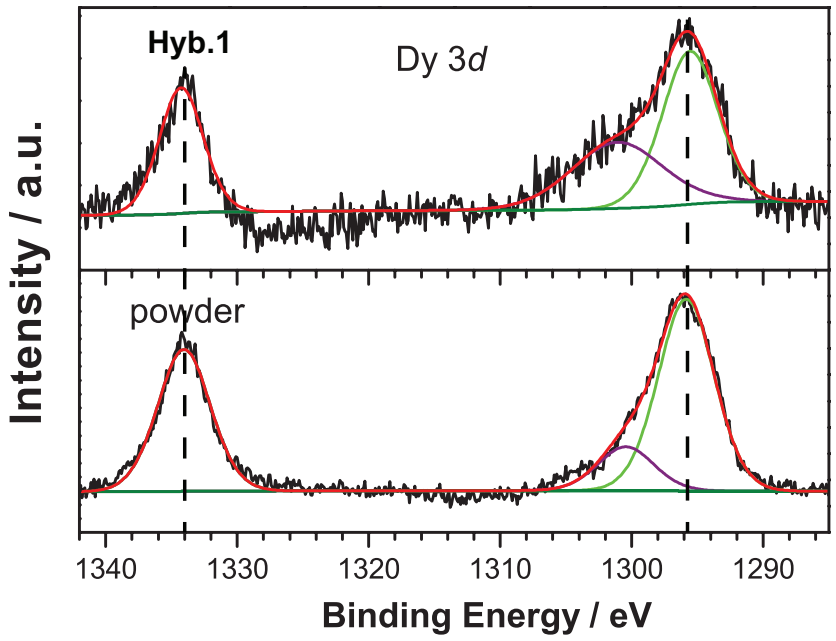

Figure 5.10: High resolution XPS spectra of Dy $3d$ of **Hyb.1** and powder reference. Both XPS spectra were calibrated with the energy of C $1s$ core level at 284.80 eV. This X-ray photoelectron spectroscopy (XPS) measurement was performed by Dr. Mitssuharu Konuma at Max Planck Institute at Stuttgart.

These results obtained from combined MALDI-TOF mass spectroscopy, SEM images

and XPS spectra of **Hyb.1**, strongly evidence that Dy(III)-SMMs molecules remain intact not only structurally, but also electronically. Therefore grafting this magnetic molecule onto SWCNTs was successful. However, the questions what interaction is between *Dy dimer* and SWCNTs and what magnetic behaviour of this hybrids, still need to be answered.

Raman spectroscopy was used to investigate **Hyb.1**. The sample prepared on SiO_2 substrate was excited by the continuous wave second harmonic of an Nd:YAG laser at 2.31 eV (633 nm). All Raman measurements were carried out under the same conditions for all samples to maintain high uniformity of the intensity. Figure 5.11 compares the Raman spectra for **Hyb.1** and pure SWCNTs, both showing the presence of most prominent Raman features: Radial Breathing Mode (RBM) mode (100 - 300 cm^{-1}) and G band (1582 cm^{-1}).

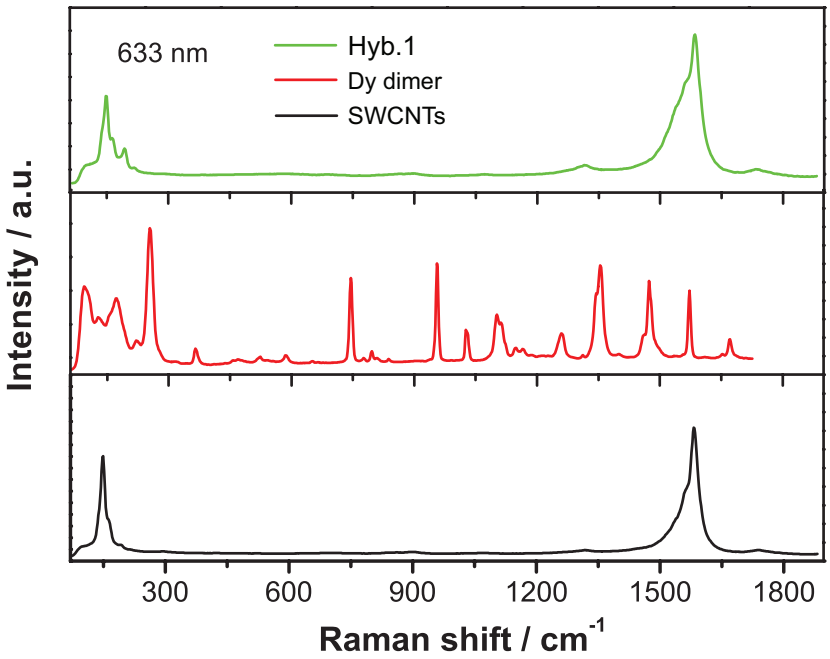

Figure 5.11: Typical Raman spectra of **Hyb.1** deposited on one SiO_2 substrate (top), powder (middle), and dispersed pure SWCNTs in $CHCl_3$ (bottom), under irradiation at 633 nm. Radial Breathing Mode (RBM) peaks that are characteristic of SWCNTs are clearly observed at 100 - 300 cm^{-1}. This Raman spectroscopy measurement was performed by Dipl. Chem. Alexander Hoyer at Max Planck Institute at Stuttgart.

Compared with that for pure SWCNTs, no distinct difference in Raman spectra for **Hyb.1** is observational, after grafting magnetic molecules on SWCNTs. The effect of *Dy dimer* on SWNTs is quite week or neglectful, and it seems simply physical adsorption behaviour of SMMs.

Magnetic properties. The effects of the magnetic molecule grafted on SWCNTs become visible when a magnetic field is applied. Static and dynamic magnetic susceptibilities of pure SWCNTs and **Hyb.1** were measured by means of SQUID magnetometry.

Static magnetic properties of the pure SWCNTs and **Hyb.1** were carried out by investigating the magnetism vs. magnetic field at 1.8 K (see Figure 5.12). The preparation

of hybrids in solvents did not allow us to quantitatively estimate the percentage of the dinuclear Dy(III)-based SMMs present in the hybrids. Therefore, we plot the original magnetic in the unit of emu. Pure SWCNTs exhibit a diamagnetic response, although possessing few metal catalyst nanoparticles. The addition of *Dy dimer* is clearly observed by an increase in the magnetic response of the hybrid material with nonsaturation values of 4.77×10^{-3} emu at 7 T. The appearance of a paramagnetic responses supports the presence of magnetic molecules in hybrid materials in the indirect way.

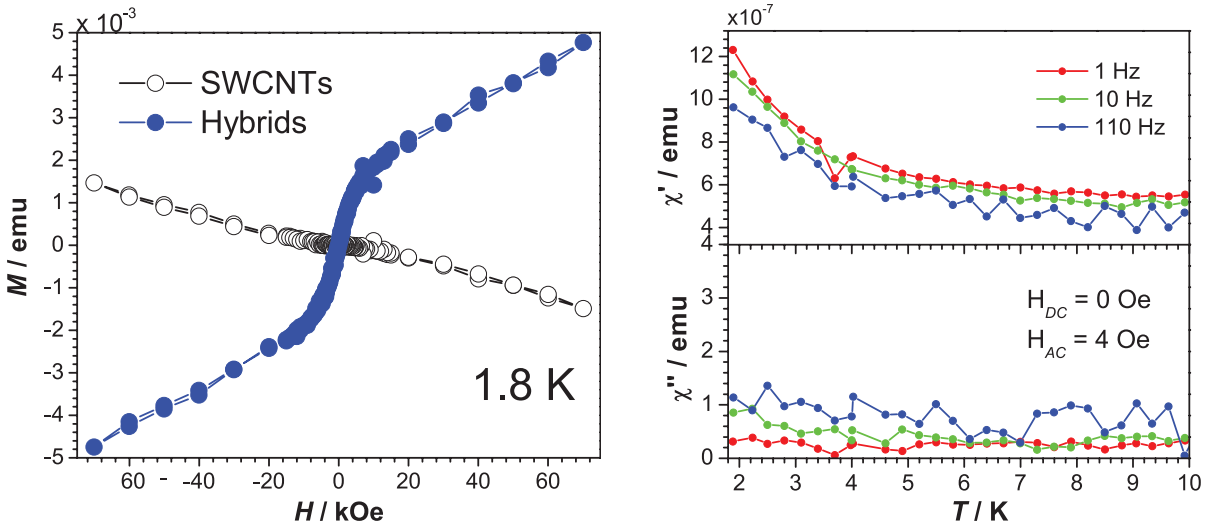

Figure 5.12: (left) Isothermal field dependence of the magnetisation (M) of **Hyb.1** (blue) and pure SWCNTs (black)at 1.8 K. (right) Temperature dependence of ac susceptibility of **Hyb.1** collected at 1 Hz, 10 Hz, and 110 Hz, respectively, under zero dc field and and 4 Oe ac field. The temperature range is between 1.8 and 20 K. Solid lines are a guide to the eye.

AC dynamic magnetic measurements were carried out under an zero static field and 4 Oe AC field, shown in Figure 5.12 right. Since pure SWCNTs exhibit diamagnetic, no ac susceptibility measurements were performed. No distinct out-of-phase signal was detected for the hybrids at the explored temperature between 1.8 and 20 K. This could be attributed to the small amount of *Dy dimer* SMMs adsorbed onto the sidewalls of nanotubes, which generates a weak signal of the order of 10^{-7}.

The case of Hyb.2

Electron microscopy and XPS analysis. HRTEM image of SWCNTs dispersed in DMF shows the presence of bundles of nanotubes (see Figure 5.13a), accompanied by a significant number of dark spots associated with the particles of the metal catalysts employed in their synthesis. The corresponding EDX spectroscopy (Figure 5.13b) confirms the Pt and Rh elements, as expected used catalysts. Nevertheless, no magnetic response of the catalysts was observed during magnetic measurements.

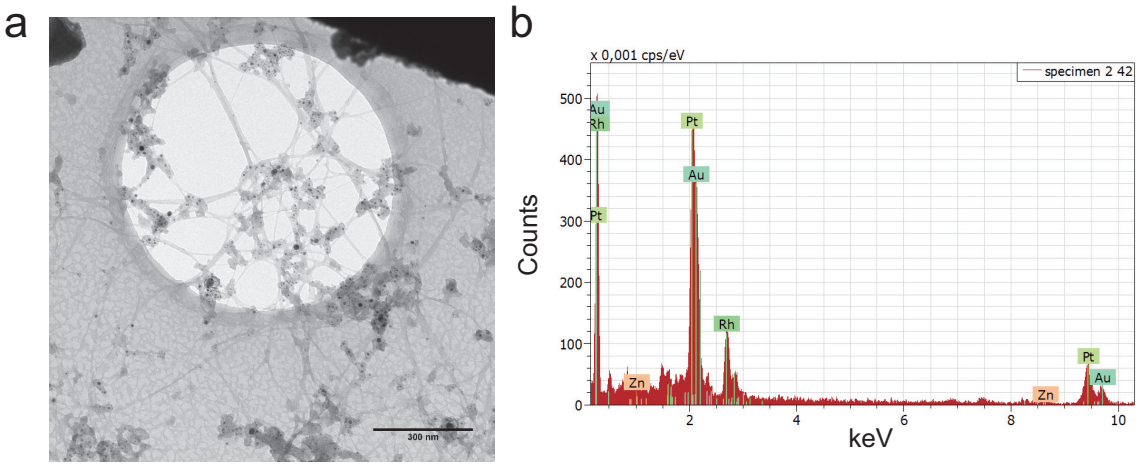

Figure 5.13: a. HRTEM image of SWCNTs dispersed in DMF. The black dots are metallic catalysts particles. The gold signals are from the grids for holding the sample; b. EDX spectrum of SWCNTs, indicative of the main elements of catalysts, Rh and Pt. Performed by M. Sc. Nilesh Vats at Max Planck Institute at Stuttgart.

A close look at **Hyb.2** obtained from grafting *Dy dimer*, reveals significant differences with respect to the pure SWCNTs, Figure 5.14. It can be found that amounts of dark spots staying on SWCNTs surfaces. In addition, EDX measurement indicates the presence of element dysprosium at higher energy (ca. 1300 keV), Figure 5.14b.

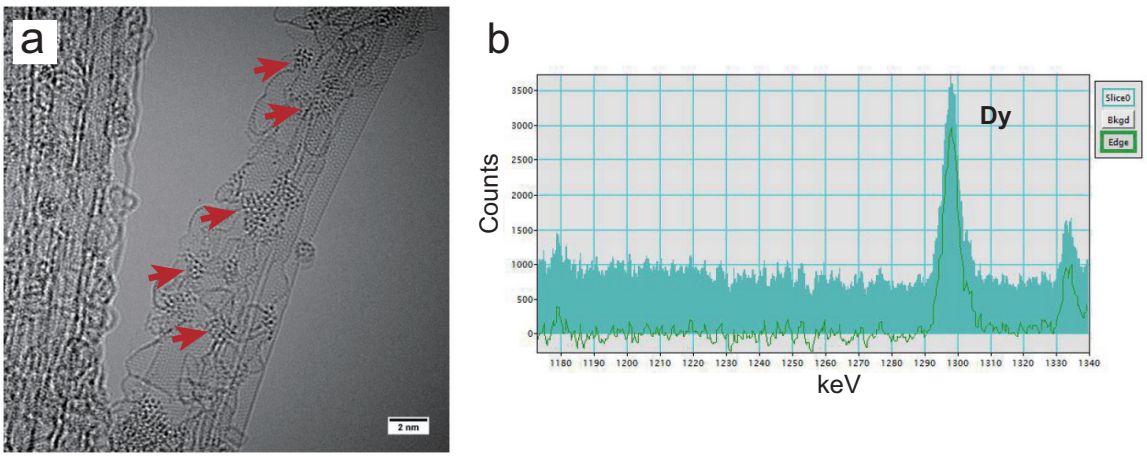

Figure 5.14: a. HRTEM image of **2** (scale bar: 2 nm), accompanied with clusters-like particles (see red arrows) staying on SWCNTs surface; b. EDX spectrum acquired from a decorated SWCNT like the one shown in a, which confirms the presence of element dysprosium. Performed by M. Sc. Nilesh Vats at Max Planck Institute at Stuttgart.

Figure 5.15 shows high resolution XPS spectra of Dy $3d$ of **Hyb.2** and powder reference. Dy $3d$ has a double peak, namely Dy $3d_{3/2}$ and Dy $3d_{5/2}$, at the binding energy of ca. 1296.0 and ca. 1333.4 eV due to the spin-orbit splitting. Furthermore, the Dy $3d_{5/2}$ level is accompanied by a less intense satellite peak at higher binding energies (ca. 1299.5 eV), in good agreement with that observed in the case of **Hyb.1** and *Dy dimer* deposited on SiO_2 substrates (see **Chapter 4**).

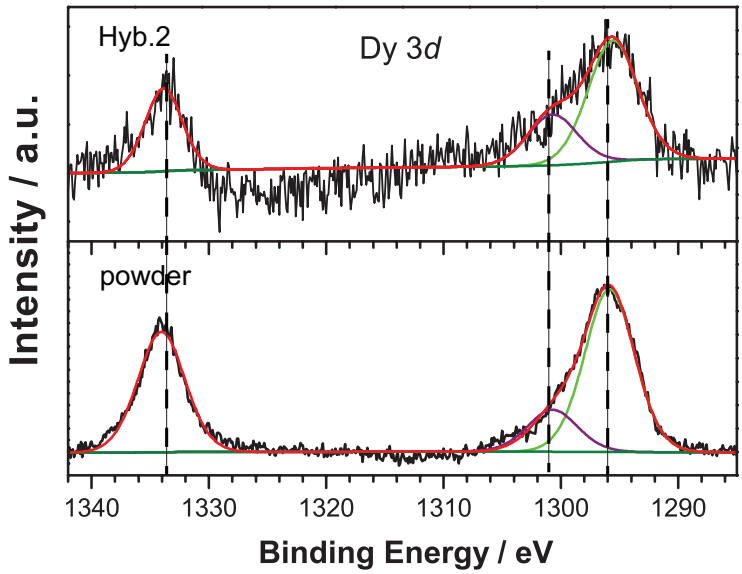

Figure 5.15: High resolution XPS spectra of Dy 3*d* of **Hyb.2** (top) and powder reference (bottom). Both XPS spectra were calibrated with the energy of C 1s cole level at 284.80 eV. This X-ray photoelectron spectroscopy (XPS) measurement was performed by Dr. Mitssuharu Konuma at Max Planck Institute at Stuttgart.

Magnetic properties. Static and dynamic magnetic measurements were also performed on **Hyb.2** and the corresponding results are given in Figure 5.16. Different from diamagnetic behaviour for pure SWCNTs at 1.8 K, **Hyb.2** shows paramagnetic behaviour (Figure 5.16). A saturation value of 2.64 $\times$ 10^{-3} emu at 7 T is obtained. This behaviour change can be attributed to importing *Dy dimer* in this case.

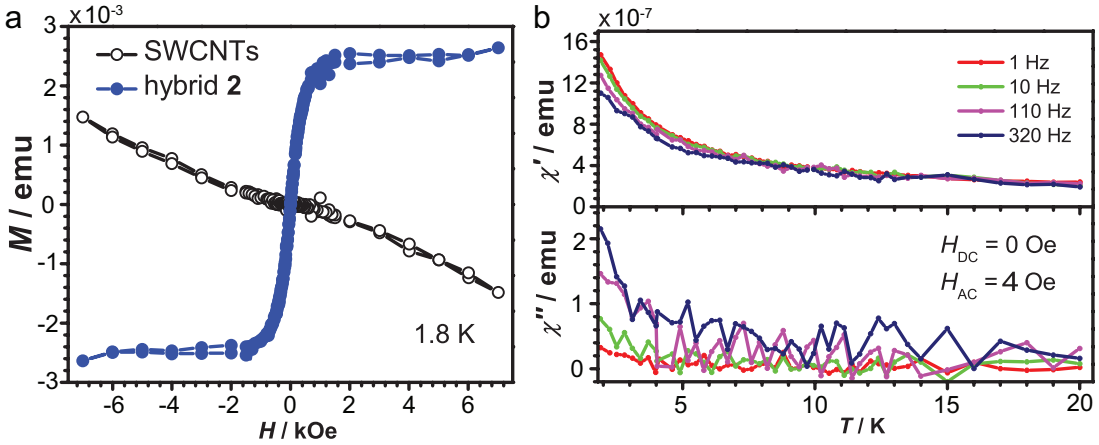

Figure 5.16: a. Isothermal magnetic field dependence of the magnetisation (M) of **Hyb.2** at 1.8 K. b. Temperature dependence of AC susceptibility of **Hyb.2** collected at 1 Hz, 3.2 Hz, 10 Hz, 110 Hz, and 320 Hz, respectively, under zero static field and 4 Oe AC field. The temperature range is between 1.8 and 20 K. Solid lines are a guide to the eye.

AC dynamic magnetic susceptibility measurements were carried out under an zero DC field and 4 Oe AC magnetic field, as shown in Figure 5.16. Still no distinct out-of-phase χ'' signals was detected for **Hyb.2** owing to a small amount of Dy(III)-SMMs grafted

onto nanotubes, which generates a weak signal of the order of 10^{-7}. However, at lower temperature below ca. 4 K, an exponential increase in both χ' and χ'' signals are present, which is the typical behaviour or lanthanide-based SMMs. It is worthy to mention that the position of the susceptibility tails seems to be frequency dependent, as expected for a dynamic relaxation process. These features provides the support for the presence of Dy(III)-based SMMs in the hybrid material.

6 Summary and Outlook

Summary

This thesis contains the contents from rational synthesis of lanthanide based SMMs, to grafting them onto various surfaces. The main summary of this thesis is presented in two parts.

In the first part, we demonstrate stepwise synthesis of Dy(III)-based SMMs of increasing nuclearity via a modular LEGO-like approach. Then, research on solvent molecule substitution effect on magnetisation dynamics of a series of dinuclear Dy(III)-based SMMs was investigated.

According to the modular LEGO-like approach, we assemble in a stepwise way the fundamental building blocks to produce a SMM with desired magnetic properties. Using Dy(III) ions as magnetic blocks, $hfac^-$ ligands as bulky shielding blocks and bidentate or tridentate ligands as linkers, we have synthesised a series of mononulcear and polynuclear Dy(III)-based SMMs, namely $Dy(hfac)_3bpy$ (bpy = 2,2′-bipyridine), **1**; $Dy(hfac)_3$tBu-bpy (tBu-bpy = 4,4′-di-tert-butyl-2,2′-bipyridine), **2**; $[Dy(hfac)_3(EtOAc)]_2bpm$ (EtOAc = ethyl acetate), **3** and $[Dy(hfac)_3]_3HAT$ (HAT = 1,4,5,8,9,12-hexaazatriphenylene), **4**. Among them, only compound **3** exhibits distinct SMMs behaviour under zero DC field confirmed by frequency-dependent AC susceptibilities. Quantum tunnelling of the magnetisation for all compounds was suppressed by an optimised external field of 4 kOe, and frequency-dependent AC susceptibilities for all were observed, confirming SMMs behaviour. The biggest effective energy barrier to reverse the spin is obtained for **4** with the value of 84 K. The static magnetic properties demonstrate the role of the linking groups in introducing intramolecular interactions that can be tuned. Dynamic susceptibility measurements for **1** to **4** show an exceptionally tuning of the dynamic properties, where under-barrier process can be suppressed and high values can be obtained by rational design.

Flexibility of supramolecular chemistry and a magnetic LEGO system would allow providing one coordination position of Dy(III) ions, which can be occupied by one additional solvent molecule, to achieve fine-tuning the local geometry around Dy(III) ion. Therefore, we enabled synthesising a series of neutral dinuclear Dy(III) ions containing complexes sharing the general formula $[Dy(hfac)_3R]_2bpm$, in which R = nothing (**5**), water (H_2O, **6**), ethyl acetate (EA, **3**), and methyl propionate (MP, **7**). Mydosh′s law and frequency-dependent imaginary χ'' components of AC susceptibility evidence that all complexes possess SMMs behaviour. The effective electrostatic model analysis reveals that magnetic easy axis lie in the plane formed by the opposite $hfac^-$ ligands due to these two

β-diketonate ligands with four large charged oxygen atoms lowering the potential energy compared with the bpm, solvent molecule and the last $hfac^-$ ligand. Furthermore, orientation of the magnetic moments is approximately perpendicular to the vector connecting the two dysprosium(III) ions, indicating the antiferromagnetic coupling.

In the second part, we investigated Dy(III)-based SMMs by means of SQUID magnetometry to identify whether they retain their molecular magnetic properties when deposited on different surfaces.

We have studied the dysprosium(III) dimer (**3**) SMMs deposited on SiO_2 surfaces and on graphene. The deposition of intact magnetic molecules was achieved by using molecular evaporation, and this allowed detailed AFM imaging of the molecules from quasi-monolayer to thick layers. Compared with magnetic measurements results for powder samples, dysprosium(III)-dimers on surfaces remain magnetically intact.

A similar experimental strategy was employed to study the morphology of Dy(III) dimer (**3**) on graphene surfaces. AFM imaging of molecular nanomagents on graphene showed individually addressable molecules and aggregates, presumably since the molecules were only weakly interact to graphene.

Different from molecular evaporation, self-assembly enables decorating magnetic molecules onto sidewalls of SWCNTs, thus generating the hybrid SMMs-SWCNTs systems. Solubleness of the Dy(III) dimer (**3**) in $CHCl_3$ and DMF enables generation of two hybrids systems, namely **Hyb. 1** and **Hyb. 2**, respectively. SEM and HRTEM imaging of **Hyb. 1** and **Hyb. 2** directly show nanoscale particles were decorated onto SWCNTs surfaces. XPS spectra and EDS spectra confirm the presence of Dy(III) element in both systems. Low temperature magnetic response for these two hybrid materials is similar to that found for powder samples, providing additional support for grafting success.

Outlook

The story described before of compound **3** including the successful synthesis, thermally deposition on various surfaces and preserving magnetic properties as films, enables providing a possibility of investigating intrinsic properties of these magnetic nano-systems. The successful combination of SMMs with SWCNTs and graphene may open new perspectives in the field of molecular spintronics, where it is possible to investigate the synergy between electron transport and magnetism at the molecular level. Molecular spintronics devices based on carbon nanostructres may benefit from understanding how reorganisation of magnetic molecules on graphene and SWCNTs ahead of fabrication of nano devices.

It comes real by collaborating with M. Sc. Chit Siong Aaron Lau, Dr. Junjie Liu and Dr. Jan Mol in Oxford University, England, who fabricate the CVD graphene-based nano-gap devices and are able to measure electronic transport properties at cryogenic temperatures (down to 20 mK).

The fabrication process of CVD graphene nano-gaps[186] is shown in Figure 6.1. The fabrication strategy comprises a lithography process and a feedback-controlled electroburning process, generating the gap of size of 1 – 2 nm and the fabrication details can be found in the Ref.[186].

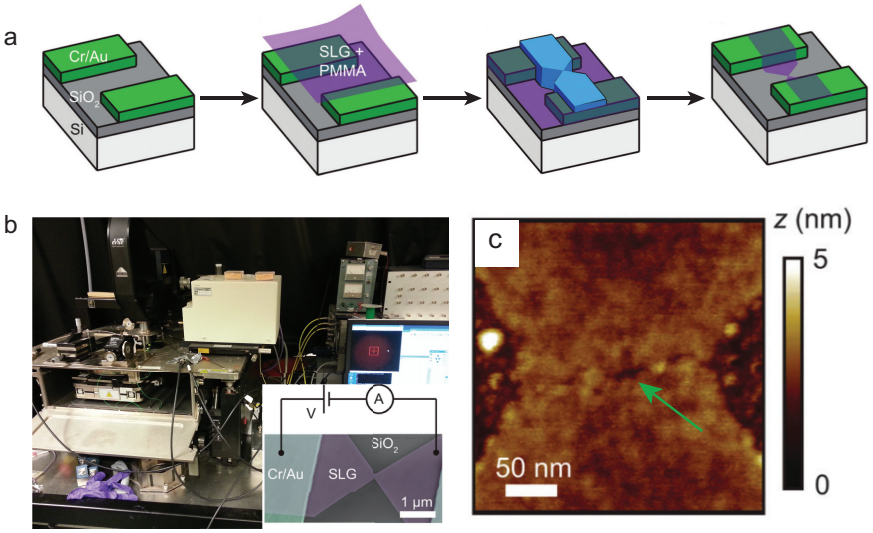

Figure 6.1: a. Schematics for the fabrication process of graphene nano-gap device. b. Feedback-controlled electroburning system for recording current-voltage. c. AFM image of a typical graphene nanogap (green arrow) after the electroburning process. Reprinted with permission from Ref. [186].

To avoid the external impurity and to keep the cleanness of the nano-gaps devices, we adopted molecular evaporation approach in high vacuum described in **Chapter 4**, to achieve the goal of depositing SMMs into the nano-gaps. Morphology of graphene nano-gaps before and after molecular evaporation is investigated by AFM, as shown in Figure 6.2. The molecules (compound **3**) appear to form densely packed islands of approximately spherical objects, consistent with those found on graphene in **Chapter 5**.

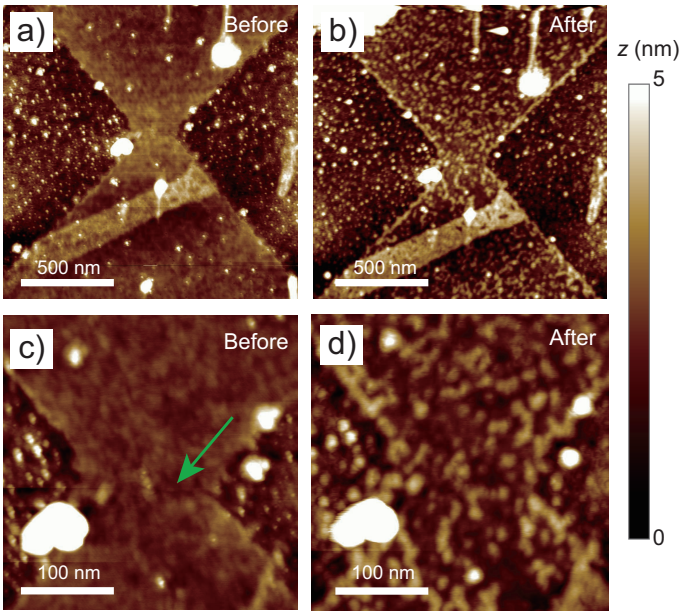

Figure 6.2: Comparison on AFM images acquired for compound **3** sublimated into graphene nano-gaps at 150 ^{o}C before and after molecular evaporation.

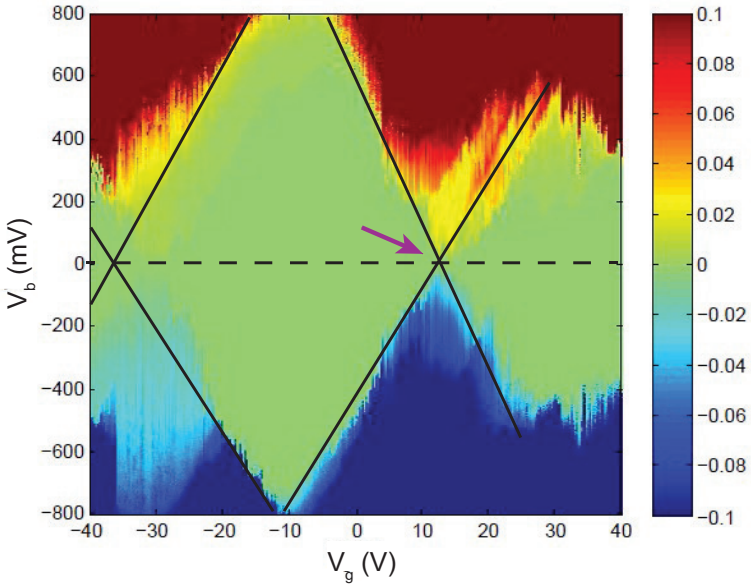

Figure 6.3: (Unpublished results) Schematic $\mathrm{d}I/\mathrm{d}V$ color plot as a function of the bias voltage V_{bias} and the gate voltage V_{gate} at $B = 0$ T at 20 mK. These measurements were performed by Chit Siong Aaron Lau, Dr. Junjie Liu and Dr. Jan Mol from University of Oxford, England.

The graphene nano-gaps involving magnetic molecules were measured in zero magnetic field B = 0 T and at 20 mK. A typical resulting stability diagram of is shown in Figure 6.3. Two low-conductance regions on either side of the degeneracy point at gate voltage V_{gate} = ca. 11 V (indicated by a purple arrow). To make sure this behaviour completely from the **3** molecule itself, we designed the comparison experiments, including 1) $\mathbf{Y}_2$ graphene junctions. Substituting Dy(III) ions with yttrium(III) ions affords the isostructural complex [Y(hfac)$_3$(EtOAc)]$_2$bpm ($\mathbf{Y}_2$), which can also be thermally evaporated due

to hfac ligands. Following the same molecular evaporation procedure for compound **3**, the $\mathbf{Y}_2$ graphene junctions were obtained. 2) graphene nanogaps. 3) graphene nanogaps with compound **3**. The constant field rotation measurements have been performed on graphene quantum dot (QD) and $\mathbf{Y}_2$ junctions at $T = 20$ mK, respectively (see figure 6.4). Coulomb peaks from the graphene nanogaps and $\mathbf{Y}_2$ graphene junctions were not observed by rotating the field. And it can be clearly found the presence of Coulomb peaks from Dy_2 junctions. Therefore, the electron transport properties belong to *Dy dimer*, not from graphene nano-gaps itself or the diamagnetic molecules.

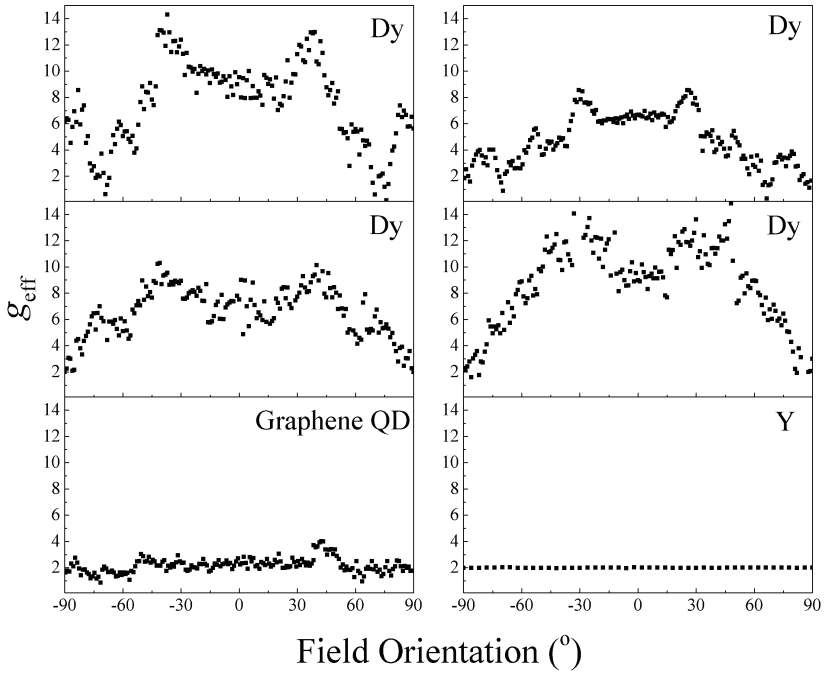

Figure 6.4: (Unpublished results) Comparison of Coulomb peaks between Dy_2 junctions, graphene QD and $\mathbf{Y}_2$ junctions at the constant field $B = 1$ T and T = 20 mK. The rotation angle is between -90° and 90°. This measurements were performed by Chit Siong Aaron Lau, Dr. Junjie Liu and Dr. Jan Mol from University of Oxford, England.

The whole experimental measurement is still running in Oxford, England, so here we just show what we obtained so far. When all the measurements are done, the intrinsic properties of this complex will be fully understood.

References

[1] A. Caneschi, D. Gatteschi, and R. Sessoli. Alternating current susceptibility, high field magnetisation, and millimeter band EPR evidence for a ground $S = 10$ state in $[Mn_{12}O_{12}(CH_3COO)_{16}(H_2O)_4]_2CH_3COOH{\cdot}4H_2O$. *J. Am. Chem. Soc.*, 113:5873–5874, 1991.

[2] L. Thomas, F. Lionti, R. Ballou, D. Gatteschi, R. Sessoli, and B. Barbara. Macroscopic quantum tunnelling of magnetization in a single crystal of nanomagnets. *Nature*, 383:145–147, 1996.

[3] W. Wernsdorfer and R. Sessoli. Quantum phase interference and parity effects in magnetic molecular clusters. *Science*, 284:133–135, 1999.

[4] D. Gatteschi and R. Sessoli. Quantum tunneling of magnetization and related phenomena in molecular materials. *Angew. Chem. -Int. Edit.*, 42:268–297, 2003.

[5] M. Mannini, F. Pineider, P. Sainctavit, C. Danieli, E. Otero, C. Sciancalepore, A. Talarico, M. Arrio, A. Cornia, D. Gatteschi, and R. Sessoli. Magnetic memory of a single-molecule quantum magnet wired to a gold surface. *Nature Mater.*, 8:194–197, 2009.

[6] M. Cavallini, J. Gomez-Segura, D. Ruiz-Molina, M. Massi, C. Albonetti, C. Rovira, J. Veciana, and F. Biscarini. Magnetic information storage on polymers by using patterned single-molecule magnets. *Angew. Chem. -Int. Edit.*, 44:888–892, 2005.

[7] A. Ardavan, O. Rival, J. Morton, S. Blundell, A. Tyryshkin, G. Timco, and R. Winpenny. Will spin-relaxation times in molecular magnets permit quantum information processing? *Phys. Rev. Lett.*, 98:057201, 2007.

[8] L. Bogani and W. Wernsdorfer. Molecular spintronics using single-molecule magnets. *Nat. Mater.*, 7:179–186, 2008.

[9] A. Rocha, V. García-Suárez, S. Bailey, C. Lambert, J. Ferrer, and S. Sanvito. Towards molecular spintronics. *Nature Mater.*, 4:335–339, 2005.

[10] S. Jiang, B. Wang, G. Su, Z. Wang, and S. Gao. A mononuclear dysprosium complex featuring single-molecule-magnet behavior. *Angew. Chem. -Int. Edit.*, 49:7448–7451, 2010.

[11] A. Mishra, W. Wernsdorfer, S. Parsons, G. Christou, and E. Brechin. The search for 3d-4f single-molecule magnets: synthesis, structure and magnetic properties of a $[Mn^{(III)}{}_2Dy^{(III)}{}_2]$ cluster. *Chem. Commun.*, 16:2086–2088, 2005.

[12] L. Toma, R. Lescouëzec, J. Pasán, C. Ruiz-Pérez, J. Vaissermann, J. Cano, R. Carrasco, W. Wernsdorfer, F. Lloret, and M. Julve. $[Fe(bpym)(CN)_4]^-$: A new building block for designing single-chain magnets. *J. Am. Chem. Soc.*, 128:7974–7956, 2006.

[13] P. Lin, T. Burchell, R. Clérac, and M. Murugesu. Dinuclear dysprosium(III) single-molecule magnets with a large anisotropic barrier. *Angew. Chem. -Int. Edit.*, 47:8848–8851, 2008.

[14] K. Bernot, J. Luzon, L. Bogani, M. Etienne, C. Sangregorio, M. Shanmugam, A. Caneschi, R. Sessoli, and D. Gatteschi. Magnetic anisotropy of dysprosium(III) in a low-symmetry environment: a theoretical and experimental investigation. *J. Am. Chem. Soc.*, 131:5573–5579, 2009.

[15] W. Huang, J. Le Roy, S. Khan, L. Ungur, M. Murugesu, and P. Diaconescu. Tetraanionic biphenyl lanthanide complexes as single-molecule magnets. *Inorg. Chem.*, 54:2374–2382, 2015.

[16] J. Luzon and R. Sessoli. Lanthanides in molecular magnetism: so fascinating, so challenging. *Dalton Trans.*, 41:13556–13557, 2012.

[17] S. Liddle and J. van Slageren. Improving f-element single molecule magnets. *Chem. Soc. Rev.*, 44:6655–6669, 2015.

[18] C. Benelli and D. Gatteschi. Magnetism of lanthanides in molecular materials with transition-metal ions and organic radicals. *Chem. Rev.*, 102:2369–2387, 2002.

[19] C. Zaleski, E. Depperman, J. Kampf, M. Kirk, and V. Pecoraro. Synthesis, structure, and magnetic properties of a large lanthanidetransition-metal single-molecule magnet. *Angew. Chem. -Int. Edit.*, 116:4002–4004, 2004.

[20] S. Osa, T. Kido, N. Matsumoto, N. Re, and A. Pochaba. A Tetranuclear 3d-4f Single Molecule Magnet: $[Cu^{II}LTb^{III}(hfac)_2]_2$. *J. Am. Chem. Soc.*, 126:420–421, 2004.

[21] G. Aromi and E. Brechin. Synthesis of 3d metallic single-molecule magnets. *Sturc. Bond*, 122:1–69, 2006.

[22] L. Sorace, C. Benelli, and D. Gatteschi. Lanthanides in molecular magnetism: old tools in a new field. *Chem. Soc. Rev.*, 40:3092–3104, 2011.

[23] L. Westin, M. Kritikos, and A. Caneschi. Self assembly, structure and properties of the decanuclear lanthanide ring complex, $Dy_{10}(OC_2H_4OCH_3)_{30}$. *Chem. Commun.*, 10:1012–1013, 2003.

[24] N. Ishikawa, M. Sugita, and W. Wernsdorfer. Quantum tunneling of magnetization in lanthanide single-molecule magnets, bis(phthalocyaninato)terbium and bis(phthalocyaninato)-dysprosium anions. *Angew. Chem. -Int. Edit.*, 44:2931–2935, 2005.

[25] J. Long, F. Habib, P. Lin, I. Korobkov, G. Enright, L. Ungur, W. Wernsdorfer, L. Chibotaru, and M. Murugesu. Single-molecule magnet behavior for an antiferromagnetically superexchange-coupled dinuclear dysprosium(III) complex. *J. Am. Chem. Soc*, 133:5319–5328, 2011.

[26] K. Pedersen, J. Bendix, and R. Clérac. Single-molecule magnet engineering: building-block approaches. *Chem. Commun.*, 50:4396, 2014.

[27] H. Heersche, Z. De Groot, J. Folk, H. Van Der Zant, C. Romeike, M. Wegewijs, L. Zobbi, D. Barreca, E. Tondello, and A. Cornia. Electron transport through

single Mn12 molecular magnets. *Phys. Rev. Lett.*, 96:206801, 2006.

[28] M. Jo, J. Grose, K. Baheti, M. Deshmukh, J. Sokol, E. Rumberger, D. Hendrickson, J. Long, H. Park, and D. Ralph. Signatures of molecular magnetism in single-molecule transport spectroscopy. *Nano Lett.*, 6:2014–2020, 2006.

[29] G. Kim and T. Kim. Electronic transport in single-molecule magnets on metallic surfaces. *Phys. Rev. Lett.*, 92:137203, 2004.

[30] K. Ullmann, P. Coto, S. Leitherer, A. Molina-Ontoria, N. Martín, M. Thoss, and H. Weber. Single-molecule junctions with epitaxial graphene nanoelectrodes. *Nano Lett.*, 15:3512–3518, 2015.

[31] S. Phark, Z. Khim, B. Kim, B. Suh, S. Yoon, J. Kim, J. Lim, and Y. Do. Atomic force microscopy study of Mn12 single-molecule magnet adsorbed on Au surface. *Jpn. J. Appl. Phys.*, 43:8273–8277, 2004.

[32] R. Moroni, R. Buzio, A. Chincarini, U. Valbusa, F. de Mongeot, L. Bogani, A. Caneschi, R. Sessoli, L. Cavigli, and M. Gurioli. Optically addressable single molecule magnet behaviour of vacuum-sprayed ultrathin films. *J. Mater. Chem.*, 18:109, 2008.

[33] L. Margheriti, D. Chiappe, M. Mannini, P. Car, P. Sainctavit, M. Arrio, F. De Mongeot, J. Cezar, F. Piras, A. Magnani, E. Otero, A. Caneschi, and R. Sessoli. X-ray detected magnetic hysteresis of thermally evaporated terbium double-decker oriented films. *Adv. Mater.*, 22:5488–5493, 2010.

[34] P. Totaro, L. Poggini, A. Favre, M. Mannini, P. Sainctavit, A. Cornia, A. Magnani, and R. Sessoli. Tetrairon(III) single-molecule magnet monolayers on gold: Insights from ToF-SIMS and isotopic labeling. *Langmuir*, 30:8645–8649, 2014.

[35] C. Cervetti, E. Heintze, and L. Bogani. Interweaving spins with their environment: novel inorganic nanohybrids with controllable magnetic properties. *Dalton Trans.*, 43:4220–32, 2014.

[36] L. Zobbi, M. Mannini, M. Pacchioni, G. Chastanet, D. Bonacchi, C. Zanardi, R. Biagi, U. Del Pennino, D. Gatteschi, A. Cornia, and R. Sessoli. Isolated single-molecule magnets on native gold. *Chem. Commun.*, 6:1640–1642, 2005.

[37] E. Coronado, A. Forment-Aliaga, F. Romero, V. Corradini, R. Biagi, V. De Renzi, A. Gambardella, and U. del Pennino. Isolated Mn_{12} single-molecule magnets grafted on gold surfaces via electrostatic interactions. *Inorg. Chem.*, 44:7693–7695, 2005.

[38] D. Ruiz-Molina, M. Mas-Torrent, J. Gómez, A. Balana, N. Domingo, J. Tejada, M. Martínez, C. Rovira, and J. Veciana. Isolated single-molecule magnets on the surface of a polymeric thin film. *Adva. Mater.*, 15:42–45, 2003.

[39] S. Kahle, Z. Deng, N. Malinowski, C. Tonnoir, A. Forment-Aliaga, N. Thontasen, G. Rinke, D. Le, V. Turkowski, T. Rahman, S. Rauschenbach, M. Ternes, and K. Kern. The quantum magnetism of individual manganese-12-acetate molecular magnets anchored at surfaces. *Nano Lett.*, 12:518–521, 2012.

[40] J. Park, A. Pasupathy, J. Goldsmith, C. Chang, Y. Yaish, P. Mceuen, J. Petta, M. Rinkoski, J. Sethna, H. Abruña, and D. Ralph. Coulomb blockade and the

Kondo effect in single-atom transistors. *Nature*, 417:722–5, 2002.

[41] T. Lis. Preparation, structure, and magnetic properties of a dodecanuclear mixed-valence manganese carboxylate. *Acta Cryst. B*, 36:2042–2046, 1980.

[42] B. Kochelaev and Y. Yablokov. *The beginning of paramagnetic resonance*. Word Scientific Publishing Co. Pte. Ltd, 1995.

[43] J. Richardson and W. Milligan. Magnetic properties of nickelous oxide. *Phys. Rev. B*, 102:1289–1294, 1956.

[44] D. Gatteschi, A. Barra, A. Caneschi, A. Cornia, R. Sessoli, and L. Sorace. EPR of molecular nanomagnets. *Coord. Chem. Rev.*, 250:1514–1529, 2006.

[45] R. Robinson, P. Brown, D. Argyriou, D. Hendrickson, and S. Aubin. Internal magnetic structure of Mn_{12} acetate by polarized neutron diffraction. *J. Phys.: Condens. Matter.*, 12:2805–2810, 2000.

[46] R. Sessoli, D. Gatteschi, A. Caneschi, and M. A. Novak. Magnetic bistability in a metal-ion cluster. *Nature*, 365:141–143, 1993.

[47] C. Paulsen, J. Park, B. Barbara, R. Sessoli, and A. Caneschi. Studies of hysteresis in Mn12Ac. *J. Magn. Magn. Mater.*, 140-144:1891–1892, 1995.

[48] J. Friedman, M. Sarachik, and R. Ziolo. Macroscopic measurement of resonant magnetization tunneling in high-spin molecules. *Phys. Rev. Lett.*, 76:3830–3833, 1996.

[49] H. Eppley, S. Aubin, M. Wemple, D. Hendrickson, and G. Christou. Single-molecule magnets: characterization of complexes exhibiting out-of-Phase AC susceptibility signals. *Mol. Cryst. Liq. Cryst. A*, 305:167–179, 1997.

[50] S. Aubin, S. Spagna, H. Eppley, R. Sager, K. Folting, G. Christou, and D. Hendrickson. Single-molecule magnets: magnetization relaxation and quantum tunneling in dodecanuclear manganese complexes. *Mol. Cryst. Liq. Cryst. A*, 305:181–192, 1997.

[51] G. Arom, S. Aubin, M. Bolcar, G. Christou, H. Eppley, K. Folting, D. Hendrickson, J. Huffman, R. Squire, H. Tsai, S. Wang, and M. Wemple. Manganese carboxylate clusters: from structuralaesthetics to single-molecule magnets. *Polyhedron*, 17:3005–3020, 1998.

[52] H. Eppley, H. Nadine, K. Felting, G. Christou, and D. Hendrickson. High-spin molecules: unusual magnetic susceptibility relaxation effects in $[Mn_{12}O_{12}(O_2CEt)_{16}(H_2O)_3]$ ($S = 9$) and the one-electron reduction product $(PPh_4)[Mn_{12}O_{12}(O_2CEt)_{16}(H_2O)_4]$ ($S = 19/2$). *J. Am. Chem. Soc.*, 117:301–317, 1995.

[53] A. Mishra, W. Wernsdorfer, K. Abboud, and G. Christou. Initial observation of magnetization hysteresis and quantum tunneling in mixed manganese-lanthanide single-molecule magnets. *J. Am. Chem. Soc.*, 126:15648–15649, 2004.

[54] F. Mori, T. Nyui, T. Ishida, T. Nogami, K. Choi, and H. Nojiri. Oximate-bridged trinuclear Dy-Cu-Dy complex behaving as a single-molecule magnet and its mechanistic investigation. *J. Am. Chem. Soc.*, 128:1440–1441, 2006.

[55] J. Costes, S. Shova, and W. Wernsdorfer. Tetranuclear $[Cu\text{-}Ln]_2$ single molecule

magnets: synthesis, structural and magnetic studies. *Dalton Trans.*, 14:1843–1849, 2008.

[56] S. Aubin, M. Wemple, D. Adams, H. Tsai, G. Christou, and D. Hendrickson. Distorted $Mn^{(IV)}Mn^{(III)}{}_3$ cubane complexes as single-molecule magnets. *J. Am. Chem. Soc.*, 118:7746–7754, 1996.

[57] C. Sangregorio, T. Ohm, C. Paulsen, R. Sessoli, and D. Gatteschi. Quantum tunneling of the magnetisation in an Iron cluster nanomagnet. *Phys. Rev. Lett.*, 78:4645–4648, 1997.

[58] A. Boudalis, N. Lalioti, G. Spyroulias, C. Raptopoulou, A. Terzis, A. Bousseksou, V. Tangoulis, and J. Tuchagues. Novel rectangular$[Fe_4(\mu_4\text{-OHO})(\mu\text{-OH})_2]^{7+}$ versus "butterfly" $[Fe_4(\mu_3\text{-O})_2]^{8+}$ Core Topology in the $Fe^{III}/RCO_2{}^-$/phen Reaction Systems (R) = Me, Ph; phen = 1,10-Phenanthroline): Preparation and Properties of $[Fe_4(OHO)(OH)_2(O_2CMe)_4(phen)_4](ClO_4)_3$, $[Fe_4O_2(O_2CPh)_7(phen)_2](ClO_4)$, and $[Fe_4O_2(O_2CPh)_8(phen)_2]$. *Inorg. Chem.*, 41:6474–6487, 2002.

[59] A. Tasiopoulos, A. Vinslava, W. Wernsdorfer, K. Abboud, and G. Christou. Giant single-molecule magnets: a $\{Mn_{84}\}$ torus and its supramolecular nanotubes. *Angew. Chem. -Int. Edit.*, 43:2117–2121, 2004.

[60] A. Ako, I. Hewitt, V. Mereacre, R. Clérac, W. Wernsdorfer, C. Anson, and A. Powell. A ferromagnetically coupled Mn_{19} aggregate with a record $S = 83/2$ ground spin state. *Angew. Chem. -Int. Edit.*, 45:5048–5051, 2006.

[61] M Murugesu, S Takahashi, A Wilson, K. Abboud, W. Wersndorfer, S Hill, and G. Christou. Large Mn_{25} single-molecule magnet with spin $S = 51/2$: magnetic and high-frequency electron paramagnetic resonance spectroscopic characterization of a giant spin state. *Inorg. Chem.*, 47:9459–9470, 2008.

[62] N. Ishikawa, M. Sugita, T. Ishikawa, S. Koshihara, and Y. Kaizu. Lanthanide double-decker complexes functioning as magnets at the single-molecular level. *J. Am. Chem. Soc.*, 125:8694–8695, 2003.

[63] J. Tang, I. Hewitt, N. Madhu, G. Chastanet, W. Wernsdorfer, C. Anson, C. Benelli, R. Sessoli, and A. Powell. Dysprosium triangles showing single-molecule magnet behavior of thermally excited spin states. *Angew. Chem. -Int. Edit.*, 45:1729–1733, 2006.

[64] R. Blagg, C. Muryn, E. McInnes, F. Tuna, and R. Winpenny. Single pyramid magnets: Dy_5 pyramids with slow magnetic relaxation to 40 K. *Angew. Chem. -Int. Edit.*, 50:6530–6533, 2011.

[65] J. Rinehart, M. Fang, W. Evans, and J. Long. Strong exchange and magnetic blocking in N-radical-bridged lanthanide complexes. *Nature Chem.*, 3:538–542, 2011.

[66] P. Zhang, Y. Guo, and J. Tang. Recent advances in dysprosium-based single molecule magnets: Structural overview and synthetic strategies. *Coord. Chem. Rev.*, 257:1728–1763, 2013.

[67] D Sander. The magnetic anisotropy and spin reorientation of nanostructures and nanoscale films. *J. Phys.: Condens. Matter*, 16:R603–R636, 2004.

[68] R. Sessoli, M. Mannini, F. Pineider, A. Cornia, and Ph. Sainctavit. XAS and XMCD of Single Molecule. In *MagnetsMagnetism and Synchrotron Radiation*, pages 279–311. Springer, 2010.

[69] Roman Boca. *Theoretical Foundations of Molecular Magnetism*. Elsevier Science S.A., 1999.

[70] M. Hennion, L. Pardi, I. Mirebeau, E. Suard, R. Sessoli, and A. Caneschi. Neutron study of mesoscopic magnetic clusters: $Mn_{12}O_{12}$. *Phys. Rev. B*, 56:8819–8827, 1997.

[71] R. Caciuffo, G. Amoretti, A. Murani, R. Sessoli, A. Caneschi, and D. Gatteschi. Neutron spectroscopy for the magnetic anisotropy of molecular clusters. *Phys. Rev. Lett.*, 81:4744–4747, 1998.

[72] I. Mirebeau, M. Hennion, H. Casalta, H. Andres, H. Gudel, A. Irodova, and A. Caneschi. Reply to the comment on Low energy magnetic excitations of the Mn12-acetate spin cluster observed by neutron scattering. *Phys. Rev. Lett.*, 83:628–631, 2000.

[73] H. Andres, R. Basler, H. U. Güdel, G. Aromí, G. Christou, H. Büttner, and B. Rufflé. Inelastic neutron scattering and magnetic susceptibilities of the single-molecule magnets $[Mn_4O_3X(OAc)_3(dbm)_3]$ (X = Br, Cl, OAc, and F): variation of the anisotropy along the series. *J. Am. Chem. Soc.*, 122:12469–12477, 2000.

[74] F. El Hallak, J. Van Slageren, and M. Dressel. Torque detected broad band electron spin resonance. *Rev. Sci. Instrum.*, 81:095105, 2010.

[75] D. Gatteschi, R. Sessoli, and J. Villain. *Molecular Nanomagnets*. Oxford University Press, Oxford, 2006.

[76] J. Villain, F. Hartman-Boutron, R. Sessoli, and A. Rettori. Magnetic relaxation in big magnetic molecules. *Europhys. Lett.*, 27:159–164, 2007.

[77] A. Barra, D. Gatteschi, and R. Sessoli. High frequency EPR spectra of a molecular nanomagnet: understanding quantum tunneling of the magnetisation. *Phys. Rev. B*, 56:8192–8198, 1997.

[78] C. Huang. *Rare earth coordination chemistry*. Peking University, China, 2010.

[79] J. Tang and P. Zhang. *Lanthanide single molecule magnets*. Springer, 2015.

[80] J. Rinehart and J. Long. Exploiting single-ion anisotropy in the design of f-element single-molecule magnets. *Chem. Sci.*, 2:2078, 2011.

[81] B. Josephson. Possible new effects in superconductive tunnelling. *Phy. Lett.*, 1:251–253, 1962.

[82] D. Koelle, R. Kleiner, F. Ludwig, E. Dantsker, and J. Clarke. High-transition-temperature superconducting quantum interference devices. *Rev. Mod. Phys.*, 71:631–686, 1999.

[83] I. Simacek, V. Zrubec, and M. Skakala. rf SQUID magnetometer with simplified circuitry. *Rev. Sci. Instrum.*, 64:2401–2402, 1993.

[84] R. Jaklevic, J. Lambe, A. Silver, and J. Mercereau. Quantum interference effects in Josephson tunneling. *Phys. Rev. Lett.*, 12:159–160, 1964.

[85] Quantum Design. *Magnetic Property Measurement System MPMS MultiVu Application Users Manual Technical support*. Quantum Design, 2004.

[86] H Lueken. Superconducting Quantum Interference Device Magnetometry. In R. Schäfer and P. C. Schmidt, editor, *Methods in Physical Chemistry*. Wiley-VCH Verlag GmbH & Co. KGaA, 2012.

[87] N. Domingo, F. Luis, M. Nakano, M. Muntó, J. Gómez, J. Chaboy, N. Ventosa, J. Campo, J. Veciana, and D. Ruiz-Molina. Particle-size dependence of magnetization relaxation in Mn_{12} crystals. *Phys. Rev. B*, 79:214404, 2009.

[88] M. Karas, D. Bachmann, and F. Hillenkamp. Influence of the wavelength in high-irradiance ultraviolet laser desorption mass spectrometry of organic molecules. *Anal. Chem.*, 57:2935–2939, 1985.

[89] C. Benelli and D. Gatteschi. Molecular Spintronics. In *Introduction to Molecular Magnetism*. Wiley-VCH Verlag GmbH & Co. KGaA, 2015.

[90] A. Cornia, A. Fabretti, M. Pacchioni, L. Zobbi, D. Bonacchi, A. Caneschi, D. Gatteschi, R. Biagi, U. Del Pennino, V. De Renzi, L. Gurevich, and H. Van der Zant. Direct observation of single-molecule magnets organized on gold surfaces. *Angew. Chem. -Int. Edit.*, 42:1645–1648, 2003.

[91] M. Burgert, S. Voss, S. Herr, M. Fonin, U. Groth, and U. Ruediger. Single-molecule magnets: a new approach to investigate the electronic structure of Mn_{12} molecules by scanning tunneling spectroscopy. *J. Am. Chem. Soc.*, 129:14362–14366, 2007.

[92] M. Mannini. *Molecular magnetic materials on solid surfaces*. Firenze University Press, 2008.

[93] S. Kyatskaya, F. Hennrich, M. Kappes, W. Wernsdorfer, and M. Ruben. Anchoring of rare-earth-based single-molecule magnets on single-walled carbon nanotubes. *J. Am. Chem. Soc.*, 131:15143–15151, 2009.

[94] L. Rigamonti, M. Piccioli, L. Malavolti, L. Poggini, M. Mannini, F. Totti, B. Cortigiani, A. Magnani, R. Sessoli, and A. Cornia. Enhanced vapor-phase processing in fluorinated Fe_4 single-molecule magnets. *Inorg. Chem.*, 52:5897–5905, 2013.

[95] D. Tanaka, T. Inose, S. Shimono, H. Tanaka, T. Tamaki, A. Abd El-Mageed, A. Dyab, N. Ishikawa, and T. Ogawa. Surface self-assembly of trans-substituted porphyrin double-decker complexes exhibiting slow magnetic relaxation. *e-J. Surf. Sci. Nanotech.*, 12:124–128, 2014.

[96] N. Turner and J. Schreifels. Surface analysis: X-ray photoelectron spectroscopy and auger electron spectroscopy. *Anal. Chem.*, 66:163R–185R, 1994.

[97] M. Mohai. *Development and Applications of Quantitative X-ray Photoelectron Spectroscopy*. PhD thesis, Hungarian Academy of Sciences, 2005.

[98] G. Binnig and C. Quate. Atomic force microscope. *Phys. Rev. Lett.*, 56:930–933, 1986.

[99] N. Jalili and K. Laxminarayana. A review of atomic force microscopy imaging systems: Application to molecular metrology and biological sciences. *Mechatronics*, 14:907–945, 2004.

[100] https://undergrad.research.ucsb.edu/wp-content/uploads/AFM_laser.gif .

[101] A. Candini, S. Klyatskaya, M. Ruben, W. Wernsdorfer, and M. Affronte. Graphene spintronic devices with molecular nanomagnets. *Nano Lett.*, 11:2634–2639, 2011.

[102] M. Mannini, F. Pineider, C. Danieli, F. Totti, L. Sorace, P. Sainctavit, M. Arrio, E. Otero, L. Joly, J. Cezar, A. Cornia, and R. Sessoli. Quantum tunnelling of the magnetization in a monolayer of oriented single-molecule magnets. *Nature*, 468:417–421, 2010.

[103] C. Bosch-Navarro, E. Coronado, C. Martí-Gastaldo, B. Rodríguez-González, and L. Liz-Marzán. Electrostatic anchoring of Mn4 single-molecule magnets onto chemically modified multiwalled carbon nanotubes. *Adv. Func. Mater.*, 22:979–988, 2012.

[104] A. Ghirri, V. Corradini, V. Bellini, R. Biagi, U. Pennino, V. Renzi, J. Cezar, C. Muryn, G. Timco, R. Winpenny, and M. Affronte. Self-assembled monolayer of Cr7Ni molecular nanomagnets by sublimation. *ACSNANO*, 5:7090–7099, 2011.

[105] L. Malavolti, V. Lanzilotto, S. Ninova, L. Poggini, I. Cimatti, B. Cortigiani, L. Margheriti, D. Chiappe, E. Otero, P. Sainctavit, F. Totti, A. Cornia, M. Mannini, and R. Sessoli. Magnetic bistability in a submonolayer of sublimated Fe4 single-molecule magnets. *Nano Lett.*, 15:535–541, 2015.

[106] L. Bogani, C. Danieli, E. Biavardi, N. Bendiab, A. Barra, E. Dalcanale, W. Wernsdorfer, and A. Cornia. Single-molecule-magnet carbon-nanotube hybrids. *Angew. Chem. -Int. Edit.*, 48:746–750, 2009.

[107] S. Jiang, K. Goß, C. Cervetti, and L. Bogani. An introduction to molecular spintronics. *Sci. China Chem.*, 55:867–882, 2012.

[108] M. Nakano and H. Oshio. Magnetic anisotropies in paramagnetic polynuclear metal complexes. *Chemi. Soc. Rev.*, 40:3239–3248, 2011.

[109] S. Langley, N. Chilton, B. Moubaraki, and K. S. Murray. Anisotropy barrier enhancement via ligand substitution in tetranuclear $\{Co^{(III)}{}_2Ln^{(III)}{}_2\}$ single molecule magnets. *Chem. Commun.*, 49:6965–7, 2013.

[110] S. Blundell and F. Pratt. Organic and molecular magnets. *J. Phys.: Condens. Matter.*, 16:R771–R828, 2004.

[111] R. Winpenny. Serendipitous assembly of polynuclear cage compounds. *J. Chem. Soc., Dalton Trans.*, 6:1–10, 2002.

[112] R. Sessoli and A. Powell. Strategies towards single molecule magnets based on lanthanide ions. *Coord. Chem. Rev.*, 253:2328–2341, 2009.

[113] M. Ding, B. Wang, Z. Wang, J. Zhang, O. Fuhr, D. Fenske, and S. Gao. Constructing single-chain magnets by supramolecular π-π stacking and spin canting: a case study on manganese(III) corroles. *Chem. Eur. J.*, 18:915–924, 2012.

[114] F. Richardson, W. Wagner, and D. Sands. Rare earth trishexafluoroacetylacetonates and related compounds. *J. Inorg. Nucl. Chem.*, 30:1275–1289, 1968.

[115] K. Bernot, L. Bogani, R. Sessoli, and D. Gatteschi. $[Tm^{III}(hfac)_3(NITPhOPh)]$: A new member of a lanthanide-based single chain magnets family. *Inorg. Chim. Acta*, 360:3807–3812, 2007.

[116] G. Zucchi, T. Jeon, D. Tondelier, D. Aldakov, P. Thuéry, M. Ephritikhine, and B. Geffroy. White electroluminescence of lanthanide complexes resulting from exciplex formation. *J. Mater. Chem.*, 20:2114–2120, 2010.

[117] P. Guo, J. Liu, Z. Zhang, L. Ungur, L. Chibotaru, J. Leng, F. Guo, and M. Tong. The first $\{Dy_4\}$ single-molecule magnet with a toroidal magnetic moment in the ground state. *Inorg. Chem.*, 51:1233–5, 2012.

[118] G. M. Sheldrick. *Program for the Solution of Crystal Structures*. University of Gottingen, Gottingen, Germany, 1997.

[119] Y. Wang, X. Yang, J. Tang, P. Cheng, Q. Wang, L. Li, and D. Liao. Syntheses, structures, and magnetic and luminescence properties of a new Dy^{III}-based single-ion magnet. *Inorg. Chem.*, 52:7380–7386, 2013.

[120] L. Bogani, C. Sangregorio, R. Sessoli, and D. Gatteschi. Molecular engineering for single-chain-magnet behavior in a one-dimensional dysprosium-nitronyl nitroxide compound. *Angew. Chem. -Int. Edit.*, 44:5817–5821, 2005.

[121] G. Cosquer, F. Pointillart, S. Golhen, O. Cador, and L. Ouahab. Slow magnetic relaxation in condensed versus dispersed dysprosium(III) mononuclear complexes. *Chem. Eur. J.*, 19:7895–7903, 2013.

[122] Y. Ma, G. Xu, X. Yang, L. Li, J. Tang, S. Yan, P. Cheng, and D. Liao. Pyrazine-bridged Dy2 single-molecule magnet with a large anisotropic barrier. *Chem. Commun.*, 46:8264–8266, 2010.

[123] M. Kahn, J. Sutter, P. Guionneau, L. Ouahab, O. Kahn, and D. Chasseau. Systematic investigation of the nature of the coupling between a Ln(III) Ion (Ln = Ce(III) to Dy(III)) and its aminoxyl radical ligands. *J. Am. Chem. Soc.*, 122:3413–3421, 2000.

[124] M. Kahn, R. Ballou, P. Porcher, O. Kahn, and J. Sutter. Analytical determination of the {Ln - aminoxyl radical} exchange interaction taking into account both the ligand-field effect and the spin - orbit coupling of the lanthanide ion (Ln = Dy(III) and Ho(III). *Chem. Eur. J.*, 8:525–531, 2002.

[125] M. Ren, S. Bao, N. Hoshino, T. Akutagawa, B. Wang, Y. Ding, S. Wei, and L. Zheng. Solvent responsive magnetic dynamics of a dinuclear dysprosium single-molecule magnet. *Chem. Eur. J.*, 19:9619–9628, 2013.

[126] L. Batchelor, I. Cimatti, R. Guillot, F. Tuna, W. Wernsdorfer, L. Ungur, L. Chibotaru, V. Campbell, and T. Mallah. Chemical tuning of the magnetic relaxation in dysprosium(III) mononuclear complexes. *Dalton Trans.*, 43:12146–12149, 2014.

[127] G. Poneti, K. Bernot, L. Bogani, A. Caneschi, R. Sessoli, W. Wernsdorfer, and D. Gatteschi. A rational approach to the modulation of the dynamics of the magnetisation in a dysprosium-nitronyl-nitroxide radical complex. *Chem. Commun.*, pages 1807–1809, 2007.

[128] P. Car, M. Perfetti, M. Mannini, A. Favre, A. Caneschi, and R. Sessoli. Giant field dependence of the low temperature relaxation of the magnetization in a dysprosium(III)-DOTA complex. *Chem. Commun.*, 47:3751–3753, 2011.

[129] A. Watanabe, A. Yamashita, M. Nakano, T. Yamamura, and T. Kajiwara. Multi-path magnetic relaxation of mono-dysprosium(III) single-molecule magnet with extremely high barrier. *Chem. Eur. J.*, 17:7428–7432, 2011.

[130] Y. Gao, G. Xu, L. Zhao, J. Tang, and Z. Liu. Observation of slow magnetic relaxation in discrete dysprosium cubane. *Inorg. Chem.*, 48:11495–11497, 2009.

[131] D. Zeng, M. Ren, S. Bao, and L. Zheng. Tuning the coordination geometries and magnetic dynamics of $[Ln(hfac)_4]^-$ through alkali metal counterions. *Inorg. Chem.*, 53:795–801, 2014.

[132] E. Fatila, E. Hetherington, M. Jennings, A. Lough, and K. Preuss. Syntheses and crystal structures of anhydrous $Ln(hfac)_3$(monoglyme). Ln = La, Ce, Pr, Sm, Eu, Gd, Tb, Dy, Er, Tm. *Dalton Trans.*, 41:1352, 2012.

[133] M. Congiu, M. Alamiry, O. Moudam, S. Ciorba, P. Richardson, L. Maron, A. Jones, B. Richards, and N. Robertson. Preparation and photophysical studies of $[Ln(hfac)_3$DPEPO], Ln = Eu, Tb, Yb, Nd, Gd; interpretation of total photoluminescence quantum yields. *Dalton Trans.*, 42:13537–13545, 2013.

[134] L. Liang, G. Peng, G. Li, Y. Lan, A. Powell, and H. Deng. In situ hydrothermal synthesis of dysprosium(III) single-molecule magnet with lanthanide salt as catalyst. *Dalton Trans.*, 41:5816, 2012.

[135] Y. Wang, X. L, T. Wang, Y. Song, and X. You. Slow relaxation processes and single-ion magnetic behaviors in dysprosium-containing complexes. *Inorg. Chem.*, 49:969–976, 2010.

[136] José J. Baldoví, Juan J. Borrás-Almenar, Juan M. Clemente-Juan, Eugenio Coronado, and Alejandro Gaita-Ariño. Modeling the properties of lanthanoid single-ion magnets using an effective point-charge approach. *Dalton Trans.*, 41:13705–13710, 2012.

[137] L. Chibotaru and L. Ungur. Ab initio calculation of anisotropic magnetic properties of complexes. I. Unique definition of pseudospin Hamiltonians and their derivation. *J. Chem. Phys.*, 137:064112, 2012.

[138] K. Qian, J. Baldoví, S. Jiang, A. Gaita-Ariño, Y. Zhang, J. Overgaard, B. Wang, E. Coronado, and S. Gao. Does the thermal evolution of molecular structures critically affect the magnetic anisotropy? *Chem. Sci.*, 6:4587–4593, 2015.

[139] I. Oyarzabal, J. Ruiz, José M. Seco, M. Evangelisti, A. Camón, E. Ruiz, D. Aravena, and E. Colacio. Rational electrostatic design of easy-axis magnetic anisotropy in a Zn(II)-Dy(III)-Zn(II) single-molecule magnet with a high energy barrier. *Chem. Eur. J.*, 20:1–9, 2014.

[140] S. Jiang and S. Qin. Prediction of the quantized axis of rare-earth ions: the electrostatic model with displaced point charges. *Inorg. Chem. Front.*, 2:613–619, 2015.

[141] X. Huang, V. Vieru, L. Chibotaru, W. Wernsdorfer, S. Jiang, and X. Wang. Determination of magnetic anisotropy in a multinuclear Tb^{III}-based single-molecule magnet. *Chem. Commun.*, 51:10373–10376, 2015.

[142] N. Chilton, D. Collison, E. McInnes, R. Winpenny, and A. Soncini. An electrostatic

model for the determination of magnetic anisotropy in dysprosium complexes. *Nature Commun.*, 4:1–7, 2013.

[143] Q. Chen, Y. Meng, Y. Zhang, S. Jiang, H. Sun, and S. Gao. A 1D dysprosium chain with slow magnetic relaxation constructed from a pyridine-N-oxide ligand. *Chem. Commun.*, 50:10434–7, 2014.

[144] J. Baldoví, S. Cardona-Serra, J. Clemente-Juan, E. Coronado, A. Gaita-Ariño, and A. Palii. SIMPRE: A software package to calculate crystal field parameters, energy levels, and magnetic properties on mononuclear lanthanoid complexes based on charge distributions. *J. Computa. Chem.*, 34:1961–1967, 2013.

[145] J. Baldoví, J. Clemente-Juan, E. Coronado, A. Gaita-Ariño, and A. Palii. An updated version of the computational package SIMPRE that uses the standard conventions for Stevens crystal field parameters. *J. Comput. Chem.*, 35:1930–4, 2014.

[146] F. Luis, M. Martínez-Pérez, O. Montero, E. Coronado, S. Cardona-Serra, C. Martí-Gastaldo, J. Clemente-Juan, J. Sesé, D. Drung, and T. Schurig. Spin-lattice relaxation via quantum tunneling in an Er^{3+} -polyoxometalate molecular magnet. *Phys. Rev. B*, 82:060403, 2010.

[147] R. Layfield, J. McDouall, S. Sulway, F. Tuna, D. Collison, and R. Winpenny. Influence of the N-bridging ligand on magnetic relaxation in an organometallic dysprosium single-molecule magnet. *Chem. Eur. J.*, 16:4442–4446, 2010.

[148] K. Bernot, F. Pointillart, P. Rosa, M. Etienne, R. Sessoli, and D. Gatteschi. Single molecule magnet behaviour in robust dysprosium-biradical complexes. *Chem. Commun.*, 46:6458–6460, 2010.

[149] F. Habib, G. Brunet, V. Vieru, I. Korobkov, L. Chibotaru, and M. Murugesu. Significant enhancement of energy barriers in dinuclear dysprosium single-molecule magnets through electron-withdrawing effects. *J. Am. Chem. Soc.*, 135:13242–13245, 2013.

[150] J. A. Mydosh. *Spin glasses: an experimental introduction.* Taylor & Francis, 1993.

[151] L. Vitali, S. Fabris, A. Conte, S. Brink, M. Ruben, S. Baroni, and K. Kern. Electronic structure of surface-supported bis(phthalocyaninato) terbium(III) single molecular magnets. *Nano Lett.*, 8:3364–3368, 2008.

[152] L. Margheriti, M. Mannini, L. Sorace, L. Gorini, D. Gatteschi, A. Caneschi, D. Chiappe, R. Moroni, F. De Mongeot, A. Cornia, F. Piras, A. Magnani, and R. Sessoli. Thermal deposition of intact tetrairon(III) single-molecule magnets in high-vacuum conditions. *Small*, 5:1460–1466, 2009.

[153] D. Shirley. High-resolution x-ray photoemission spectrum of the valence bands of gold. *Phys. Rev. B*, 5:4709–4714, 1972.

[154] D. Sarma and C. Rao. XPES studies of oxides of second- and third-row transition metals including rare earths. *J. Electron. Spectrosc. Relat. Phenom.*, 20:25–45, 1980.

[155] B. Padalia, W. Lang, P. Norris, L. Watson, and D. Fabian. X-Ray photoelectron core-level studies of the heavy rare-earth metals and their oxides. *Proc. R. Soc. A.*,

354:269–290, 1977.

[156] A. Bismarck, R. Tahhan, J. Springer, A. Schulz, T. Klapötke, H. Zeil, and W. Michaeli. Influence of fluorination on the properties of carbon fibres. *J. Fluor. Chem.*, 84:127–134, 1997.

[157] P. Sundberg, R. Larsson, and B. Folkesson. On the core electron binding energy of carbon and the effective charge of the carbon atom. *J. Electron. Spectrosc. Relat. Phenom.*, 46:19–29, 1988.

[158] L. Sorace, C. Benelli, and D. Gatteschi. Lanthanides in molecular magnetism: old tools in a new field. *Chemi. Soc. Rev.*, 40:3092–3104, 2011.

[159] M. De Volder, S. Tawfick, R. Baughman, and A. Hart. Carbon nanotubes: present and future commercial applications. *Science*, 339:535–9, 2013.

[160] A. Geim and K. Novoselov. The rise of graphene. *Nat. Mater.*, 6:183–191, 2007.

[161] L. Bogani and W. Wernsdorfer. A perspective on combining molecular nanomagnets and carbon nanotube electronics. *Inorg. Chim. Acta*, 361:3807–3819, 2008.

[162] G. Whitesides, J. Kriebel, and B. Mayers. Self-assembly and nanostructured materials. In *Nanoscale Assembly*, pages 217–239. Springer, 2005.

[163] N. Shang, P. Papakonstantinou, M. McMullan, M. Chu, A. Stamboulis, A. Potenza, S. Dhesi, and H. Marchetto. Catalyst-free efficient growth, orientation and biosensing properties of multilayer graphene nanoflake films with sharp edge planes. *Adv. Func. Mate.*, 18:3506–3514, 2008.

[164] N. Tombros, C. Jozsa, M. Popinciuc, H. Jonkman, and B. van Wees. Electronic spin transport and spin precession in single graphene layers at room temperature. *Nature*, 448:571–574, 2007.

[165] W. Han, K. Pi, K. McCreary, Y. Li, J. Wong, A. Swartz, and R. Kawakami. Tunneling spin injection into single layer graphene. *Phys. Rev. Lett.*, 105:167202, 2010.

[166] T. Yang, J. Balakrishnan, F. Volmer, A. Avsar, M. Jaiswal, J. Samm, S. R. Ali, A. Pachoud, M. Zeng, M. Popinciuc, G. Güntherodt, B. Beschoten, and B. Özyilmaz. Observation of long spin-relaxation times in bilayer graphene at room temperature. *Phys. Rev. Lett.*, 107:047206, 2011.

[167] W. Han, R. Kawakami, M. Gmitra, and J. Fabian. Graphene spintronics. *Nat. Nanotech.*, 9:794–807, 2014.

[168] K. Novoselov, A. Geim, S. Morozov, D. Jiang, Y. Zhang, S. Dubonos, I. Grigorieva, and A. Firsov. Electric field effect in atomically thin carbon films. *Science*, 306:666–669, 2004.

[169] C. Berger, Z. Song, T. Li, X. Li, A. Ogbazghi, R. Feng, Z. Dai, A. Marchenkov, E. Conrad, P. First, and W. de Heer. Ultrathin epitaxial graphite: 2D electron gas properties and a route toward graphene-based nanoelectronics. *J. Phys. Chem. B*, 108:19912–19916, 2004.

[170] C. Berger, X. Wu, N. Brown, C. Naud, X. Li, Z. Song, D. Mayou, T. Li, J. Hass, A. Marchenkov, E. Conrad, P. First, and W. De Heer. Electronic Confinement and Coherence in patterned epitaxial graphene. *Science*, 312:1191–1196, 2006.

[171] S. Stankovich, D. Dikin, G. Dommett, K. Kohlhaas, E. Zimney, E. Stach, R. Piner, S. Nguyen, and R. Ruoff. Graphene-based composite materials. *Nature*, 442:282–286, 2006.

[172] Q. Yu, J. Lian, S. Siriponglert, H. Li, Y. Chen, and S. Pei. Graphene segregated on Ni surfaces and transferred to insulators. *Appli. Phys. Lett.*, 93:113103, 2008.

[173] A. Reina, X. Jia, J. Ho, D. Nezich, H. Son, V. Bulovic, M. Dresselhaus, K. Jing, and J. Kong. Large area, few-layer graphene films on arbitrary substrates by chemical vapor deposition. *Nano Lett.*, 9:30–35, 2009.

[174] X. Li, W. Cai, J. An, S. Kim, J. Nah, D. Yang, R. Piner, A. Velamakanni, I. Jung, E. Tutuc, S. K. Banerjee, L. Colombo, and R. S. Ruoff. Large-area synthesis of high-quality and uniform graphene films on copper foils. *Science*, 324:1312–1314, 2009.

[175] K. Novoselov and A. Castro Neto. Two-dimensional crystals-based heterostructures: materials with tailored properties. *Phys. Scr.*, T146:014006, 2012.

[176] P. Blake, E. Hill, A. Castro Neto, K. Novoselov, D. Jiang, R. Yang, T. J. Booth, and A. K. Geim. Making graphene visible. *Appli. Phys. Lett.*, 91:063124, 2007.

[177] A. Ferrari, J. Meyer, C. Scardaci, C. Casiraghi, and M. Lazzeri. Raman spectrum of graphene and graphene layers. *Phys. Rev. Lett.*, 97:187401 (4), 2006.

[178] I. Lewis and H. Edwards. *Handbook of Raman spectroscopy.* Marcel Dekker, INC., 2001.

[179] D. Graf, F. Molitor, K. Ensslin, C. Stampfer, A. Jungen, C. Hierold, and L. Wirtz. Spatially resolved raman spectroscopy of single- and few-layer graphene. *Nano Lett.*, 7:238–242, 2007.

[180] H. Dai. Carbon nanotubes: synthesis, integration, and properties. *Acc. Chem. Res.*, 35:1035–1044, 2002.

[181] J. Seo, N. Yoder, T. Shastry, J. Humes, J. Johns, A. Green, and M. Hersam. Diameter refinement of semiconducting arc discharge single-walled carbon nanotubes via density gradient ultracentrifugation. *J. Phys. Chem. Lett.*, 4:2805–2810, 2013.

[182] M. Bystrzejewski, M. Ruemmeli, H. Lange, A. Huczko, P. Baranowski, T. Gemming, and T. Pichler. Single-walled carbon nanotubes synthesis: A direct comparison of laser ablation and carbon arc routes. *J. Nanosci. Nanotech.*, 8:6178–86, 2008.

[183] P. Poulsen, J. Borggreen, J. Nygård, D. Cobden, M. Andreasen, and P. Lindelof. Single-wall carbon nanotube devices prepared by chemical vapor deposition. In *AIP Conf. Proc.*, volume 544, pages 504–507. AIP, 2000.

[184] M. Rahman, H. Younes, N. Subramanian, and A. Ghaferi. Optimizing the dispersion conditions of SWCNTs in aqueous solution of surfactants and organic solvents. *J. Nanomater.*, 2014, 2014.

[185] S. Reich and C. Thomsen. Raman spectroscopy of graphite. *Phil. Trans. R. Soc. Lond. A*, 362:2271–2288, 2004.

[186] C. Lau, J. Mol, J. Warner, and G. Briggs. Nanoscale control of graphene electrodes. *Phys. Chem. Chem. Phys.*, 16:20398–20401, 2014.

List of Abbreviations

AC	alternating current
AFM	atomic force microscope or microscopy
bpy	2,2′-bipyridine
CVD	chemical vapour deposition
DC	direct current
E_B	binding energy
EDX	energy dispersive X-ray
E_K	kinetic energy
EPR	electron paramagnetic resonance
EtOAc	ethyl acetate
GO	graphite oxide
MALDI-TOF MS	Matrix-Assisted Laser Desorption/Ionization-Time of Flight Mass Spectrometry
mK	milliKelvin
$Mn_{12}OAc$	a typical single-molecule magnet compound with the chemical structure: $Mn_{12}O_{12}(CH_3COO)_{16}(H_2O)_4]\cdot 2CH_3COOH\cdot 4H_2O$
MP	methyl propionate
^{1}H-NMR	proton nuclear magnetic resonance
HAT	1,4,5,8,9,12-hexaazatriphenylene
hfac	hexafluoroacetylacetonate
HOPG	highly oriented pyrolytic graphite
INS	Inelastic Neutron Scattering
Ln	lanthanide
NDR	negative differential resistance
QD	quantum dot
QTM	quantum tunnelling of the magnetisation
RF-SQUID	radio frequency superconducting quantum interference device
RSO	reciprocating sample option
SEM	scanning electron microscope (or microscopy)
SH	Spin Hamiltonian
SMM	single-molecule magnet
SQUID	superconducting quantum interference device
STM	scanning tunnelling microscope (or microscopy)
RBM	Radial Breathing Mode
tBu-bpy	4,4′-di-tert-butyl-2,2′-bipyridine

TCNQ	7,7′,8,8′-tetracyanoquinodimethane
TEM	transmission electron microscope (or microscopy)
XPS	X-ray photoelectron spectroscopy
UHV	ultra-high vacuum
ZFS	zero-field splitting

Acknowledgements

Throughout my PhD study at University of Stuttgart in Germany, I met many wonderful peoples and have truly enjoyed studying and working here. It is the right time for me to express my greatest gratitude to all the people who helped me bring this thesis to the light.

I thank Chinese CSC (China Scholarship Council fellowship Grant) for financial support to my PhD study and work in this great university in Germany.

I was lucky to work with and learn from Dr. Lapo Bogani who is my thesis advisor. His constant pursuit of new ideas and profound knowledge imprinted in my mind a great scientist. Close to this study end, I felt embarrassed to realise how many mistakes I made in the passed three years. Thank Lapo for his trust and guidance on my study and work.

I thank Prof. Dr. Martin Dressel, the director of our institute and my first thesis supervisor. Every discussion about my thesis project imprinted his prudent scientific attitude and uncompromising attention to important details in my mind.

I also thank Prof. Dr. Joris van Slageren, my second thesis supervisor for his kindness and patience in giving his suggestions and comments on this thesis.

I also thank Prof. Dr. Wolfgang Kaim for being chairman in my defence and for giving comments on this thesis.

Here I sincerely thank the people who helped to measure our samples by using different techniques. They are Dr. Wolfgang Frey from Organic Chemistry Institute of the University of Stuttgart, Ms Barbara Förtsch Inorganic Chemistry department of the University of Stuttgart, Dr. Wolfgang Kröner and Prof. Dr. Paul Müller from Department of Physics at Universät Erlangen-Nürnberg, Dr. Mark H. Rmmeli at Leibniz-Institut für Festkörper- und Werkstoffforschung (IFW) Dresden and Dresden University of Technology, Germany, Dr. Shang -Da Jiang from the School of Chemistry at the Peking University, P.R. China, Dr. Mitssuharu Konuma at Max Planck Institute at Stuttgart, Dipl. Chem. Alexander Hoyer at Max Planck Institute at Stuttgart, M. Sc. Kristina Vaklinova at Max Planck Institute at Stuttgart, M. Sc. Nilesh Vats at Max Planck Institute at Stuttgart, M. Sc. Chit Siong Aaron Lau, Dr. Junjie Liu and Dr. Jan Mol from Oxford University, England.

I felt very lucky to be able to study and work in the Nanomagnetism group in 1st Physics Institute during my graduate career. Many thanks to all my dear group members for their help and company: Dr. Shang -Da Jiang, Dr. Karin Goß, Dr. Ralph Hübner, Christian Cervetti, Eric Heintze, Alexa Paretzki, Michael Slota, Nicola Dotti, Marian Blankenhorn.

Particularly, I want to acknowledge Dr. Shang -Da Jiang and Dr. Ralph Hübner, two great Chemists, who taught me the Chemistry beauty! Without their help and

suggestions, this thesis project must be boring.

And I thank Christian Cervetti as well who gave me lots of good lessons from the beginning until now. I still remember the crazy days spent with him in the labs and I will cherish these wonderful memories.

I was lucky to have the opportunity to work at Max Planck Institute (MPI) at Stuttgart. Several people at MPI deserve special thanks.

Special thanks to Dr. Stephan Rauschenbach and his PhD student Sabine Abb, who offered me great support for carrying on my thesis at MPI at Stuttgart.

Also many thanks to Alexander Hoyer, who, with his cheerful manners and help, kept my working days at MPI pleasant and fun.

I thank Kristina Vaklinova and Nilesh Vats as well for their kindness and help.

I also want to acknowledge my Chinese friends at Stuttgart: Shuai Xue, Huiqiang Wang, Kaipei Tian, Ran Su, Min Wang, Yuan Yan, Peng Zhang, Shuai Jiang, Meng Wang, Weiwu Li, Qi Ai, and Ning Zhou. I had lots of fun with them, and getting together keeps me entertained and happy throughout my days at Stuttgart.

My warmest thanks to my old friend Lei Lei. Without her support for me applying this PhD position, this thesis cannot exist. Through her creative energy and witty insights, she has made my life full of excitement and joy.

Finally, special thanks, of course, to my family. My dear Dad and Mom, with their unceasing love, gave me the strength to finish this work. I also thank my cheerful young brother Lianfeng Wang and young sister Yali Wang, who gave me lots of support and warm caring.